MSc Thesis

Comparative modelling of membrane and packed-bed methanol reformers integrated with low temperature PEMFC for on-board ship applications

Filippo Bernardinelli

TU Delft

Comparative modelling of membrane and packed-bed methanol reformers integrated with low temperature PEMFC for on-board ship applications

by

Filippo Bernardinelli

to obtain the degree of Master of Science
at the Delft University of Technology,
to be defended publicly on Monday November 3rd, 2025 at 13:00.

Student number:	5930537
Project duration:	January 1st, 2025 – November 3rd, 2025
Thesis committee:	Prof. Dr. Ir. W. de Jong, TU Delft, Supervisor
	Dr. Ir. L. van Biert, TU Delft, Supervisor
	Ir. B. Grenko, TU Delft, Daily Supervisor
	Prof. Dr. Ir. L. Botto, TU Delft, External Committee

Cover: The Obsidian super-yacht by Feadship, available at `https://www.feadship.nl/fleet/obsidian`.

TU Delft Delft University of Technology

Acknowledgements

This project marks the conclusion of my Master of Science at Delft University of Technology. The main lesson I have learned from this experience is that while the end goal is important, the journey matters even more. Sharing ideas, learning new concepts and discussing different opinions have really broadened my perspective. I arrived unsure about my English and worried about my background, but I leave with much more confidence and awareness, ready to chase my future.

I want to thank my family, who have always believed in me and given me the opportunity and support to be here today. I would also like to thank my supervisors, Prof. Dr. Ir. Wiebren de Jong, Dr. Ir. Lindert van Biert and Ir. Bojan Grenko, for their guidance and support throughout the past ten months. In particular, I am very grateful to Bojan, who always found time for my questions and concerns.

Lastly, I would like to thank all the people I shared this adventure with, from my fellow students in the master's program to my basketball teammates and all the other wonderful people I was lucky to become friend with. The relationships we have built will last forever, even if our paths lead us to different places. You are all welcome to the mountains in Italy for your holidays and weekends.

Filippo Bernardinelli
Delft, November 2025

Abstract

In the context of maritime decarbonization, methanol has emerged as a promising alternative fuel due to its favourable storage properties and potential for renewable production. This thesis investigates the techno-economic performance of integrating methanol steam reforming with low-temperature proton exchange membrane fuel cells (LT-PEMFCs) for on-board power generation on a super-yacht. The primary objective is to conduct a comparative analysis of two distinct system architectures: an integrated membrane reactor where reaction and separation occur simultaneously (Configuration A), and a conventional packed-bed reactor followed by a separate membrane purification unit (Configuration B).

To evaluate these systems, two detailed, steady-state process models were developed using the Aspen Plus V12 simulation software. The core unit operations, including the coaxial membrane reformer and the PEM fuel cell, were modelled using custom-developed User2 Fortran subroutines. These subroutines implement detailed, literature-based models for the MSR kinetics (Peppley et al.), hydrogen permeation (Sieverts' Law), and PEMFC electrochemistry (Correa et al.). The systems were sized to meet a 325 kW net power demand derived from real-world Feadship vessel load data, and comprehensive heat integration strategies were implemented for both.

The simulation results reveal a fundamental trade-off between unit-level conversion efficiency and system-level thermal efficiency across the different power loads. While the membrane reactor (Configuration A) achieved superior methanol conversion due to in-situ hydrogen removal, its fuel-depleted retentate stream necessitated a significant supplementary fuel flow to the burner for heat integration. In contrast, the conventional packed-bed reactor (Configuration B), despite a lower conversion, produced a fuel-rich retentate that greatly improved the effectiveness of its heat recovery loop.

Consequently, Configuration B demonstrated a higher overall system efficiency (59%) and lower specific methanol consumption compared to Configuration A (57%) at the design point. The operational cost analysis further confirmed this advantage, showing lower annual fuel and membrane replacement costs for Configuration B. This study concludes that for an integrated onboard power system where retentate fuel value is critical for thermal self-sufficiency, the conventional reactor with a separate purification unit represents the more efficient and economically viable architecture. Both modelled systems, however, show significant efficiency and emissions advantages over traditional marine diesel engines, validating the promise of methanol-reforming PEMFC technology for sustainable maritime applications.

Contents

List of Figures

List of Tables

Nomenclature

Table 1: List of Chemical Compounds.

Compound	**Formula**
Ammonia	NH_3
Beta-Alumina Solid Electrolyte	BASE
Carbon dioxide	CO_2
Carbon monoxide	CO
Compressed Natural Gas	CNG
Diesel / Marine Gas Oil	$C_{10}H_{20}$–$C_{15}H_{28}$ / MGO
Dimethyl ether	CH_3OCH_3
Fatty Acid Methyl Esters	FAME
Formaldehyde	CH_2O
Formic acid	HCOOH
Halogenated compounds (as Cl)	Cl
Hydro-treated vegetable oil	HVO
Hydrogen	H_2
Hydrogen Sulfide	H_2S
Liquefied petroleum gas	LPG
Methane	CH_4
Methanol	CH_3OH
Nitrogen	N_2
Nitrogen oxides	NO_x
Oxygen	O_2
Palm Fatty Acid Distillate	PFAD
Phosphoric Acid	H_3PO_4
Potassium Carbonate	K_2CO_3
Potassium Hydroxide	KOH
Sulphur dioxide	SO_x
Water	H_2O
Yttria-stabilized zirconia	YSZ

Table 2: List of Abbreviations.

Abbreviation	**Full Name**
AFC	Alkaline Fuel Cell
ATRM	Autothermal Reforming
CAPEX	Capital Expenditure
CEPCI	Chemical Engineering Plant Cost Index
CHP	Combined Heat and Power
CMSMs	Carbon Molecular Sieve Membranes
DME	Dimethyl Ether
GDL	Gas Diffusion Layer
GHG	Greenhouse Gas
HCHO	Formaldehyde
HCOOH	Formic Acid
HHV	Higher Heating Value
HT-PEMFC	High Temperature Proton Exchange Membrane Fuel Cell
ICE	Internal Combustion Engine
KPIs	Key Performance Indicators
LBG	Liquefied Biogas
LHV	Lower Heating Value
LNG	Liquefied Natural Gas
LPG	Liquefied Petroleum Gas
LT-PEMFC	Low Temperature Proton Exchange Membrane Fuel Cell
MCFC	Molten Carbonate Fuel Cell
MD	Methanol Decomposition
MEA	Membrane Electrode Assembly
MGO	Marine Gas Oil
MMMs	Mixed Matrix Membranes
MMRs	Membrane Micro-Reactors
MOFs	Metal-Organic Frameworks
MR	Membrane Reactor
MSR	Methanol Steam Reforming
OPEX	Operational Expenditure
PAFC	Phosphoric Acid Fuel Cell
PBR	Packed-Bed Reactor
PBMR	Packed Bed Membrane Reactor
PBMR-C	Packed Bed Membrane Reactor Cell
Pd-Ag	Palladium-Silver
PEMFC	Proton Exchange Membrane Fuel Cell
POM	Partial Oxidation of Methanol
PSA	Pressure Swing Adsorption
RDS	Rate-Determining Step
RWGS	Reverse Water-Gas Shift
S/C	Steam-to-Carbon Ratio
SOFC	Solid Oxide Fuel Cell
TSA	Temperature Swing Adsorption
VLE	Vapour-Liquid Equilibria
VPSA	Vacuum Pressure Swing Adsorption
WGS	Water-Gas Shift
YSZ	Yttria-Stabilized Zirconia

Table 3: List of Symbols.

Symbol	Description	Unit
ΔH^*	Enthalpy change of adsorption	$kJ \cdot mol^{-1}$
ΔS^*	Entropy change of adsorption	$J \cdot mol^{-1} \cdot K^{-1}$
ε	Bed voidage (void fraction)	-
η_{HHV}	Electrical efficiency (based on Higher Heating Value)	%
η_{sys}	Overall system efficiency	%
λ	Empirical membrane hydration parameter	-
μ	Fluid viscosity	$Pa \cdot s$
μ_f	PEMFC hydrogen utilization factor	%
$\xi_{1..4}$	Semi-empirical coefficients for PEMFC model	-
ρ	Fluid density	$kg \cdot m^{-3}$
A	Active area of a fuel cell	cm^2
B	Parametric coefficient for concentration loss	V
C_p	Specific heat capacity	$J \cdot kg^{-1} \cdot K^{-1}$
C_i	Surface concentration of species i on catalyst sites	$mol \cdot m^{-2}$
d_p	Catalyst particle diameter	m
D_{in}, D_{out}	Inner and outer tube diameter of reformer	m
D_{shell}	Overall shell diameter of the reactor	m
E	Activation energy	$kJ \cdot mol^{-1}$
E_{Nernst}	Ideal Nernst potential of a fuel cell	V
F	Faraday's constant	$C \cdot mol^{-1}$
I_{stack}	Total stack current	A
i_{FC}	Cell operating current	A
J	Hydrogen flux through a membrane	$mol \cdot m^{-2} \cdot s^{-1}$
J	Current density in a fuel cell	$A \cdot cm^{-2}$
J_{max}	Maximum current density	$A \cdot cm^{-2}$
k_j	Rate constant for reaction j	$m^2 \cdot s^{-1} \cdot mol^{-1}$
K_i^*	Adsorption coefficient for species i	$bar^{-0.5}$
l_{tubes}	Length of reactor tubes	m
$\dot{m}$	Mass flow rate	$kg \cdot s^{-1}$
$\dot{n}$	Molar flow rate	$mol \cdot s^{-1}$ or $kmol \cdot h^{-1}$
N_{cells}	Number of cells in a PEMFC stack	-
n	Pressure coefficient in Sievert's law	-
P	Permeability of a membrane	$mol \cdot m^{-1} \cdot s^{-1} \cdot Pa^{-n}$
P, p	Pressure, Partial pressure	bar, Pa, atm
p	Permeance of a membrane	$mol \cdot m^{-2} \cdot s^{-1} \cdot Pa^{-n}$
P_{net}	Net electrical power output	W or kW
P_t	Tube pitch in a shell-and-tube exchanger	m
Q	Heat duty or heat transfer rate	W
r_j	Rate of reaction j	$mol \cdot m^{-2} \cdot s^{-1}$
R_c, R_M	Contact and membrane resistance	Ω
Rec_{H_2}	Hydrogen recovery	%
S_A	Surface area of fresh catalyst	$m^2 \cdot kg^{-1}$
T	Temperature	K or °C
t	Thickness of a membrane	m
U	Overall heat transfer coefficient	$W \cdot m^{-2} \cdot K^{-1}$
V_{act}	Activation voltage loss (overpotential)	V
V_{cell}	Actual cell voltage	V
V_{con}	Concentration voltage loss (overpotential)	V
V_{ohm}	Ohmic voltage loss (overpotential)	V
v_s	Superficial fluid velocity	$m \cdot s^{-1}$
X_{CH_3OH}	Methanol conversion	%
Y_{H_2}	Hydrogen yield	kmol H_2 per kmol CH_3OH
Z	Axial position along the reactor length	m

Chapter 1

Introduction

1 Climate change crisis

The rapid pace of industrialization and urbanization has significantly increased energy consumption and resource depletion, placing immense pressure on the planet's natural systems. Evidence of climate change is undeniable, with global temperatures rising to unprecedented levels, leading to severe environmental consequences. Glacial retreat, illustrates the accelerating impact of warming. Ocean ecosystems are also under threat, with rising temperatures causing widespread coral bleaching and disrupting marine biodiversity. Perhaps the most alarming indicator is the continuous reduction in Arctic sea ice, which has shrunk drastically since 1979 [20], contributing to rising sea levels that threaten coastal regions worldwide. Figure 1.1 illustrates the global surface temperature change relative to the average temperature from 1951 to 1980. This figure highlights how much temperature has risen over the last century.

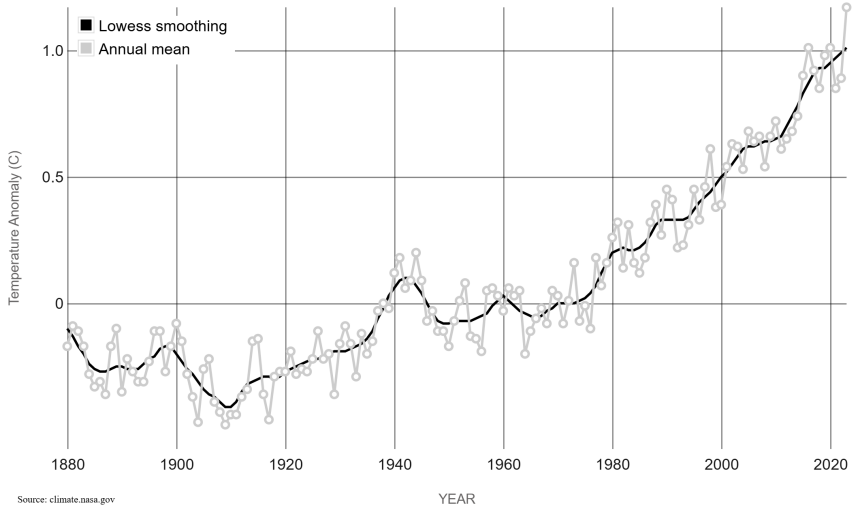

Figure 1.1: Global surface temperature change compared to the long-term average from 1951 to 1980 [1]. Reprinted with permission.

The primary driver of global warming is the increasing concentration of carbon dioxide in the atmosphere, largely due to human activities such as fossil fuel combustion and industrial processes. Since the Industrial Revolution, CO_2 levels have soared beyond any previously recorded values, intensifying the greenhouse effect [21]. While Earth's natural greenhouse effect is essential for maintaining habitable temperatures, excessive CO_2 traps additional infrared radiation, amplifying global warming. This mechanism, combined with emissions from methane and other greenhouse gases, has led to climate patterns that are becoming increasingly erratic and extreme. [22]

Faced with the reality of climate change, humanity has three options: mitigation, adaptation, or suffering. Mitigation involves reducing greenhouse gas emissions through cleaner energy sources and improved efficiency, aiming to slow down the rate of climate change. Adaptation focuses on minimizing damage by implementing protective measures, such as reinforcing sea defences and modifying agricultural practices.

However, failure to act on either front will result in widespread suffering, affecting ecosystems, communities, and economies. The urgency of the crisis demands immediate and sustained mitigation efforts to provide scientists and engineers with the time necessary to develop long-term solutions. [23]

2 The maritime transportation sector

In order to mitigate the causes of climate change, engineers and scientists need to develop long-term solutions. These technologies need to be feasible and effective otherwise our society will need to adapt and suffer due to the consequences of this crisis. The present work aims to contribute to mitigate the causes of climate change offering an engineering technology in the marine transportation sector.

In 2021 according to the Renewals Global Status Report [24], the transportation sector is responsible for 30% of global energy consumption, of which only 3.9% is renewable. Among the others sector of energy demand transportation has the lowest renewable energy rate. To mitigate the climate change consequences it is therefore mandatory to develop this sector with sustainable technologies.

To increase the renewable energy ratio in the transportation sector, the European Union has published new regulations affecting the maritime industry. The FuelEU Maritime Regulation promotes the use of renewable, low-carbon fuels and clean energy technologies for ships, essential to support decarbonisation in the sector. The Regulation is fully applied from 1 January 2025. FuelEU Maritime sets maximum limits for the yearly average greenhouse gas (GHG) intensity of the energy used by ships above 5,000 gross tonnage calling at European ports, regardless of their flag. Targets will ensure that the greenhouse gas intensity of fuels used in the sector will gradually decrease over time, starting with a 2% decrease by 2025 and reaching up to an 80% reduction by 2050 as it shown in Figure 1.2. In fact, more than 55% of all the ships are larger than 5,000 tons and they cover more than 90% of the total CO_2 emissions of the marine sector. However, the targets cover not only CO_2 but also methane (CH_4) and nitrogen oxides (NO_x) emissions over the full lifecycle of the fuels used onboard. Moreover, to reduce air pollution in ports, passenger and container ships at berth or moored at the quayside must use on-shore power supply (OPS) or alternative zero-emission technologies from 1 January 2030 onwards. [2]

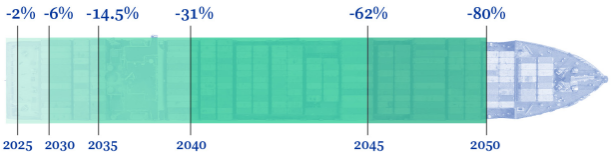

Figure 1.2: Annual average carbon intensity reduction compared to the average in 2020 [2]. Reprinted with permission.

3 Introduction to methanol reforming for maritime applications

The transition towards low-carbon fuels in the maritime sector requires efficient onboard power solutions that balance energy density, storage feasibility, and emissions reduction. While methanol is a promising alternative fuel, its direct use in conventional engines or fuel cells presents challenges due to lower energy density and emission concerns. A viable solution is to convert methanol into hydrogen through methanol steam reforming (MSR), a process that produces hydrogen-rich gas while maintaining relatively low operating temperatures compared to other reforming methods.

Methanol steam reforming involves the catalytic conversion of methanol and steam into hydrogen and carbon dioxide, with minimal carbon monoxide production. This hydrogen can then be fed into a proton exchange membrane fuel cell (PEMFC) to generate electricity efficiently. However, the efficiency of MSR depends on multiple factors, including reactor design, hydrogen separation efficiency, and heat management. Two primary reactor configurations dominate current research: conventional packed-bed reactors with downstream separation units and membrane reactors, which integrate hydrogen production and separation into a single system. Each approach presents unique advantages and limitations, particularly when applied to shipboard energy systems, where space constraints and operational efficiency are critical considerations.

To determine the most effective reactor configuration for maritime applications, a thorough review of existing research is necessary. The following section examines key studies that have explored different MSR reactor designs, hydrogen purification techniques, and their integration with fuel cells, providing a foundation for evaluating their feasibility in shipboard applications.

4 Review of the relevant studies

Hydrogen production from methanol steam reforming has been widely studied, particularly in the context of fuel cell applications. Research has focused on optimizing hydrogen yield, reactor efficiency, and gas purity, with an increasing emphasis on compact, high-performance systems suitable for mobile applications such as ships. A major challenge in methanol reforming is ensuring sufficient hydrogen purity for PEM fuel cells, which are highly sensitive to carbon monoxide and other contaminants. Consequently, reactor configurations and hydrogen separation techniques must be carefully designed to achieve both high conversion efficiency and low impurity levels. Figure 1.3 provides an overview of the process which is the central focus of this work.

Recent studies have explored two main approaches: membrane reactors, which simultaneously produce and purify hydrogen in a single unit, and conventional packed-bed reactors followed by external separation processes. While membrane reactors offer the advantage of continuous hydrogen extraction, shifting the reaction equilibrium toward higher conversion rates, their performance is influenced by membrane permeability, durability, and cost. On the other hand, conventional packed-bed reactors, although more established, require additional gas separation steps, increasing system complexity and energy consumption.

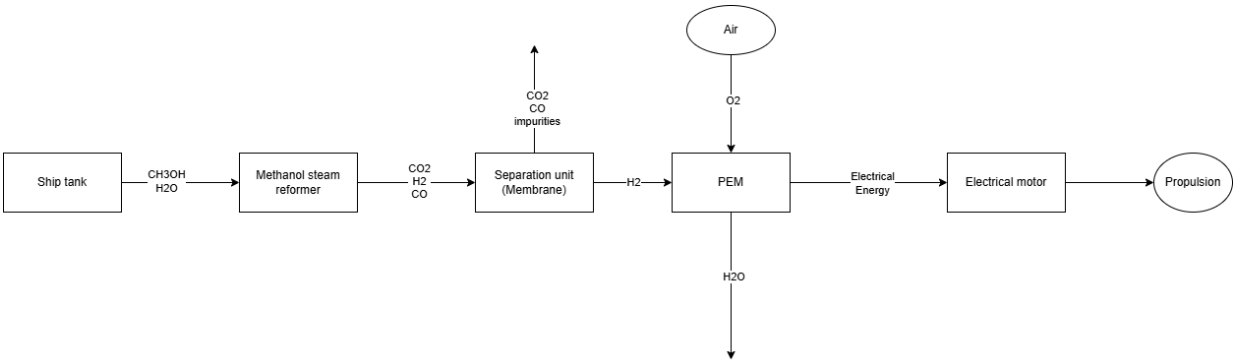

Figure 1.3: A general overview of the methanol to propulsion process.

The study by Sharma et al. [25] laid an important foundation by comparing a membrane reformer to a membrane separator under identical conditions. Their work debunked the common assumption that gas-phase inhibition from CO, CO_2, and steam significantly hinders hydrogen permeation in a membrane reformer, showing that hydrogen flux and purity were nearly identical in both setups. This was a crucial step forward in understanding whether a separation unit is needed at all, or whether a membrane-integrated reactor could be sufficient for high-purity hydrogen production. However, this study was conducted under laboratory conditions, without considering a conventional packed-bed reactor (PBR) followed by a separation unit, which is still the standard approach in industrial and maritime applications. Furthermore, it did not analyse system-wide heat integration, a critical aspect when designing a power system for ships, where energy recovery from exhaust gases and heat exchangers can drastically improve overall efficiency.

To explore a broader range of reactor configurations, Ribeirinha et al. [26] extended the analysis to packed-bed membrane reactors (PBMRs), investigating whether hydrogen-selective membranes (Pd-Ag) or carbon dioxide-selective membranes (ionic liquids) offered better performance. Their findings were particularly relevant because they showed that Pd-Ag membranes greatly enhances methanol conversion by shifting the equilibrium forward, whereas CO_2 removal has only a minor effect on conversion but improves energy efficiency. This study brought valuable insights into the trade-off between conversion efficiency and energy consumption, but its focus remained on high-temperature PEM fuel cells (HT-PEMFCs), which are more tolerant to impurities like CO.

Ribeirinha et al. [27] in a later study investigated a novel approach to methanol steam reforming (MSR) by integrating a packed bed membrane reactor cell (PBMR-C) directly with a high-temperature polymer electrolyte membrane fuel cell (HT-PEMFC), creating a highly compact and efficient hydrogen production system. Their study aimed to address the challenges of thermal management and fuel purity in HT-PEMFCs by designing a system where the endothermic MSR reaction and the exothermic fuel cell electrochemical process could operate in a thermally integrated manner. To enable this, they introduced a thin (4 µm) self-supported Pd-Ag membrane between the reforming catalyst and the membrane electrode assembly (MEA), ensuring hydrogen selectivity while preventing methanol crossover, which can poison the fuel cell anode. This concept allowed the in situ production and purification of hydrogen within a single unit, simplifying system complexity and potentially reducing energy losses compared to conventional

separate reformer-fuel cell configurations.

While the previous studies focused mainly on membrane reactors, Graeeli et al. [28] shifted attention back to traditional packed-bed reactors, analysing how reactor design optimization impacts hydrogen production and CO formation. Their work showed that a co-current reactor configuration could reduce reactor length and construction costs, but at the cost of higher CO production, which is problematic for LT-PEMFC applications. This study was particularly useful in highlighting the trade-offs involved in reactor design. However, it did not fully explore heat integration strategies, which are crucial for maritime applications, where waste heat from reforming and separation processes must be efficiently recovered to improve overall system performance.

5 Research questions

This study aims to produce valuable results that are relevant for real life applications. For this purpose Feadship Royal Dutch Shipyard, provided the power load of one of their super-yachts. This will allow to model this process based on real life data, making the results of this research usable for real life applications. Moreover, this study seeks to address the following research questions:

1. What are the techno-economic trade-offs of implementing a membrane reactor versus a conventional packed-bed reactor with a separation unit for shipboard LT-PEMFC applications?
2. What are the optimal operating conditions and sizes for the methanol steam reformer, the separation unit and the PEMFC for the power demand use cases of the Feadship super-yacht?
3. What are the key challenges and opportunities in integrating heat recovery strategies into the system?

6 Structure of the report

This thesis is organized into nine main chapters to systematically address the research questions. Chapter 2 provides a comprehensive "Theoretical background", beginning with a literature review of alternative marine fuels and fuel cell technologies to establish the context for the methanol-PEMFC pathway. It then delves into the principles of methanol steam reforming and reactor available technologies. Chapter 3, the "Methodology", details the overall simulation strategy and the basis of design. This chapter meticulously describes the development of the custom component models and outlines the sizing and heat integration strategies for the two proposed system architectures (Configuration A and B). Chapter 4, the "Model validation", presents a detailed and rigorous validation for the model against relevant literature. Chapter 5 presents the "Results and discussion", providing a detailed comparative performance analysis of the two configurations across various operating loads. Chapter 6 provides a comparative "Operating cost analysis" based on the simulation results, quantifying the economic drivers of each system. Following the main analysis, Chapter 7 presents the "Conclusion", summarizing the key findings and directly answering the research questions. Chapter 8 transparently discusses the "Model limitations", outlining the key assumptions and simplifications made during the study. Finally, Chapter 9 offers "Recommendations for future work", suggesting pathways for model refinement, dynamic simulation, and further techno-economic investigation.

Chapter 2

Theoretical background

1 Renewable alternatives for the maritime sector

Methanol has been selected as input of this propulsion process. However, several other sustainable energy carriers could have been used. Here a comparative analysis of renewable technologies for ship propulsions will be described. Finally, it will be analysed why methanol has been selected over the others.

Fuels, energy carriers and primary energy sources

Brynolf et al. [13] in their article on sustainable fuels for shipping provide clear definitions of fuels, energy carriers and primary energy sources. These definitions are critical for making complete comparisons between different compounds and technologies in the renewable energy sector for marine applications.

"*Primary energy sources* represent unrefined sources of energy found in nature such as crude oil or biomass and *energy carriers* the "compounds" in the fuel that carry the energy, while the *fuel* is an energy carrier associated with a specific primary energy source and processing option [13]". For instance, liquefied natural gas (LNG) serves as a *fuel*, derived from natural gas, which acts as the *primary energy source*. The relative *energy carrier* is methane (CH_4). Figure 2.1 provides an illustration of these definitions for different fuels, energy carriers and primary energy sources.

This chapter is based on the assumption that each of the different energy carriers discussed has a renewable primary energy source. In fact, most of the energy carriers can be produced both from fossil and form renewable sources. However, since the goal is to reduce green house gases (GHG) emissions it is mandatory to create a sustainable closed loop between energy sources, energy carriers, fuels and emissions. The main renewable energy sources available are biomass, solar, wind, hydroelectric energy and other technologies utilising the energy in moving water (waves, tides, currents etc..).

In the sustainable transportation fuel sector it is possible to divide the fuels in two categories: blue and green fuels. The first ones are considered renewable just partially because during their life cycle some GHG compounds are emitted. On the other hand, green fuels do not emit GHG during their life cycle making them completely sustainable. However, blue fuels can be converted into green, for example by capturing the emission and storing them. This process is typically called Carbon Capture and Storage (CCS).

1.1 Ammonia (NH_3)

In recent years, ammonia has gained attention as a potential marine fuel. Essentially, it serves as an alternative hydrogen storage medium in molecular form (NH_3). At room temperature and atmospheric pressure, ammonia exists as a gas. However, for storage, it must either be cooled below $-33°C$ at atmospheric pressure or compressed to 7.5 bar at room temperature. Compared to both compressed and liquid hydrogen, ammonia has a higher energy density, allowing it to store more energy per unit volume. Traditionally, it is stored in insulated pressurized tanks, which require more onboard space than LNG or methanol [3].

Unlike liquefied hydrogen and LNG, ammonia does not require cryogenic storage, making it easier to handle. The most common production method is the Haber-Bosch (HB) process, which synthesizes ammonia by combining hydrogen (typically from natural gas steam reforming) with nitrogen captured from the air [13].

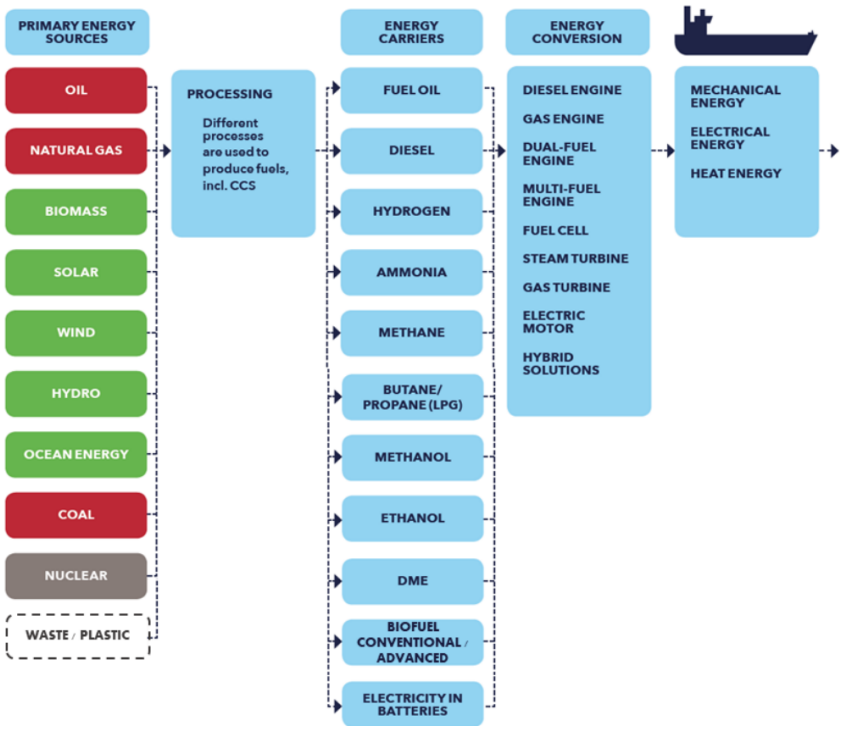

Figure 2.1: Simplified illustration of the chain from energy sources to mechanical energy for marine propulsion [3]. Reprinted with permission.

Efforts are underway to develop renewable ammonia production pathways, primarily through the electrolysis of water using renewable electricity. Ammonia has already been demonstrated as a viable fuel in fuel cells and combustion engines, though some modifications to existing technologies are necessary. For instance, ammonia can be converted into hydrogen for use in PEM fuel cells or used directly in solid oxide fuel cells (SOFCs).

A key advantage of ammonia is that it is a carbon-free fuel, meaning it does not emit CO_2 when burned or utilized in a fuel cell. However, its overall life cycle environmental impact depends on the production method, whether derived from fossil fuels or renewable sources, as well as the efficiency and emissions of the onboard energy conversion system. If ammonia is used in internal combustion engines, it will produce nitrogen oxides (NO_x) and particulate matter during combustion. To mitigate these emissions, catalysts will likely be required [29].

1.2 Hydrogen (H_2)

Hydrogen has a low energy density, even in liquefied form (10,000 MJ/m^3), making it less efficient than LNG (16,000 MJ/m^3) and methanol (22,000 MJ/m^3) for storage and transport [30]. It liquefies at $-253°$C, requiring extensive thermal insulation to minimize boil-off losses. Moreover, hydrogen liquefaction is energy-intensive, consuming approximately 30% of the fuel's final energy content, and involves high capital costs [31]. Developing cryogenic storage tanks for ships remains a key challenge in making hydrogen a viable marine fuel.

Hydrogen can be used in both internal combustion engines (ICEs) and fuel cells, with fuel cells offering higher efficiency. Hydrogen's flammability and wide combustion range pose safety risks, requiring stringent handling measures. Material selection is critical due to hydrogen embrittlement, where absorbed hydrogen weakens metals [32].

As a carbon-free fuel, hydrogen does not emit CO_2 during combustion or fuel cell use. However, NO_x emissions can still form in internal combustion engines [13]. Additionally, the lifecycle emissions depend on the production method, whether hydrogen is derived from fossil fuels or renewable sources. The environmental impact is also influenced by energy conversion efficiency and onboard emission controls [32].

1.3 Electricity (batteries)

Direct electric propulsion with batteries is also a potentially viable option for ships. Fully electric and hybrid vessels are increasingly being adopted, particularly in the short-sea shipping sector, including offshore operations, passenger ferries, and coastal transport.

From an energy efficiency perspective, using electricity directly is more advantageous than converting it into fuel before reconverting it into mechanical or electrical energy. However, batteries present significant challenges for deep-sea shipping, as their volume, weight, low energy density and cost make it challenging to store the large amounts of energy required for long-distance voyages. [13]

1.4 Methane (CH_4)

Methane is the primary energy carrier in natural gas and biogas. To be used as liquefied natural gas (LNG), it must be cooled to $-162°C$ through multiple compression stages and stored in cryogenic insulated tanks. These tanks, while necessary to maintain LNG in liquid form, are significantly more expensive than conventional fuel storage systems [3].

Over the past two decades, LNG has become an increasingly common fuel for internal combustion engines (ICEs) and for direct methane fuel cells. Another option is compressed natural gas (CNG), which requires less energy for compression compared to liquefaction, making it suitable for certain vessel types. However, both LNG and CNG remain fossil fuels, offering limited potential for reducing shipping emissions. A renewable alternative is methane derived from biomass or renewable electricity [33].

Renewable liquefied methane can either replace or be blended with LNG. The most common form is liquefied biogas (LBG), produced via anaerobic digestion of biomass, where raw biogas contains 50–75% methane. Another approach is biomass gasification, while the electro-fuel route synthesizes methane by combining renewable CO_2 with hydrogen from water electrolysis in a methanation reactor [33].

Since methane (CH_4) contains one carbon atom and four hydrogen atoms, its CO_2 emissions are lower than diesel for the same energy output. However, its overall climate impact depends on the production method, whether fossil or renewable-based, and the efficiency of onboard energy converters.

1.5 Diesel-type energy carrier (LPG & HVO)

Several diesel-type fuels are available, including liquefied petroleum gas (LPG) and hydro-treated vegetable oil (HVO), both of which offer alternative fuel options for marine applications.

LPG is defined as any liquid mixture of propane and butane, with specific ratios selected to achieve desired saturation, pressure, and temperature characteristics. Propane is gaseous at ambient conditions, with a boiling point of -42°C, but can be stored as a liquid under moderate pressure (8.4 bar at 20°C). Butane exists in two forms, n-butane and iso-butane, with boiling points of -0.5°C and -12°C, respectively. Due to their higher boiling points, butane isomers require lower storage pressures than propane. For land-based storage, propane tanks are equipped with safety valves to maintain pressures below 25 bar. However, LPG fuel tanks are 2–3 times larger than oil tanks due to the fuel's lower volumetric energy density [3].

LPG is primarily sourced as a by-product of oil and gas production or oil refining, though it can also be produced from renewable sources, such as by-product of renewable diesel production. In marine applications, LPG can be used in two-stroke diesel-cycle engines, four-stroke lean-burn Otto-cycle engines, and gas turbines [3].

HVO is a form of biodiesel with a chemical composition more similar to diesel than fatty acid methyl esters (FAME), making it a drop-in fuel that can be blended with diesel or used at 100% purity with minimal engine modifications. Compared to vegetable oils and FAME, HVO is a more stable fuel, offering longer storage capabilities [13].

HVO can be produced from a range of feedstocks, including palm fatty acid distillate (PFAD), slaughterhouse waste, tall oil, palm oil, and rapeseed oil. Due to its compatibility with existing diesel engines, HVO presents a viable alternative for reducing fossil fuel dependency in the maritime sector [13].

1.6 Dimethyl ether - DME (CH_3OCH_3)

Dimethyl ether (DME, CH_3OCH_3) is a colourless gas at standard temperature and atmospheric pressure. It is considered a redundant fuel for compression-ignition diesel engines, though it has potential in certain marine applications [13].

DME shares similar handling and storage characteristics with ammonia and liquefied petroleum gas (LPG). All three exist as gases under ambient conditions but liquefy under moderate pressure, eliminating the need for cryogenic cooling, unlike LNG or LBG. However, DME has approximately half the volumetric density of Marine Gas Oil (MGO), meaning it requires larger fuel storage tanks to store the same amount of energy [34].

DME can be produced through catalytic methanol dehydration, with methanol sourced from fossil fuels, biogenic feedstocks, or electro-fuel pathways. Additionally, DME can be synthesized directly from syngas, expanding its potential as a renewable or low-carbon fuel option.

As with all carbon-based fuels, CO_2 emissions are released during DME combustion, making its life cycle environmental performance highly dependent on its production route. If derived from renewable sources, DME could significantly reduce overall emissions. One key advantage of DME is its oxygenated molecular structure, which results in low NO_x emissions and minimal soot formation, contributing to improved air quality [13].

1.7 Methanol (CH_3OH)

Methanol is the simplest alcohol, characterized by low carbon content (38%) and high hydrogen content, making it a cleaner alternative to conventional fuels. In comparison, diesel contains 87% carbon [35]. Methanol remains liquid between −93°C to +65°C (176 K to 338 K) at atmospheric pressure, making storage significantly more cost-effective than LNG, hydrogen, and ammonia. Additionally, since methanol is a liquid at standard conditions, it is easy to transport and refuel ships.

However, methanol's lower heating value (19.5 MJ/kg) and lower density mean that it requires approximately 2.5 times the fuel tank volume of Marine Gas Oil (MGO) per unit of energy. Nonetheless, it has a higher energy density than hydrogen, making it a more efficient option for transport and storage [3].

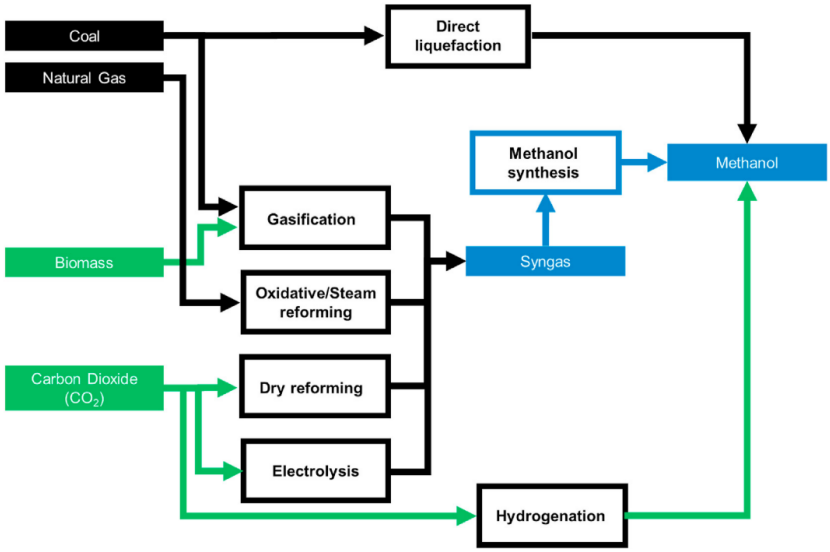

Figure 2.2: Production routes from primary feedstock to methanol [4]. Reprinted with permission.

Methanol can be synthesized from a variety of feedstocks, including natural gas, coal, and renewable sources such as black liquor from pulp mills, forest residues, agricultural waste, and most importantly from electrolysis of water combined with captured CO_2 from power plants or the air. When produced from natural gas, it is typically synthesized through a combination of steam reforming and partial oxidation, achieving energy efficiencies of up to 70%. In contrast, coal gasification provides a cheap and abundant source but results in twice the greenhouse gas (GHG) emissions compared to natural gas-based production. Figure 2.2 provides an highlight of the production routes from primary feedstock to methanol. When produced from electrolysis and CO_2 capture methanol becomes renewable since carbon is not emitted but instead it is stored. [3] [13]

Methanol can be used as fuel in two-stroke diesel-cycle engines as well as in four-stroke lean-burn Otto-cycle engines [3]. Since methanol contains no sulphur, it fully complies with strict sulphur emission regulations. However, its combustion may increase formaldehyde (CH_2O) emissions, which must be managed through proper mitigation measures. [13]

Beyond combustion engines, methanol is also suitable for hydrogen production and therefore fuel cells, including direct molten carbonate fuel cells and solid oxide fuel cells (SOFCs), offering another pathway for efficient energy conversion. In fact, like ammonia and methane, methanol is a storage medium of hydrogen that can be extrapolated later on [13].

Methanol is a flammable and toxic liquid that requires careful handling to ensure safety during its storage and transport. For transportation, methanol is commonly shipped across continents via double-hulled tanker ships, railcars, and tanker trucks, with procedures adapted from those used for other hydrocarbon fuels like gasoline. Special attention must be given to leak detection, fire suppression using alcohol-resistant foams, and the use of materials compatible with methanol. During inland storage, methanol is typically kept in above-ground tanks with floating roofs or baffled containers to minimize vapour emissions and static discharge risks. Grounding, bonding, and vapour control strategies—such as nitrogen blanketing—are implemented to prevent ignition, and flame arresters are installed in venting systems. Facilities must be equipped with leak detection systems, fire suppression equipment, and bermed containment areas capable of holding spill volumes. Safety protocols include strict control of ignition sources, use of explosion-proof equipment, regular maintenance checks, and personnel training. Methanol's low-luminosity flame also necessitates the use of infrared detection during emergency response. [36] [37]

1.8 Comparisons

Table 2.1 shows a summary of the physical properties of the energy carriers discussed in the previous sections.

Table 2.1: Summary of properties of some conventional and potential future energy carriers for ships. L = liquid, G = gaseous. Values vary slightly in literature and depend on the specific conditions of the measurements done. [13]

Fuel	Formula	BP (°C)	Storage (°C)	Pressure (kPa)	Density (kg/m^3)	LHV (MJ/kg)
MGO/Diesel	$C_{10}H_{20}$-$C_{15}H_{28}$[e]	260–371	25	101	840	43
HVO	C_nH_{2n+2}[c]	180–360	25	101	775–758[d]	44
Methane (L)	CH_4	-161.6	-162	101–125	430–470	49
Methanol (L)	CH_3OH	64	25	101	786	19.7
Ammonia (L)	NH_3	-33.3	25	1000–1700	603[a]	18.6–18.8
DME (L)	CH_3OCH_3	-24.9	25–31.5	500–1000	670[b]	28.8
Hydrogen (G)	H_2	-252	25	25000	17.5	120
Hydrogen (L)	H_2	-252	-253	101.3	71	120

[a] Liquid ammonia at 25°C.
[b] At 20°C.
[c] General formula of straight-chain paraffinic hydrocarbons.
[d] Density at 15°C, 1013 bar.
[e] Diesel fuels, not specifically MGO; avg. formula: $C_{12}H_{23}$.

Methanol stands out among alternative marine fuels due to its combination of ease of storage, transport, and environmental benefits. Unlike hydrogen and ammonia, which require cryogenic storage or high pressures, methanol remains liquid at atmospheric pressure and temperatures ranging from -93°C to $+65$°C, making its storage and refueling simpler and more cost-effective. While it has a lower heating value than marine gas oil (MGO), requiring approximately 2.5 times the fuel tank volume for the same energy content, methanol offers a higher energy density than hydrogen, making it more efficient for transport and storage. Compared to ammonia and liquefied natural gas (LNG), methanol avoids the need for specialized storage conditions, reducing infrastructure costs. Furthermore, methanol does not contain nitrogen, ensuring compliance with strict emission regulations and reducing air pollutants such as NO_x and particulate matter. It can be used in both internal combustion engines and fuel cells, with potential for hydrogen extraction through reforming, which makes it a flexible energy carrier. Additionally, methanol is biodegradable and poses a lower environmental risk in case of spills compared to petroleum-based fuels. Based on this characteristics methanol has been selected as energy carrier for the present work.

2 From hydrogen to electricity

Methanol has been chosen as the energy carrier for our process, and it is now time to move to the next step of this on-board ship technology. As shown in Figure 1.3, methanol is stored in the ship's tanks

and then converted into hydrogen inside a reforming reactor. There are several possible methods for this conversion, including partial oxidation, methanol decomposition, auto-thermal reforming, and steam reforming. However, before determining which method is the most suitable, it is essential to establish the boundary conditions. Since methanol is the main input of the reactor, the output must be aligned with the requirements of the fuel cell. To select the optimal reforming process, we need to understand the specific conditions that will allow the fuel cell to operate at its best.

This chapter explores different fuel cell options for on-board ship applications, including alkaline fuel cells (AFC), phosphoric acid fuel cells (PAFC), solid oxide fuel cells (SOFC), molten carbonate fuel cells (MCFC), and proton exchange membrane fuel cells (PEMFC). A detailed comparison between these technologies will be performed focusing on the purity requirements. The findings from this analysis will establish the key parameters for selecting the most suitable methanol reforming method.

2.1 Alkaline fuel cell (AFC)

Figure 2.3 illustrates the working principles of an alkaline fuel cell (AFC), which generates electric power using an alkaline electrolyte composed of potassium hydroxide (KOH) dissolved in water. The key to its operation lies in the movement of hydroxyl ions (OH^-) across the electrolyte, enabling the completion of the circuit and allowing electrical energy to be extracted. [38]

At the anode, hydrogen gas reacts with hydroxyl ions, producing water and releasing electrons. This process, described by the oxidation reaction in Equation 2.1, generates four water molecules and four free electrons. These electrons then travel through an external circuit to reach the cathode, where they participate in a reduction reaction. At the cathode, oxygen molecules combine with water and interact with the incoming electrons, forming hydroxyl ions (OH^-). This reduction reaction, as shown in Equation 2.2, restores the hydroxyl ions in the electrolyte, allowing the fuel cell to keep running.

$$\text{(Oxidation)}\ 2\,H_2 + 4\,OH^- \longrightarrow 4\,H_2O + 4\,e^- \tag{2.1}$$

$$\text{(Reduction)}\ O_2 + 2\,H_2O + 4\,e^- \longrightarrow 4\,OH^- \tag{2.2}$$

Alkaline fuel cells (AFCs) typically operate at temperatures between 60°C and 90°C, making them part of the low-temperature fuel cell category. One of their key advantages is the use of low-cost catalysts, with nickel being the most common choice for accelerating electrochemical reactions at both the anode and cathode. AFCs are known for their high electrical efficiency, reaching around 60%, while their combined heat and power (CHP) efficiency can exceed 80%. They are capable of generating up to 20 kW of electricity, making them a practical and cost-effective option. Their affordability is largely due to the use of potassium hydroxide (KOH) as an electrolyte, a widely available and inexpensive chemical. Additionally, their design is relatively simple, as they do not require bipolar plates. [14]

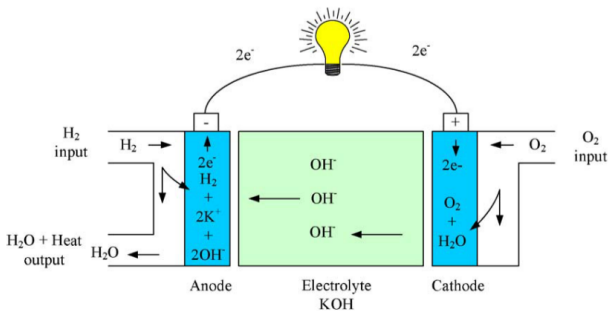

Figure 2.3: Alkaline fuel cell principles of operation [5]. Reprinted with permission.

AFCs consume hydrogen and pure oxygen to produce electricity, heat, and water, with the resulting water being of potable quality. This feature has made them particularly useful in spacecraft and space shuttles, where access to clean drinking water is essential. Moreover, they operate with high efficiency, and produce no greenhouse gas emissions, making them an environmentally friendly energy source. [14]

Despite these advantages, AFCs have a significant drawback: they are highly susceptible to poisoning by carbon dioxide. The water-based alkaline solution used as an electrolyte, potassium hydroxide (KOH), reacts with CO_2, forming potassium carbonate (K_2CO_3), which disrupts the fuel cell's performance. To

mitigate this issue, AFCs typically require purified air or pure oxygen, which increases operating costs. Finding a suitable alternative to KOH remains a challenge. Additionally, AFCs tend to have a relatively short lifespan, further limiting their widespread adoption. [5]

2.2 Phosphoric acid fuel cell (PAFC)

Phosphoric acid fuel cells (PAFCs) utilize carbon paper electrodes and a liquid phosphoric acid (H_3PO_4) electrolyte. Since phosphoric acid has low ionic conductivity at lower temperatures, PAFCs operate within a temperature range of $150°C - 220°C$. The hydrogen ion (H^+), also known as the proton, serves as the charge carrier in this type of fuel cell. These protons move through the electrolyte from the anode to the cathode, while the electrons take a different path, flowing through an external circuit to produce electricity. At the cathode, water forms as a result of the reaction between electrons, protons, and oxygen, with a platinum catalyst facilitating the process. The oxidation and reduction reactions occurring at the anode and cathode, respectively, are represented in Equation 2.3 and Equation 2.4. The working principle of a PAFC is illustrated in Figure 2.4. [39] [40] [14]

$$\text{(Oxidation) } 2H_2 \longrightarrow 4H^+ + 4e^- \tag{2.3}$$

$$\text{(Reduction) } O_2 + 4H^+ + 4e^- \longrightarrow 2H_2O \tag{2.4}$$

The electrical efficiency of PAFCs typically ranges between 40% and 50%, while their combined heat and power (CHP) efficiency can reach approximately 85%. These fuel cells are primarily used for stationary applications, particularly on-site power generation. The higher operating temperature of PAFCs makes them less vulnerable to CO poisoning and other contaminants compared to fuel cells that also rely on platinum catalysts. Unlike other types, PAFCs do not require pure oxygen, as CO_2 does not degrade the electrolyte or hinder performance. They can operate using air and are compatible with reformed fossil fuels. Moreover, H_3PO_4 offers long-term stability and low volatility, contributing to their reliability. [14]

However, the initial cost of PAFC technology is relatively high. Since PAFCs rely on air with only 21% oxygen instead of pure oxygen, the current density is lower by a factor of three. To compensate for this limitation, PAFCs are designed with stack bipolar plates to increase the electrode surface area and enhance energy production. This design choice, while necessary, significantly raises the upfront cost of the system. [39] [40] [14]

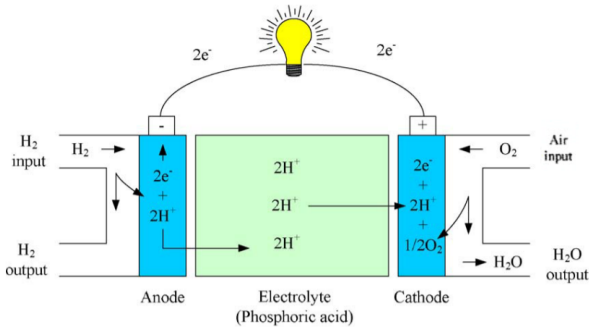

Figure 2.4: Phosphoric acid fuel cell principles of operation [5]. Reprinted with permission.

2.3 Solid oxide fuel cell (SOFC)

Solid oxide fuel cells (SOFCs) are high-temperature fuel cells (500°C-1000°C) that use a solid ceramic electrolyte made of metallic oxides. These fuel cells typically operate with a mixture of hydrogen and carbon monoxide, produced through the internal reforming of hydrocarbon fuels, while air serves as the oxidant. [41] Yttria-stabilized zirconia (YSZ) is the most commonly used electrolyte in SOFCs due to its high chemical and thermal stability, as well as its ability to conduct ions efficiently. At the cathode, oxygen undergoes a reduction reaction, while fuel oxidation takes place at the anode. The anode must be porous to allow fuel to pass through while also facilitating the transport of oxidation products away from the electrolyte and electrode interfaces. [41] [42]

Equation 2.5 and Equation 2.6 present the oxidation and reduction reactions occurring at the anode and cathode, respectively. The working principle of SOFC technology is illustrated in Figure 2.5.

$$\text{(Oxidation)}\ O^{2-}(s) + H_2(g) \longrightarrow H_2O(g) + 2e^- \tag{2.5}$$

$$\text{(Reduction)}\ \frac{1}{2}O_2(g) + 2e^- \longrightarrow O^{2-}(s) \tag{2.6}$$

SOFCs are well suited for large-scale distributed power generation systems, with capacities reaching hundreds of megawatts. The heat produced as a by-product is often utilized to drive gas turbines, enhancing the overall combined heat and power (CHP) efficiency to between 70% and 80%. These systems are known for their reliability, modularity, and adaptability to different fuel sources while emitting low levels of harmful gases such as NO_x and SO_x. SOFCs can serve as local power generation solutions in rural areas that lack access to public electricity grids. Additionally, they operate silently and require minimal maintenance. [14]

However, SOFCs also have certain drawbacks, including long start-up and cooling-down times (dynamic operation not favourable), as well as challenges related to mechanical and chemical compatibility, which limit their broader adoption. [14]

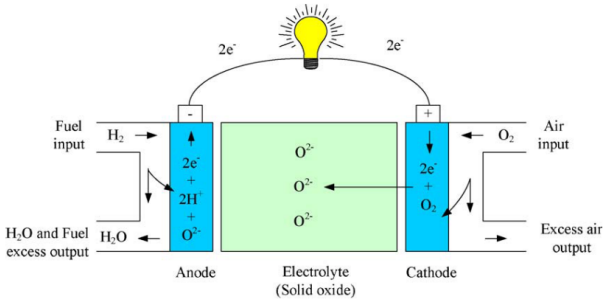

Figure 2.5: Solid oxide fuel cell principles of operation [5]. Reprinted with permission.

2.4 Molten carbonate fuel cell (MCFC)

Molten carbonate fuel cells (MCFCs) operate at high temperatures, around 650°C, and use a molten carbonate salt mixture as the electrolyte. This electrolyte is suspended in a porous, chemically inert ceramic matrix made of beta-alumina solid electrolyte (BASE). In MCFCs, the reaction at the hydrogen electrode involves hydrogen fuel and carbonate ions (CO_3^{2-}), which react to produce carbon dioxide, water, and electrons. [14] The working principles of this type of fuel cell are illustrated in Figure 2.6.

At the anode, the feed gas, typically methane (CH_4) and water (H_2O), undergoes conversion into hydrogen (H_2), carbon monoxide (CO), and carbon dioxide (CO_2). Simultaneously, an oxidation reaction takes place (Equation 2.7), where hydrogen is reduced, generating electrons. This process relies on the carbonate ions (CO_3^{2-}) present in the electrolyte:

$$\text{(Oxidation)}\ H_2 + CO_3^{2-} \longrightarrow H_2O + CO_2 + 2e^- \tag{2.7}$$

At the cathode, a reduction reaction occurs (Equation 2.8), producing new carbonate ions from oxygen (O_2) and carbon dioxide (CO_2). These newly formed carbonate ions then travel through the electrolyte to the anode, completing the electrochemical cycle. The generated electric current and cell voltage can be collected at the electrodes. [14]

$$\text{(Reduction)}\ CO_2 + \frac{1}{2}O_2 + 2e^- \longrightarrow CO_3^{2-} \tag{2.8}$$

MCFCs operate at high temperatures, around 650°C, and within a pressure range of 1 to 10 atm. Each cell generates a voltage between 0.7 V and 1 V. These fuel cells require carbon dioxide and oxygen as reactants, and experimental setups have ranged from 10 kW to 2 MW. Among fuel cell technologies, MCFCs were among the first to be used in practical applications. [5]

One of their advantages is the ability to facilitate internal fuel reforming, generating significant amounts of heat while maintaining a fast reaction rate and high efficiency. However, they are highly sensitive to sulphur contamination. In particular, the anode can tolerate no more than 1.5 ppm of sulphur in the

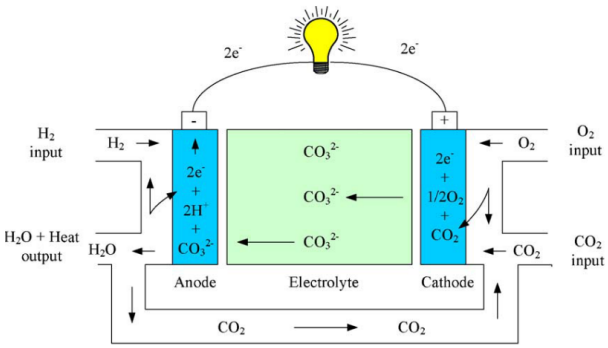

Figure 2.6: Molten carbonate fuel cell principles of operation [5]. Reprinted with permission.

fuel; exceeding this limit leads to a considerable decline in performance. Additionally, MCFCs require preheating before operation, and their liquid electrolyte presents challenges in handling and maintenance. [5]

One of the main advantages of MCFCs is their improved efficiency compared to phosphoric acid fuel cells (PAFCs). While PAFC plants typically achieve efficiencies between 40% and 50%, MCFCs can reach nearly 60%. When waste heat is captured and utilized, overall fuel efficiency can climb as high as 85%, making them a more cost-effective and efficient energy solution. [43]

2.5 Proton exchange membrane fuel cell (PEMFC)

The PEMFC is comprised of bipolar plates and membrane electrode assembly (MEA). In PEMFCs, the hydrogen is activated by catalyst to form proton ion and eject electrons at the anode. The proton passes through the membrane while electron is forced to flow to the external circuit and generate electricity. The electrons then flow back to the cathode and interact with oxygen and proton ion to form water. Figure 2.7 illustrates the working principles of this fuel cell. Equation 2.9 and Equation 2.10 represent the oxidation reaction at the anode and the reduction reaction at the cathode, respectively. [14][44]

The MEA is composed of dispersed catalyst layer, carbon cloth or gas diffusion layer and the membrane. Membrane is to transport protons from anode to cathode and block the passage of electron and reactants. Gas diffusion layer is to access the fuel uniformly. Electrons at anode pass through the external circuit and generate electricity.[44]

$$\text{(Oxidation)}\ \mathsf{H_2(g)} \longrightarrow \mathsf{2\,H^+ + 2\,e^-} \tag{2.9}$$

$$\text{(Reduction)}\ \frac{1}{2}\mathsf{O_2\,(g) + 2\,H^+ + 2\,e^-} \longrightarrow \mathsf{H_2O\,(l)} \tag{2.10}$$

Typically, PEMFCs are low temperature fuel cells with operating temperature between 60°C and 100°C. They are light weight compact systems with rapid start-up process. The sealing of electrodes in PEMFCs is easier than other types of fuel cells because of solidity of the electrolyte. In addition, they have longer lifetime and cheaper to manufacture. [45] From efficiency point of view, the higher the working temperature the higher efficiency can be gained. This is due to the higher reaction rate. Nevertheless, a working temperature above 100°C will vaporize the water causing dehydration to the membrane which leads to the reduction in the proton conductivity of the membrane. Electrical efficiency of PEMFCs is between 40% and 50% and the output power can be as high as 250 kW.[45]

PEMFC systems are usually used in portable and stationary applications. However, among applications of PEMFCs, transportation seems to be the most suitable since they provide continuous electrical energy supply at high level of efficiency and power density. They also require minimum maintenance because there are no moving parts in the power generating stacks of the fuel cells. Fuel cell vehicles are the most promising application of PEMFC systems.[14]

The main advantages of PEMFCs are the use a non-corrosive electrolyte, the tolerance of $\mathsf{CO_2}$ so they can use the atmospheric air, the employment of a solid and dry electrolyte so it eliminates the handling of liquids and the problems of resupply. Moreover, they have high voltage, current and power density. They can work at low pressure (1 or 2 bars), which adds security. [5] [15]

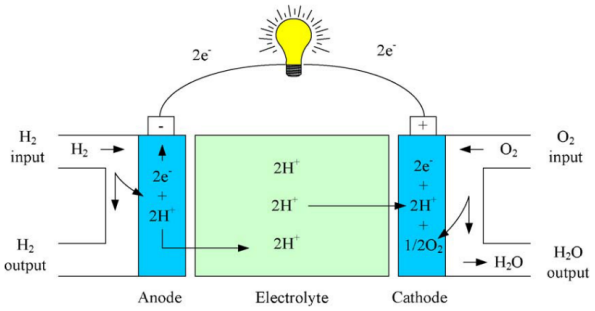

Figure 2.7: Proton exchange membrane fuel cell principles of operation [5]. Reprinted with permission.

On the other hand, they are very sensitive to impurities of hydrogen. In fact they do not tolerate more than 0.2 ppm of CO and they also have a low tolerance to sulphur particles. They need humidification units of reactive gases making water management a critical aspect of this technology. In addition, They use a catalyst (platinum) and a membrane (solid polymer) which are very expensive. [5] [15]

2.6 Comparisons

Among the various fuel cell technologies analysed for on-board ship applications, the Proton Exchange Membrane Fuel Cell (PEMFC) emerges as the most viable option due to its compact design, rapid start-up, and high power density, making it particularly well-suited for maritime environments. In contrast, other fuel cell types present significant drawbacks that limit their practicality in this context. Alkaline Fuel Cells (AFCs), while achieving high electrical efficiency (up to 60%) and using low-cost catalysts, suffer from severe CO_2 poisoning, requiring purified oxygen instead of ambient air, which complicates system integration. Phosphoric Acid Fuel Cells (PAFCs), despite being more tolerant to fuel impurities, operate at relatively high temperatures (150–220°C), necessitating expensive materials that increase their overall cost and complexity. Solid Oxide Fuel Cells (SOFCs) offer impressive efficiencies (up to 65%) and fuel flexibility, but their extreme operating temperatures (500–1000°C) result in long startup times, mechanical stress, and significant thermal insulation requirements. Similarly, Molten Carbonate Fuel Cells (MCFCs), while achieving efficiencies comparable to SOFCs, require temperatures around 650°C, making them unsuitable for rapid load changes and necessitating complex preheating systems.

Table 2.2: Comparison of technical characteristics of fuel cell technologies. [5] [14] [15]

Fuel Cell	**Electrolyte**	**Temp (°C)**	**Eff. (Elec.)**	**Eff. (CHP)**	**Power**	**Strengths**	**Weaknesses**
AFC	Aqueous KOH	60–90	60%	>80%	Up to 20 kW	Low cost, simple, clean by-product, high efficiency, fast cathode reaction	CO_2 poisoning, low power output
PAFC	Liquid H_3PO_4	150–220	40–50%	85%	Up to 200 kW	CO_2 tolerance, long-term stability, heat by-product, impurity tolerance	High initial cost, start-up issues, CO poisoning
SOFC	Solid ceramic (YSZ)	500–1000	50–65%	70–80%	from 100 W to 2 MW	Fuel flexible, low emissions, reliable, quiet, low maintenance, solid electrolyte	High temp, long start-up/cool-down
MCFC	Molten carbonate	600–700	60%	85%	from 10 kW to 2 MW	Fuel flexible, no noble metals, high efficiency, CHP suited	Long start-up
PEMFC	Solid polymer	60–100	40–50%	70–90%	Up to 250 kW	Low temp, lightweight, compact, quick start-up, long life, good sealing, transport-suited	High cost, water management

Unlike high-temperature fuel cells, PEMFCs operate at much lower temperatures (60–100°C), allowing for a lightweight and compact system that responds quickly to load variations, an essential feature for ship propulsion and auxiliary power needs. Their rapid start-up time ensures immediate availability of power, which is crucial for dynamic marine operations. Furthermore, PEMFCs have a solid polymer electrolyte, eliminating the handling issues associated with liquid electrolytes and simplifying maintenance. They also tolerate ambient air as an oxidant, unlike AFCs, which require pure oxygen, and they function at relatively low operating pressures (1–2 bar), enhancing system safety. While their electrical efficiency ranges from 40% to 50%, comparable to PAFCs, they outperform in terms of power density and ease of integration into mobile applications. Additionally, PEMFCs require minimal maintenance since they lack moving parts in their core power-generating stack. Despite challenges such as hydrogen purity sensitivity, the need for humidification, and the high cost of platinum catalysts, their superior adaptability, efficiency, and reliability

make them the preferred choice for our application. Table 2.2, provides a detailed comparison of fuel cell characteristics.

2.7 PEMFC requirements

To be able to proceed onto the next stage of the process it is necessary to highlight the purity requirements of the selected fuel cell type. These level of tolerance will set the boundary condition for the selection of the reforming methods to use where methanol is transformed into hydrogen. Table 2.3 summarise the level of impurities that the PEM fuel cell is able to work with. If these limits are exceeded the efficiency will drop combined with serious damages on the system.

Table 2.3: Typical Maximum Level of Hydrogen Impurities (ISO 14687:2019). [16]

Impurity	**Typical Maximum Level (ISO 14687:2019)**
Hydrogen (H_2) content	≥99.97–99.999% (balance = impurities)
Water (H_2O)	5 ppm
Total hydrocarbons (except CH_4)	2 ppm (on C1 basis)
Methane (CH_4)	100 ppm
Oxygen (O_2)	5 ppm
Inert gases (N_2, He, Ar)	300 ppm (combined)
Carbon dioxide (CO_2)	2 ppm
Carbon monoxide (CO)	0.2 ppm
Total sulphur compounds (asH_2S)	0.004 ppm (4 ppb)
Formaldehyde ($HCHO$)	0.2 ppm
Formic acid ($HCOOH$)	0.2 ppm
Ammonia (NH_3)	0.1 ppm
Halogenated compounds (as Cl)	0.05 ppm

3 From methanol to hydrogen

Methanol has been selected as energy carrier for our process and PEM fuel cells have been chosen to transform hydrogen into electricity. In the previous sections the requirements of this fuel cell type have been deeply highlighted. This will now be the guideline for the selection of the best method to transform methanol into hydrogen. In this chapter multiple options will be investigated such as: partial oxidation, methanol decomposition, auto-thermal reforming and steam reforming. It will also be highlighted why the steam reforming method has been chosen over the others.

3.1 Partial oxidation (POM)

Partial oxidation occurs when fuel and air are partially reacted or combusted in a reactor to generate hydrogen-rich syngas. The amount of air supplied to the reactor is carefully regulated to prevent complete oxidation of hydrocarbons into carbon dioxide and water. By maintaining oxygen levels well below the stoichiometric requirement for full oxidation, the process yields a gas mixture primarily composed of hydrogen and carbon monoxide, along with nitrogen and trace elements. [46]

$$CH_3OH + \frac{1}{2}O_2 \rightarrow CO_2 + 2H_2 \quad \Delta H^\circ = -192.2 \text{ kJ/mol} \tag{2.11}$$

The partial oxidation of methanol is an exothermic reaction (Equation 2.11), eliminating the need for an external energy supply. [47] However, the strong exothermic nature of the reaction complicates temperature control within the reactor, requiring careful reactor design to mitigate the formation of localized hot spots. These hot spots can lead to rapid temperature spikes in the catalytic bed, accelerating catalyst deactivation due to sintering of the active phase. [48]

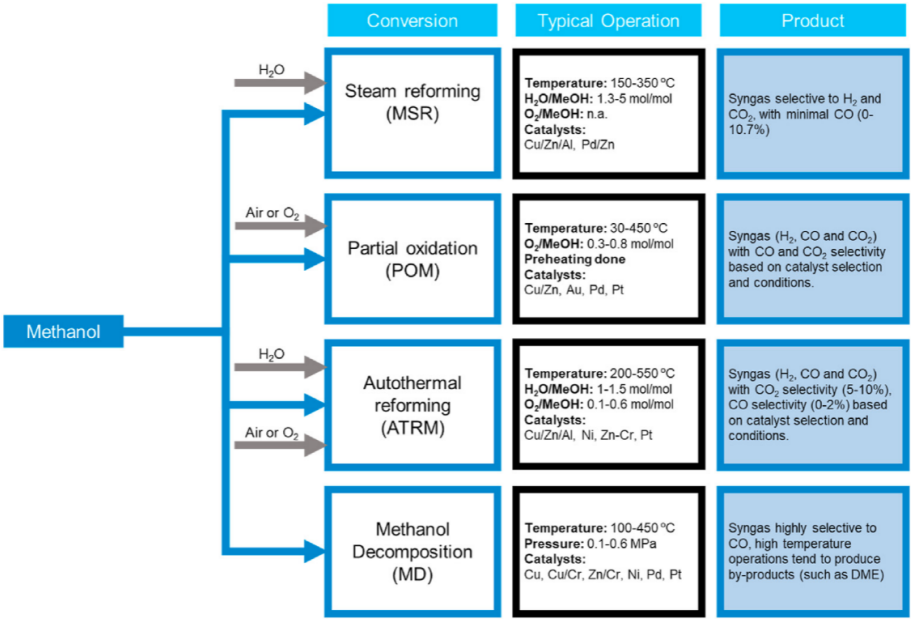

Figure 2.8: A schematic of the thermochemical route for hydrogen production from methanol (MSR, POM, ATRM, MD) [4]. Reprinted with permission.

Recent advancements in POM research have focused on enhancing cold-start capabilities through the development of novel catalysts and optimized reactor designs. However, POM still results in a less favourable H_2/CO_2 ratio compared to methanol steam reforming. The process also poses a significant risk of excessive CO formation due to its inherent difficulty in temperature regulation, further limiting its hydrogen yield compared to reforming-based methods. [17]

Catalyst selection is a critical aspect of POM, with noble and non-noble metals being employed to optimize performance. Copper-based catalysts are the most widely utilized due to their high catalytic activity. Metallic palladium (Pd^0) catalysts have been observed to favour decomposition products (H_2 and CO), whereas Pd-Zn alloys enhance selectivity toward reforming products (H_2 and CO_2), achieving higher methanol conversion rates. Alternative materials such as silver (Ag) and gold (Au) have also been explored for their catalytic potential. [4]

3.2 Methanol decomposition (MD)

Methanol decomposition is a straightforward reaction from a chemical standpoint, as methanol is the sole reactant. Unlike reforming or oxidation processes, MD proceeds to completion at relatively low temperatures but is characterized by significantly slower reaction kinetics. [4]

$$CH_3OH \longrightarrow CO + 2\,H_2 \quad \Delta H^\circ = 90.4 \text{ kJ/mol} \tag{2.12}$$

The strong endothermic nature of the reaction, as shown in Equation 2.12, necessitates a substantial energy input to sustain the process. The resulting gas mixture comprises approximately 67% hydrogen and 33% carbon monoxide, the latter being highly toxic to the anode compartment of low-temperature PEM fuel cells [49]. Moreover, methanol decomposition has slower kinetics compared to the other methods forcing to increase the reactor sizes to achieve the same production. As a result, MD is generally not considered a suitable hydrogen production method for PEMFC. However, its potential lies in its ability to achieve complete methanol conversion at a relatively low temperature of 473 K under atmospheric pressure. [50]

Methanol decomposition can be catalysed by various active metals. Cu-based catalysts are effective at low temperatures, typically operating between 200°C-275°C, while Zn/Cr catalysts perform optimally around 350°C. Pt-based catalysts exhibit the highest activity but require temperatures above 400°C for efficient operation. Initial research on MD catalysts primarily focused on Cu/ZnO systems due to their proven effectiveness in low-temperature methanol synthesis. Cheng [51] investigated the role of ZnO and other metal promoters such as Cr, barium (Ba), and manganese (Mn) in Cu-based catalysts, demonstrating their influence on MD performance at 250°C. [4]

3.3 Steam reforming (MSR)

Methanol steam reforming (MSR) is a catalytic process in which methanol reacts with water vapour to produce hydrogen gas. The reaction typically occurs in the presence of metal oxide catalysts at temperatures ranging from 200°C to 300°C. The key chemical reactions governing the reforming process are given as follows:

$$CH_3OH + H_2O \rightleftharpoons CO_2 + 3\,H_2 \quad \Delta H^\circ = 49.0 \text{ kJ/mol} \tag{2.13}$$

$$CH_3OH \rightleftharpoons CO + 2\,H_2 \quad \Delta H^\circ = 90.4 \text{ kJ/mol} \tag{2.14}$$

$$CO + H_2O \rightleftharpoons CO_2 + H_2 \quad \Delta H^\circ = -41.4 \text{ kJ/mol} \tag{2.15}$$

The overall reaction in Equation 2.13 is the result of two fundamental steps: methanol decomposition (Equation 2.14) and the water-gas shift reaction (Equation 2.15). The interplay between these two reactions determines the extent of intermediate CO formation during the process. Compared to partial oxidation (POM) and autothermal reforming (ATRM), MSR achieves significantly higher hydrogen yields, as demonstrated in Table 2.5 [17]. MSR is characterized by its endothermic nature, high methanol conversion efficiency, selective hydrogen production, and low CO generation, which facilitates easier integration with fuel cells. However, it suffers from slow startup times and requires a continuous heat input to sustain the reaction. [4]

Figure 2.9 provides a schematic representation of a typical MSR system. The reformer reactor is typically followed by a separation unit to isolate CO_2 and H_2. In some configurations, a shift reactor is incorporated to further enhance hydrogen purity by converting residual CO into additional H_2 and CO_2 through the water-gas shift reaction. [4]

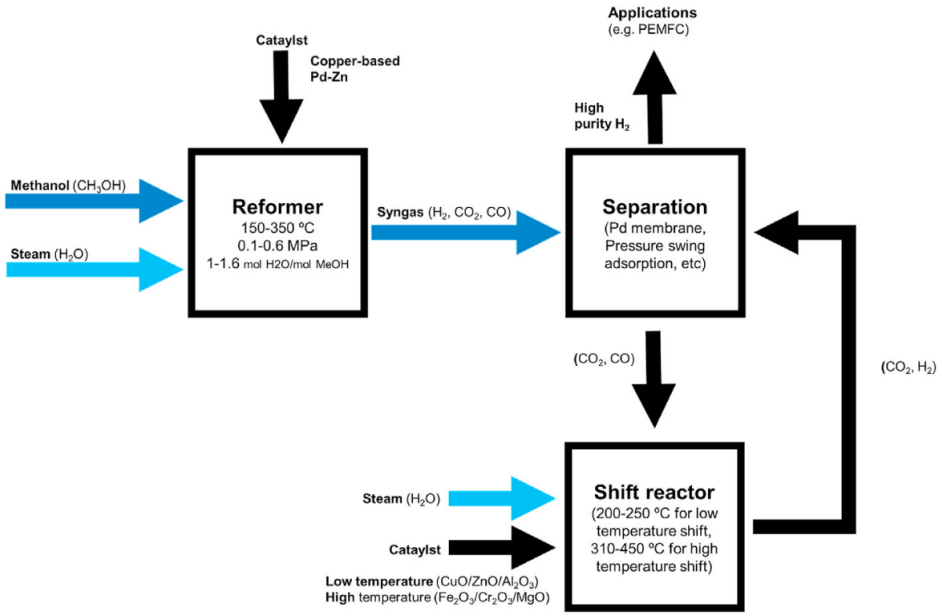

Figure 2.9: A schematic of methanol steam reforming (MSR) process [4]. Reprinted with permission.

The highly endothermic nature of the primary hydrogen-producing reactions (Equation 2.13 and Equation 2.14) necessitates a constant heat supply to maintain reaction progress. This makes MSR inherently less energy-efficient compared to ATRM or POM, although its operating temperature is easier to regulate.

The efficiency of MSR is influenced by key parameters such as reforming temperature (T_{ref}) and the steam-to-carbon ratio (S/C). Faungnawakij et al. [6] conducted a thermodynamic analysis of MSR at varying S/C ratios, temperatures, and pressures. Their findings indicate that complete methanol conversion is achievable at 200°C under a stoichiometric S/C ratio, as depicted in Figure 2.10. Increasing the S/C ratio further enhances methanol conversion at lower temperatures, whereas S/C ratios below 1 result in a sharp decline in conversion efficiency at temperatures below 200°C. However, the S/C ratio can not be increased indefinitely since boiling excess water is energy intensive.

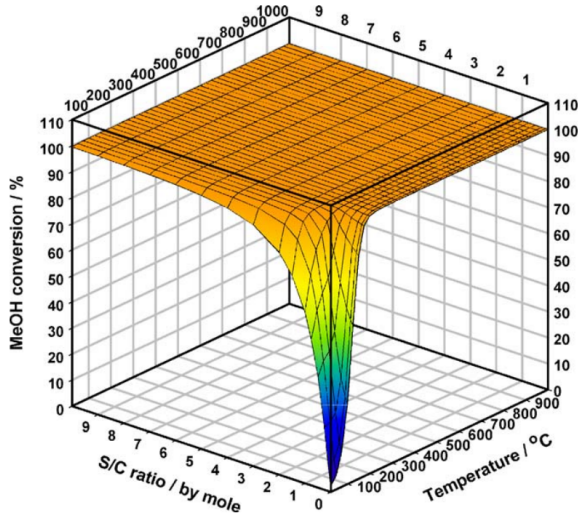

Figure 2.10: Equilibrium conversion of MeOH from MSR as a function of S/C ratio and temperature [6]. Reprinted with permission.

Copper-based catalysts are widely employed in MSR due to their high activity and strong selectivity towards CO_2 over CO, thereby minimizing carbon monoxide formation and making the process suitable for proton exchange membrane fuel cells (PEMFC). [4] Common catalysts include $Cu/ZnO/Al_2O_3$, $Cu/ZnO/ZrO_2$, and $Cu/ZnO/Cr_2O_3$, with $Cu/ZnO/Al_2O_3$ being the most commercially used option. [17]

The performance of MSR catalysts can be further enhanced through the addition of promoters such as zinc, zirconia, ceria, and chromium, which improve catalytic activity and stability. The inclusion of ZrO_2 has been shown to increase the dispersion of Cu crystallites, thereby enhancing catalytic performance. Additionally, catalysts with spinel structures exhibit improved stability and efficiency. Palladium-zinc alloy catalysts have also demonstrated high selectivity for H_2 and CO_2, further improving the effectiveness of the process. [4]

3.4 Autothermal reforming (ATRM)

Autothermal reforming of methanol (ATRM) is a process that integrates both partial oxidation and steam reforming reactions. Methanol reacts with both air and steam to generate a hydrogen-rich gas, utilizing the heat released from the exothermic partial oxidation of methanol (POM) to drive the endothermic methanol steam reforming (MSR) reaction. By carefully balancing the air, steam, and fuel mixture, ATRM can ideally operate at a thermo-neutral point, where no external energy is required to sustain the reaction. [17]

$$CH_3OH + (1 - 2\,r)\,H_2O + r\,O_2 \longrightarrow CO_2 + (3 - 2\,r)\,H_2, \quad 0 \leq r \leq 0.5 \tag{2.16}$$

$$\Delta H^\circ = (-241.8(2r) + 49.5)\ \text{kJ mol}^{-1}, \quad 0 \leq r \leq 0.5 \tag{2.17}$$

The ratio of oxygen to methanol, represented by the variable r in Equation 2.16 and Equation 2.17, can be adjusted to achieve a thermo-neutral or slightly exothermic reaction. However, in practical applications, thermo-neutral ($\Delta H^\circ = 0$ kJ/mol) is not attainable due to inevitable heat losses. As a result, ATRM is typically operated under slightly exothermic conditions to compensate for thermal inefficiencies. [48]

In addition to these reforming reactions, the reverse water-gas shift (RWGS) reaction occurs simultaneously, producing small amounts of CO in the product gas:

$$CO_2 + H_2 \rightleftharpoons CO + H_2O \quad \Delta H^\circ = 41.4\ \text{kJ/mol} \tag{2.18}$$

ATRM enables relatively high hydrogen yields while maintaining moderate reaction kinetics. However, hot spots can form due to the imbalance between local exothermic and endothermic reactions. The exothermic portion of the reaction occurs near the reactor inlet, where partial oxidation takes place, while the endothermic steam reforming reaction consumes the heat further downstream. This uneven heat distribution increases the risk of catalyst sintering, reducing long-term stability. To mitigate this issue, the

oxygen/steam ratio must be carefully optimized; increasing oxygen content enhances the exothermic nature of ATRM, but at the expense of lowering the maximum hydrogen concentration. To suppress the reverse water-gas shift reaction and minimize CO formation, ATRM is typically conducted with an excess of steam, 20–30% more than the stoichiometric requirement. [17]

The catalysts used for ATRM must exhibit high activity under both oxidative and reductive conditions, making them suitable for both POM and MSR. Examples include noble metal catalysts, monolithic catalysts, and the BASF V1765 catalyst, a $CuO/ZnO/Al_2O_3$ formulation modified with ZrO_2 to enhance stability and performance. [4]

3.5 Comparisons

Table 2.4 and Table 2.5 provide a summary of the key features of the different reforming methods described in the previous sections. In Table 2.4 the symbols "+" and "-" represent weather a characteristic of the reforming method is good or bad.

Table 2.4: Comparison of Different Hydrogen Production Processes. [4]

Process	**MSR**	**POM**	**ATRM**	**MD**
H_2 Yield	High (+) from CH_3OH & H_2O.	Low (-), high temp. needed.	Higher than POM (+).	Low (-), slow kinetics.
CO Formation	Low (+), Cu, Pd catalysts.	High (-), poisons PEMFC.	High (-), needs cleanup.	High (-), not ideal for PEMFC.
Process Complexity	Well-known (+), needs heat input (-).	Fast start-up (+), no steam unit (+).	Flexible (+), self-sustained (±).	Endothermic (-), slow adsorption (-).
Catalyst Stability	Well-developed (+), Cu-based.	Stable (+), cold start possible.	Complex (-), needs dual activity.	Cu-based (+), Cr promoters used.

Table 2.5: Operating conditions and typical composition of produced gases in different methanol reforming processes. [17]

	Steam Reforming	**Partial Oxidation**	**Autothermal Reforming**
Water:methanol (molar)	1.5–2	–	1.2–1.5
O_2/methanol	–	>0.5	0.1–0.25
Temp (°C)	200–300	250–350	200–350
Pressure (bar)	3–5	–	–
Catalysts	$Cu/ZnO/Al_2O_3$, $Cu/ZnO/Cr_2O_3$, Pd/ZnO, CuO/CeO_2	$Cu/ZnO/Al_2O_3$, Cu/ZnO, Au/TiO_2, $Cu/Zn/SiO_2$, Cu/Cr	$Cu/ZnO/Al_2O_3$, Cu/ZrO_2/, $Cu/Cr_2O_3/Al_2O_3$
H_2 (%)	70–74	40–41	55–60
CO_2 (%)	22–25	20	22
N_2 (%)	–	21	21
CO (%)	<1	0.1–2	2
By-products	CO, coke, DME	CO, formaldehyde, methyl formate, DME	CO, formaldehyde, DME
Heat (ΔH_f°), kJ/mol	+131	-154.8	-12
Reactions	$CH_3OH + H_2O \rightleftharpoons CO_2 + 3\,H_2$ $CH_3OH \rightleftharpoons CO + 2\,H_2$	$CH_3OH + \frac{1}{2}\,O_2 \rightleftharpoons 2\,H_2 + CO_2$	$CH_3OH + \frac{1}{2}\,H_2O + \frac{1}{2}\,O_2 \rightleftharpoons CO_2 + \frac{1}{2}\,H_2$
Remarks	1. High H_2 yield 2. Less CO 3. Widely used	1. Low H_2/CO_2 ratio 2. High CO output	1. Ideally heat neutral 2. Allows compact reactor

Among the four hydrogen production methods analysed, methanol steam reforming (MSR) emerges as the most suitable option due to its superior hydrogen yield (70-74%) and minimal carbon monoxide (CO) formation (<1%), which is critical for proton exchange membrane fuel cell (PEMFC) applications to avoid catalyst poisoning. The inherently low CO content simplifies gas clean-up, making integration with fuel cells more efficient. Compared to partial oxidation of methanol (POM), which offers faster startup times and does not require an external heat source, MSR achieves nearly double the hydrogen yield (POM: 40-41%) while significantly reducing CO formation (POM: 0.1-2% CO), making it the superior choice for fuel cell applications. Methanol decomposition (MD), though simpler, produces extremely high CO concentrations (33%), requiring additional purification steps that complicate system integration and reduce efficiency. Autothermal reforming (ATRM) balances energy consumption by integrating both exothermic and endothermic reactions, but still produces higher CO levels (around 2%) than MSR, requiring additional treatment to meet PEMFC purity standards. Moreover, MSR operates at a moderate temperature range (200°C-300°C), facilitating efficient heat integration with onboard ship systems while maintaining stable

operation. Its well-established catalyst technology ($Cu/ZnO/Al_2O_3$) ensures long-term reliability, and its high selectivity for hydrogen production makes it the best suited choice for maritime applications where space, energy efficiency, and system compatibility with fuel cells are key considerations. Given these advantages, MSR is the selected hydrogen production method for our project, providing the best trade-off between efficiency, fuel purity, and operational feasibility.

4 Methanol steam reforming reactors

Methanol steam reforming has been chosen over the others methods for transforming methanol into hydrogen. As explained in the previous section its characteristics suits well the requirements of the PEM fuel cell. In this section different types of reactors will be analysed. Conventional bed reactors followed by a purification system will be compared with an integrated membrane reactor, where the purification stage is combed within the reactor itself.

4.1 Conventional packed-bed reactor

The design of the reactor plays a crucial role in determining reaction conversion, and in the case of methanol steam reformers, a tubular configuration is commonly used. Figure 2.11 illustrates a schematic representation of a multi-tubular packed-bed reactor. During operation, a gaseous mixture of methanol and steam is introduced into the catalyst bed of the reformer. The reactants first travel through the bulk fluid to reach the external surface of the catalyst pellets. From there, they diffuse into the pores of the pellets, where the reforming reactions take place on the exposed active sites of the catalyst [7].

Once the reaction occurs, the resulting hydrogen-rich gas is directed to a purification stage, where hydrogen is separated from by-products such as carbon dioxide, carbon monoxide, and other impurities. After purification, the high-purity hydrogen is fed into the anode of a PEM fuel cell stack to generate electricity [7]. The reactor requires an external heat source to maintain the necessary temperature for the reforming process. This heat is transferred into the catalyst bed via a thermal fluid circulating through the shell side of the reactor. In most cases, a burner is employed to provide the required thermal energy, ensuring stable and efficient reactor operation.

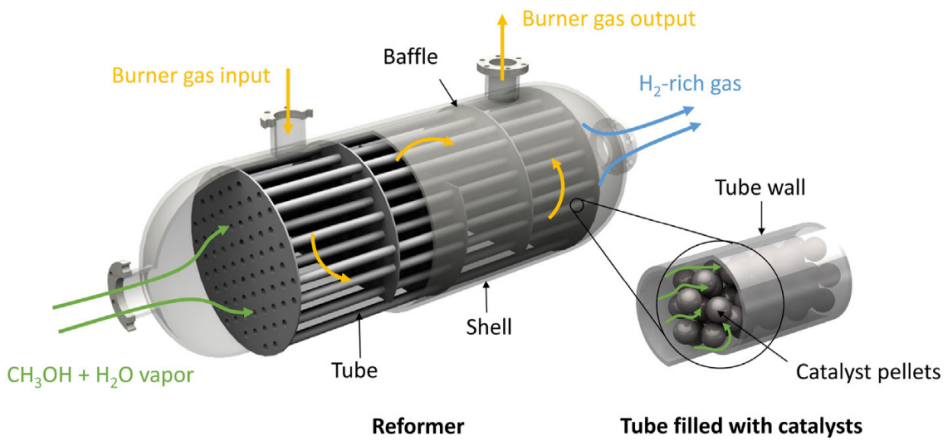

Figure 2.11: Schematic diagram of a multi-tubular packed-bed reactor for methanol steam reforming [7]. Reprinted with permission.

Over the past few decades, several innovative approaches have been developed to enhance the thermal efficiency of reactors. Advances in micro-processing technologies have made it easier to manufacture alternative reactor designs, particularly well-structured flat micro-reactors. These micro-reactors are defined as devices containing micro-structured features, typically with sub-millimetre dimensions, where chemical reactions occur in a continuous manner [8].

Compared to conventional reactors, micro-reactors offer several advantages. Their higher surface-to-volume ratio improves thermal management, while the reduced mean distance between the fluid volume and reactor walls enhances heat and mass transfer properties. Additionally, the controlled flow patterns within these systems can be tailored to match the specific requirements of the reaction. Another key advantage of flat reformers is their compatibility with fuel cell stacks, making them an attractive option for integrated energy systems [8]. For methanol steam reforming, the most commonly used micro-reactor designs include

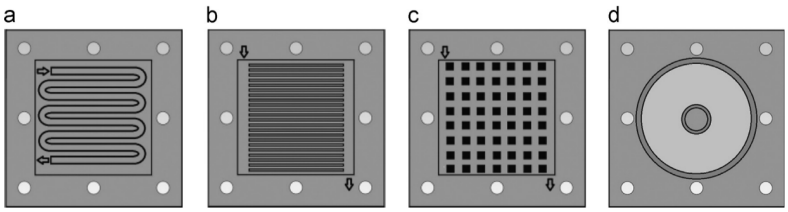

Figure 2.12: Different flow field designs of micro-reactors. (a) coiled-serpentine; (b) Parallel multichannel; (c) Pin-hole; (d) Radial [8]. Reprinted with permission.

rectilinear channels, pin-hole structures, coil-based configurations, and radial designs. Each of these geometries is optimized to improve reaction kinetics, enhance efficiency, and provide better temperature control, further contributing to the overall performance of the reforming process. Figure 2.12 shows a schematic drawing of the four different micro-reactor technologies.

4.2 Purification systems

Hydrogen purification technologies play a crucial role in ensuring high-purity hydrogen for applications such as fuel cells. Various methods operate on different physicochemical principles to separate hydrogen from associated impurities. The H_2 purification methods can be mainly classified as physical and chemical methods. The first category include:

1. Adsorption methods: pressure swing absorption (PSA), temperature swing adsorption (TSA) and vacuum adsorption
2. Low-temperature separation methods: cryogenic distillation and low-temperature adsorption
3. Membrane separation methods: inorganic membrane and organic membrane

While the second category involve a metal hydride separation and catalysis method. Figure 2.13 provide an illustration of classification of the purification methods. [9]

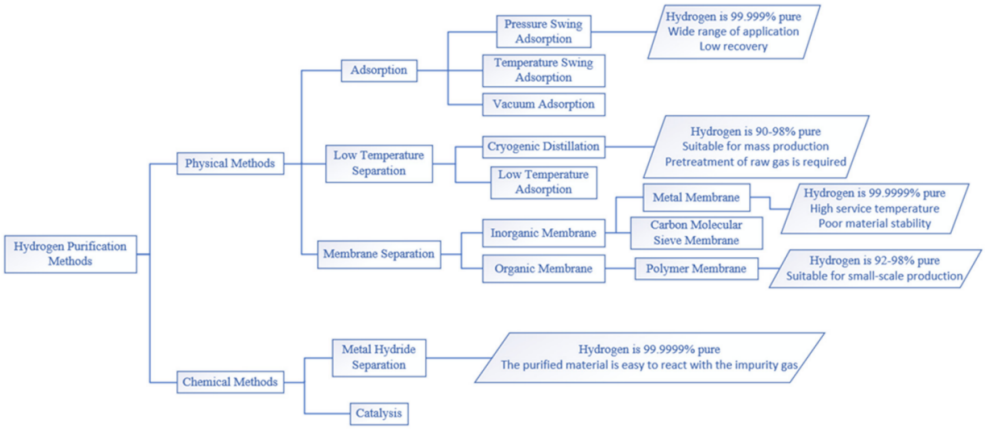

Figure 2.13: Classification of hydrogen purification technologies [9]. Reprinted with permission.

The most widely used physical method is pressure swing adsorption (PSA), which exploits the differential adsorption of gases on a solid adsorbent material by cyclically varying the pressure. This process is particularly suitable for large-scale hydrogen purification from sources such as coal gasification and natural gas reforming due to its industrial feasibility and cost-effectiveness [9]. The efficiency of PSA is highly dependent on the choice of adsorbent materials, ranging from traditional options like zeolites and activated carbons to advanced materials such as metal-organic frameworks (MOFs), which offer enhanced selectivity for removing impurities such as carbon dioxide, carbon monoxide, and methane [9]. Variations in the PSA cycle, including multi-bed systems and vacuum PSA (VPSA), are continuously explored to improve hydrogen purity and recovery rates.

Another key category is membrane separation, where a selective barrier enables hydrogen to permeate at a different rate than other gas components, driven by pressure, concentration, or electrical potential

gradients. Metal membranes, particularly those composed of palladium and its alloys, exhibit excellent hydrogen selectivity and permeability by dissociating hydrogen molecules into protons that diffuse through the metal lattice. Despite their effectiveness, the high cost of palladium and susceptibility to embrittlement have led to research into palladium alloys and supported thin-film membranes to enhance performance and reduce material usage [9]. Other membrane technologies include polymer membranes, which offer flexibility and lower cost but typically face a trade-off between permeability and selectivity. This challenge is often addressed by incorporating inorganic materials into mixed matrix membranes (MMMs). Carbon-based membranes, such as carbon molecular sieve membranes (CMSMs) and graphene-based membranes, show promise due to their tailored pore structures and minimal thickness, allowing for ultra-high selectivity and permeability. Additionally, MOF membranes are being investigated for their tuneable porosity and surface chemistry, which could further enhance hydrogen separation capabilities. [9]

Beyond adsorption and membrane-based methods, metal hydride separation provides an alternative approach by leveraging the reversible absorption and desorption of hydrogen within specific metal alloys. By controlling temperature and pressure, hydrogen can be selectively absorbed into the metal hydride lattice while impurities remain in the gas phase, followed by the controlled release of purified hydrogen. The effectiveness of this method depends on the properties of the hydrogen storage alloy, with ongoing research focusing on improving stability and resistance to impurities [9]. Another advanced technique is cryogenic distillation, which separates hydrogen based on differences in boiling points at extremely low temperatures. While capable of achieving high hydrogen recovery rates, this method is energy-intensive and requires pre-treatment to remove impurities that could solidify and cause operational issues. Given the diverse sources of hydrogen and the stringent purity requirements for fuel cell applications, integrating multiple purification technologies is often necessary to achieve the required hydrogen quality. [9]

4.3 Membrane reactor

Membrane reactors offer a significant advancement in methanol steam reforming by integrating hydrogen production and separation within a single system. This technology allows for a lower operating temperature (typically 100°C lower than conventional reactors) while improving selectivity and nearly eliminating catalyst deactivation due to carbonization. A major advantage of membrane reactors is their ability to continuously remove high-purity hydrogen from the permeate side, effectively shifting the reaction equilibrium to favour hydrogen production. This feature is particularly beneficial for applications requiring ultra-pure hydrogen, such as low-temperature fuel cells, where carbon monoxide impurities must be minimized. [52]

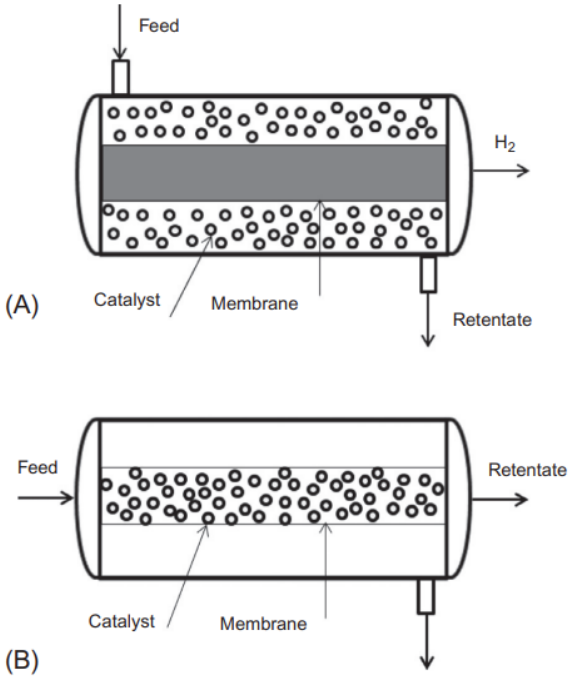

Figure 2.14: Schematic diagram of the membrane reactor [10]. Reprinted with permission.

Among the various membrane materials, palladium-based membranes are widely recognized for their exceptional hydrogen selectivity and permeability. The dissociative adsorption of hydrogen molecules on the membrane surface, followed by diffusion through the metal lattice, enables highly efficient separation.

However, the high cost of palladium and its susceptibility to embrittlement have driven research into alternative materials and composite membranes. Palladium-silver alloys, for example, offer improved durability and permeability, while composite membranes, consisting of a thin palladium layer on a porous substrate, significantly reduce material costs while maintaining high performance [52] . Figure 2.14 shows a scheme of the working participles of a membrane methanol steam reformer [10]. In Figure 2.14 (A) the catalyst is in the shell side of the reactor and the hydrogen is permeated through the tubes of the reactor. On the other hand, in Figure 2.14 (B) the catalyst is in the tube side of the reactor and the hydrogen is permeated to the shell side.

In membrane reactor configurations, different designs serve specific roles in optimizing reaction conditions. Extractor-type membrane reactors selectively remove hydrogen as it is produced, shifting the thermodynamic equilibrium and increasing conversion rates while reducing side reactions. Distributor-type membrane reactors facilitate controlled reactant addition to improve reaction uniformity and mitigate local overheating. Contactors enhance interaction between reactants and catalysts, leading to higher conversion efficiency. Recent developments in membrane micro-reactors (MMRs), which combine the benefits of miniaturized reactor design with membrane separation, have further improved mass and heat transfer, making them promising candidates for compact and efficient hydrogen production systems. [52]

Methanol steam reforming in membrane reactors has been extensively studied, with composite palladium membranes demonstrating high hydrogen selectivity and efficiency. Experimental studies have achieved methanol conversions exceeding 95%, with hydrogen recovery rates of over 90% in certain cases. Efforts to replace palladium with alternative materials such as carbon-based or silica membranes have shown promise, though challenges remain in maintaining high selectivity and stability. Ultimately, membrane reactors represent a highly efficient solution for hydrogen production, addressing both performance and purity challenges while enabling integration with fuel cell technologies. [52]

Chapter 3

Methodology

1 Plan of approach

The literature research has established the theoretical background of the technologies involved in this process. It has also identified the existing research gap and formulated the research questions that this study aims to address. This section outlines the approach taken to tackle these questions based on the theoretical insights gathered. The explicit research question can be seen in Section 5 of Chapter 1.

The process performance will be simulated using ASPEN Plus, where two models will be developed. In the first, the methanol steam reformer will be integrated with a membrane (Configuration A), while in the second, a conventional packed-bed reactor will be coupled with an external separate membrane (Configuration B). Both configurations will supply hydrogen to the same optimized LT-PEMFC model.

A key focus of the study will be on methanol conversion rates and hydrogen recovery in both setups. Additionally, the impact of hydrogen separation in the membrane reactor on reaction equilibrium, CO formation, and overall energy consumption will be examined. The operating conditions of the methanol steam reformer including temperature, pressure, and steam-to-methanol ratio will be optimized to maximize hydrogen yield and minimize energy demand. For the membrane reactor, selectivity and permeability will be fine-tuned to achieve the highest possible hydrogen yield and purity.

Once the core structure of the model comprising the reformer, membrane and PEMFC has been established, a heat management analysis will be conducted. Strategies for heat integration and recovery will be explored to enhance the overall efficiency combined with minimizing the emissions of the process.

The model will also serve as the foundation for a techno-economic analysis. A comparative assessment of both process configurations will be carried out, considering operational expenses, and maintenance requirements. Additionally, the relationship between efficiency, fuel consumption, and overall operating costs (OPEX) will be examined. This analysis will be based on power demand data provided by Feadship, ensuring that the results offer a realistic evaluation of the process's feasibility for onboard ship applications.

2 Basis of design

As previously mentioned, Feadship, a Dutch super-yachts company has agreed on sharing specific power loads data to this study. More specifically the data provided were collected from the journey of one of their super-yachts during one year of use. The specific ship type remains private for privacy. The goal of the company is to investigate and study path for renewable ships. Table 3.1 provides a list of specifications and the use profile of this super-yacht.

To accurately design the process the most relevant data is the power demand profile of the yacht. Feadship has provided two different power loads. Figure 3.1 shows the power load profile of the auxiliary components of the ship. The auxiliary components are not responsible of the propulsion but they represent the power demand of everything else is on-board. Figure 3.2 shows the total power load profile of the design ship which is the sum of the auxiliary and the propulsion loads. The complete profiles and data set are visible in Appendix A.

It is noticeable that the auxiliary load and the propulsion load are on two different scales. It is clear from these profiles that modelling a single process capable of providing both power profiles efficiently and

Table 3.1: Feadship vessel specifications and use profile [11].

Parameter	Value	Unit
Length	87.0	m
Beam	13.5	m
Draught	3.9	m
Displacement	2470	t
Gross Tonnage (GT) volume	3000	t
Maximum speed	18	kn
Range	5000	nm
Max propulsive power	4000	kW
Max auxiliary power	1000	kW
Mean auxiliary load	280	kW
Use profile		
Sailing	10	% of all time
At anchor	33	% of all time
In harbour	57	% of all time

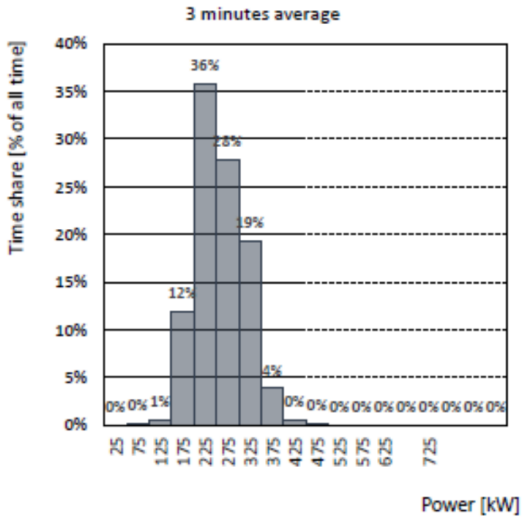

Figure 3.1: Design ship's auxiliary power load profile per time spent [11].

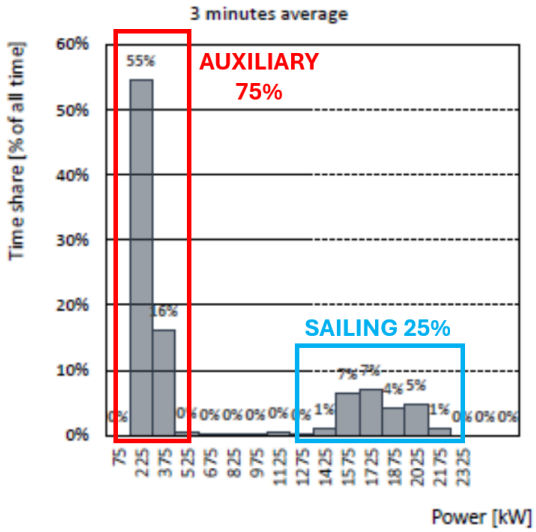

Figure 3.2: Design ship's total power load profile per time spent [11].

effectively is technically difficult. As shown in Figure 3.2, for 75% of the operating time only the auxiliary components are active . On the other hand when sailing (25% of the time) the ship consumes the highest amount of power. Therefore, for the state of this process the auxiliary load has been selected as boundary condition to satisfy. It is important to notice that this process could be scaled up to meet the power demand of the propulsion, therefore the decision of focusing on the auxiliary power demand is a design choice. Moreover, it is noticeable from Figure 3.1 that 95% of the time share of the auxiliary power demand is below 325 kW. Therefore, P=325 kW has been selected as benchmark for the process design optimization and sizing. This means that the system will be sized accordingly to match this power target. However a sensitivity analysis of the entire spectrum of Figure 3.1 will be performed (between 70 kW and 375 kW). In real life applications the system will need to have auxiliary batteries to cover for the 5% power that the system might not be able to cover. Those batteries are not modelled in this process and are outside the scope of the research.

3 Simulation strategy and setup

This section outlines the detailed methodology employed to simulate, analyse, and compare two distinct process configurations for this application. The primary tool for this investigation is the Aspen Plus V12 process simulator, coupled with custom-developed Fortran models.

The primary objective of this thesis is to conduct a techno-economic comparison of two promising system architectures for on-board power generation from methanol:

- **Configuration A: Integrated Membrane Reactor (MR) System:** This configuration utilizes a custom-modelled membrane reformer that performs methanol steam reforming and hydrogen separation simultaneously within a single unit operation. The system is then integrated with a low temperature PEM fuel cell. See Figure 3.3.
- **Configuration B: Packed Bed Reactor + Separation (PBR+S) System:** This configuration represents a more traditional approach, employing a conventional packed-bed reformer followed by a separate, dedicated hydrogen purification membrane unit. Similarly to configuration A, the system is then integrated with a low temperature PEM fuel cell. See Figure 3.4.

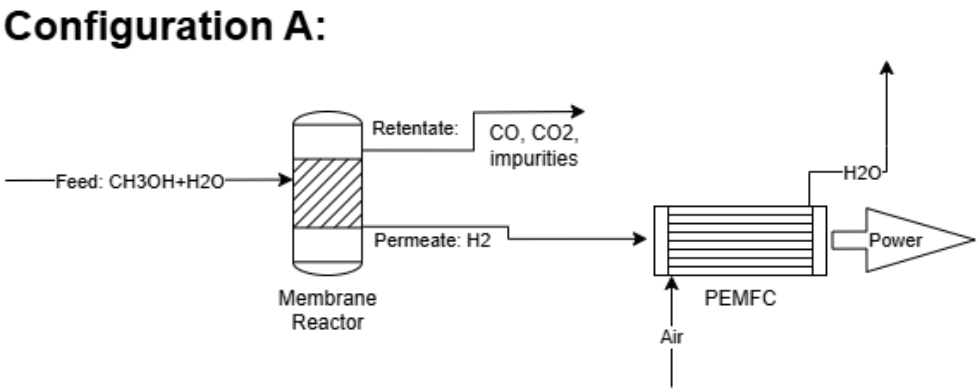

Figure 3.3: Block flow diagram Configuration A.

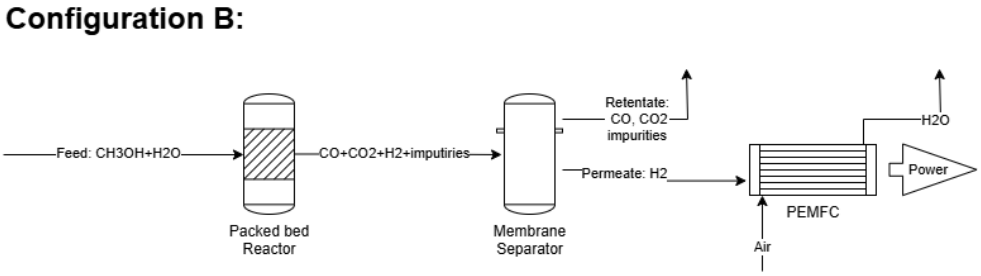

Figure 3.4: Block flow diagram Configuration B.

Due to the absence of built-in high-fidelity models in Aspen Plus, the components of both configurations were built using a custom modelling approach. This involved developing user-defined subroutines in the Fortran programming language to represent the core physics of these units. This strategy allows for a rigorous implementation of literature-based kinetic and electrochemical models, providing a robust foundation for system analysis.

Figure 3.5 shows the three basic main steps on how to link ASPEN Plus with an external Fortran subroutine code. Microsoft Visual Studio is the environment where the code is developed. To write the code several rules and specific structures must be followed for ASPEN Plus to communicate with the code. The specific rules are taken from the ASPEN Plus User Models manual [53]. The code is then compiled through the Intel Fortran Compiler (oneAPI) which converts the code into the machine language that ASPEN Plus is capable of reading. Finally the compiled code is linked with ASPEN Plus in the settings of the software.

The ASPEN Plus User Models manual [53] provides the structures for each different user type subroutine that it is needed to build. In the case of this project: in Configuration A both the membrane reactor and the PEMFC were model with a User2 subroutine type. Similarly in Configuration B the membrane separation

unit and the PEMFC were also modelled with a User2 subroutine type. The only main component modelled with an Aspen Plus tool is the conventional packed bed reactor where an R-plug reactor is used but the kinetic modelling of the reactions is still a custom user made Fortran subroutine.

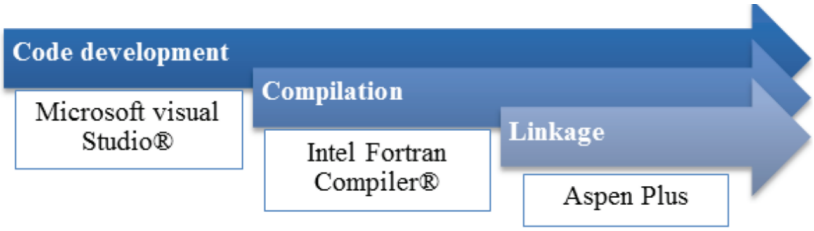

Figure 3.5: Basic steps for the development of a Fortran user model.

The User2 subroutine file can be visualised as a black box where streams come in and out. The Fortran code is then responsible of calculating the resulting properties and operating conditions of the outlet streams. On the other hand, the R-Plug reactor type can be visualised as a typical plug flow reactor. This is a common design choice for this type of reactions.

3.1 Thermodynamic property package

The equation of state used to model the process steps within the Aspen models is an important decision. Accurate material properties and interactions ensure realistic material and energy transfer, and thus realistic process modelling. The Peng-Robinson (PR-BM) equation of state with the Boston-Mathias alpha function was selected as the global thermodynamic property package for this study. This package is well-suited for vapour-liquid equilibria (VLE) involving the light gases (H_2, CO, CO_2, N_2, O_2, Ar), water, and methanol present in the system. It provides accurate predictions of phase behaviour and thermodynamic properties such as enthalpy and entropy over the wide range of temperatures and pressures encountered.

It is important to note that, in the User2 blocks of the Aspen Plus model, the choice of thermodynamic property package is irrelevant. This is because each User2 block functions as a black box that executes custom user-defined code. Consequently, the thermodynamic assumptions implemented within the Fortran code effectively define the property package used in that block. In contrast, the Peng–Robinson equation of state is applied to the R-plug reactor and all other auxiliary equipment that are not User2 blocks. Later in this Methodology chapter, each User2 block will be discussed in a dedicated section summarising the specific thermodynamic assumptions used to characterise its properties.

4 Component models

The ASPEN Plus models developed in this work do not aim to create customized kinetic, electrochemical, or separation models for the system components. Instead, the focus is on optimizing each section of the process and ensuring effective integration between them. Consequently, the component-specific models will be adopted from literature. This section provides a description of the base model used for each main component.

4.1 Reactor kinetic model

$Cu/ZnO/Al_2O_3$ has been selected as the catalyst material for the reactor pellets. Most recent simulation studies on methanol steam reforming using $Cu/ZnO/Al_2O_3$ as a catalyst rely on the kinetic model developed by Peppley et al. [54] in 1999. This model accounts for surface mechanisms on the catalyst for all three primary reactions occurring within the reactor: methanol steam reforming (MSR), methanol decomposition (MD), and the water-gas shift reaction (WGS). Since all three reactions take place simultaneously, each requires an individual kinetic rate, which this model explicitly considers.

The key features of this kinetic model are:

1. Hydrogen adsorption does not compete for the active sites where oxygen-containing species adsorb.
2. Separate active sites exist for methanol decomposition, distinct from those responsible for the methanol-steam reaction and the water-gas shift reaction.
3. The rate-determining step (RDS) for both the methanol-steam reaction and methanol decomposition is the dehydrogenation of adsorbed methoxy groups.

4. The RDS for the water-gas shift reaction is the formation of an intermediate formate species.

Experimental rate data for this model were obtained over a wide range of conditions using a packed-bed differential reactor.

The rate expressions for key reactions involved in the MSR process are provided below, based on the Langmuir-Hinshelwood kinetic model published by Peppley et al. [54]:

Methanol–steam reaction:

$$r_R = \frac{k_R K^*_{\mathsf{CH_3O}^{(1)}} \left(\frac{p_{\mathsf{CH_3OH}}}{p_{\mathsf{H_2}}^{1/2}}\right) \left(1 - \frac{p_{\mathsf{H_2}}^3 p_{\mathsf{CO_2}}}{k_R p_{\mathsf{CH_3OH}} p_{\mathsf{H_2O}}}\right) C_{S_1}^T C_{S_{1a}}^T}{\left(1 + K^*_{\mathsf{CH_3O}^{(1)}} \left(\frac{p_{\mathsf{CH_3OH}}}{p_{\mathsf{H_2}}^{1/2}}\right) + K^*_{\mathsf{HCOO}^{(1)}} p_{\mathsf{CO_2}} p_{\mathsf{H_2}}^{1/2} + K^*_{\mathsf{OH}^{(1)}} \left(\frac{p_{\mathsf{H_2O}}}{p_{\mathsf{H_2}}^{1/2}}\right)\right) \left(1 + K^{1/2}_{\mathsf{H}^{(1a)}} p_{\mathsf{H_2}}^{1/2}\right)} \tag{3.1}$$

Water-gas shift reaction:

$$r_W = \frac{k^*_W K^*_{\mathsf{OH}^{(1)}} \left(\frac{p_{\mathsf{CO}} p_{\mathsf{H_2O}}}{p_{\mathsf{H_2}}^{1/2}}\right) \left(1 - \frac{p_{\mathsf{H_2}} p_{\mathsf{CO_2}}}{k_W p_{\mathsf{CO}} p_{\mathsf{H_2O}}}\right) C_{S_1}^{T^2}}{\left(1 + K^*_{\mathsf{CH_3O}^{(1)}} \left(\frac{p_{\mathsf{CH_3OH}}}{p_{\mathsf{H_2}}^{1/2}}\right) + K^*_{\mathsf{HCOO}^{(1)}} p_{\mathsf{CO_2}} p_{\mathsf{H_2}}^{1/2} + K^*_{\mathsf{OH}^{(1)}} \left(\frac{p_{\mathsf{H_2O}}}{p_{\mathsf{H_2}}^{1/2}}\right)\right)^2} \tag{3.2}$$

Decomposition reaction:

$$r_D = \frac{k_D K^*_{\mathsf{CH_3O}^{(2)}} \left(\frac{p_{\mathsf{CH_3OH}}}{p_{\mathsf{H_2}}^{1/2}}\right) \left(1 - \frac{p_{\mathsf{H_2}}^2 p_{\mathsf{CO}}}{k_D p_{\mathsf{CH_3OH}}}\right) C_{S_2}^T C_{S_{2a}}^T}{\left(1 + K^*_{\mathsf{CH_3O}^{(2)}} \left(\frac{p_{\mathsf{CH_3OH}}}{p_{\mathsf{H_2}}^{1/2}}\right) + K^*_{\mathsf{OH}^{(2)}} \left(\frac{p_{\mathsf{H_2O}}}{p_{\mathsf{H_2}}^{1/2}}\right)\right) \left(1 + K^{1/2}_{\mathsf{H}^{(2a)}} p_{\mathsf{H_2}}^{1/2}\right)} \tag{3.3}$$

where r_j (mol m^{-2}s^{-1}) denotes the rate of reaction j ($j = R, W, D$), k_j (m^{2}s^{-1}mol^{-1}) is the rate constant of reaction j, K_i^* (bar$^{-0.5}$) is the adsorption coefficient for species i, p_i (bar) is the partial pressure of component i. $C_{S_1}^T$, $C_{S_{1a}}^T$, $C_{S_2}^T$, and $C_{S_{2a}}^T$ (mol m^{-2}) represent the surface concentrations of the hypothetical active sites, where '1' and '1a' sites are for the MSR and WGS reactions, and '2' and '2a' sites are for the MD reaction.

Table 3.2: Parameters for rate constants in the comprehensive kinetic model.

Rate constants	**Kinetic parameters**	
	k^∞ (m^{2}s^{-1}mol^{-1})	E (kJ mol^{-1})
k_R (m^{2}s^{-1}mol^{-1})	7.4×10^{14}	102.8
k_D (m^{2}s^{-1}mol^{-1})	3.8×10^{20}	170.0
k_W (m^{2}s^{-1}mol^{-1})	5.9×10^{13}	87.6

Table 3.3: Parameters for adsorption coefficients in the comprehensive kinetic model.

Adsorption coefficients	**Kinetic parameters**	
	ΔS^* (J mol^{-1}K^{-1})	ΔH^* (kJ mol^{-1})
$K^*_{CH_3O_{(1)}}$ (bar$^{-0.5}$)	−41.8	−20.0
$K^*_{OH_{(1)}}$ (bar$^{-0.5}$)	−44.5	−20.0
$K_{H(1a)}$ (bar$^{-0.5}$)	−100.8	−50.0
$K^*_{HCOO_{(1)}}$ (bar$^{-0.5}$)	179.2	100.0
$K^*_{CH_3O_{(2)}}$ (bar$^{-0.5}$)	30.0	−20.0
$K^*_{OH_{(2)}}$ (bar$^{-0.5}$)	30.0	−20.0
$K_{H(2a)}$ (bar$^{-0.5}$)	−46.2	−50.0

Table 3.2 and Table 3.3 provide the selected parameters for the complete model. All the equations and parameters of the reactor kinetic model are available in Appendix B.

4.2 Membrane permeation model

In subsection 4.3 of Chapter 2 an inorganic membrane made of palladium (Pd) has been selected as the type of membrane for this process. The mechanism of H_2 permeation of this technology is based on the concepts of: surface adsorption and desorption, diffusion within the metal and external mass transfer.

The general equation that regulates the permeation is Sievert's law:

$$J = \frac{P}{t}\left(P_1^n - P_2^n\right) \tag{3.4}$$

$$p = P/t \tag{3.5}$$

where J $(molm^{-2}s^{-1})$ is the hydrogen flux, P $(molm^{-1}s^{-1}Pa^{-n})$ is the permeability of the membrane to respect of the hydrogen, t (m) is the thickness of the membrane, n is the pressure coefficient (typically $n = 0.5$) and P_1, P_2 are the hydrogen partial pressure on the high/low pressure sides of the membrane. Typically the ratio of the permeability and thickness can be condensed in a singular parameter called permeance p $(molm^{-2}s^{-1}Pa^{-n})$.

4.3 PEM fuel cell electro-chemical model

Several electro-chemical models for PEM fuel cells are available in literature. To select the best suited model for this project application it is important to first chose the level of complexity, details and duplicability. Sinurat et al. [55] defined a very simple steady-state model which they have also implemented in Aspen Plus. Their model uses relatively straightforward equations for the thermodynamic potential and the different voltage losses. Corrêa et al. [12], Xu and Xiao [56], Mogorosi et al. [57] developed quite similar models where the steady-state response in coupled with the dynamic response.

Corrêa et al. [12] has been chosen as the model to follow over the others thanks to the high level of details that makes the model easier to replicate and implement.

The main equation of the PEMFC model is:

$$V_{\text{cell}} = E_{\text{Nernst}} - V_{\text{act}} - V_{\text{ohm}} - V_{\text{con}} \tag{3.6}$$

The actual cell potential (E_{Nernst}) is decreased from its ideal potential because of several types of irreversible losses. V_{act} is the voltage drop due to the activation of the anode and cathode (also known as activation overpotential), a measure of the voltage drop associated with the electrodes. V_{ohm} is the ohmic voltage drop (also known as ohmic overpotential), a measure of the ohmic voltage drop resulting from the resistances of the conduction of protons through the solid electrolyte and the electrons through its path. Finally, V_{con} represents the voltage drop resulting from the reduction in concentration of the reactants gases or, alternatively, from the transport of mass of oxygen and hydrogen.

$$E_{\text{Nernst}} = 1.229 - 0.85 \times 10^{-3}(T - 298.15) + 4.3085 \times 10^{-5} T \left[\ln(P_{\text{H}_2}) + \frac{1}{2}\ln(P_{\text{O}_2})\right] \tag{3.7}$$

Where T is the cell temperature in Kelvin, and P_{H_2} and P_{O_2} are the reactant partial pressures in atmospheres (atm).

$$V_{\text{act}} = -\left[\xi_1 + \xi_2 T + \xi_3 T \ln(C_{\text{O}_2}) + \xi_4 T \ln(i_{\text{FC}})\right] \tag{3.8}$$

Where i_{FC} is the cell operating current (A) and the ξ terms are semi-empirical coefficients. The concentration of oxygen at the catalyst interface, C_{O_2} in (mol/cm^3), is determined by:

$$C_{\text{O}_2} = \frac{P_{\text{O}_2}}{5.08 \times 10^6 \cdot e^{(-498/T)}} \tag{3.9}$$

$$V_{\text{ohm}} = i_{\text{FC}} \cdot (R_M + R_C) \tag{3.10}$$

where R_C is the constant contact resistance and R_M is the resistance of the proton exchange membrane. R_M is dependent on the membrane's specific resistivity, thickness, and active area, and was calculated using the empirical correlation for Nafion membranes provided by the authors (Corrêa et al. [12], Eq. 10).

$$V_{\text{con}} = -B \cdot \ln\left(1 - \frac{J}{J_{\text{max}}}\right) \tag{3.11}$$

where J is the current density (A/cm^2), J_{max} is the maximum current density, and B is a parametric coefficient.

Table 3.4: Fixed parameters of the electrochemical model from Table 2 of Corrêa et al. [12].

Parameter	Value	Parameter	Value
T_{op}	353 K	ξ_1	-0.948
P_{H_2}	1.47628 atm	ξ_2	$0.00286 + 0.0002 \ln A + (4.3 \cdot 10^{-5}) \ln c_{H_2}$
P_{O_2}	0.2095 atm	ξ_3	$7.22 \cdot 10^{-5}$
t_{memb}	25 μm	ξ_4	$-1.0615 \cdot 10^{-4}$
B	0.15 V	λ	23
R_C	0.0003 Ω	J_{max}	672 mA/cm^2

Table 3.4 shows the fixed parameters that I used to build the electrochemical model of the PEMFC. These values are directly taken from Table 2 in the paper of Corrêa et al. [12].

5 Models design assumptions

5.1 PEMFC design assumptions

The PEMFC model is built upon a set of core assumptions that enable a robust, system-level analysis while maintaining computational tractability. These assumptions, which define the model's operational domain and limitations, are outlined below in a logical progression from the overall system scope to the detailed electrochemical level:

System-level operational framework

These assumptions define the overall state and boundaries of the fuel cell stack.

1. **Steady-state operation:** The model calculates the performance of the fuel cell at a steady, constant operating point for a given current density. It does not account for transient effects like start-up, shut-down, or the dynamics of the charge double-layer capacitance.
2. **Isothermal and isobaric stack:** The entire fuel cell stack is assumed to operate at a single, uniform temperature ($T_{\text{OP\_K}}$) and pressure ($P_{\text{AN\_ATM\_OP}}/P_{\text{CAT\_ATM\_OP}}$). This implies a perfect thermal management system and negligible pressure drops within the cell's flow channels. All outlet streams are assumed to exit at this operating temperature.

Fluid and transport properties

These assumptions govern the behaviour of gases and water within the system.

1. **Ideal gas behaviour:** The partial pressures of reactants (H_2 andO_2) at the catalyst interface, crucial for the Nernst and activation loss calculations, are determined using the ideal gas law ($P_i = Y_i \cdot P_{\text{total}}$).
2. **Simplified feed and water management:** To focus on the core electrochemical performance, the complex multi-phase flow and water transport phenomena are simplified:
   - *Dry feed gas assumption:* The anode (H_2) and cathode (Air) feed streams are assumed to be dry (zero relative humidity).

- *Implicit membrane hydration:* The model does not explicitly calculate the water content profile across the membrane. Instead, it relies on an empirically fitted parameter, $\lambda = 23$, from the Corrêa et al. [12] model. This assumes the membrane is in a state of high and stable hydration, sufficient for good proton conductivity.
- *No water crossover:* The model assumes no net transport of water across the membrane (neither electro-osmotic drag nor back-diffusion).
- *Complete product water removal:* All water produced by the cathode reaction is assumed to be in the vapour phase and exits with the cathode outlet stream.

Electrochemical and reaction assumptions

These assumptions concern the core reactions and material properties at the cell level.

1. **Ideal anode feed:** The hydrogen feed stream is assumed to be 100% pure H_2. The model does not account for the potential negative impact of impurities (e.g., CO, CO_2) from a reformer, which would poison the anode catalyst in a real low-temperature PEMFC.
2. **Perfect reactant distribution:** Reactants are assumed to be perfectly and uniformly distributed across the entire active area of each cell. This eliminates local variations in concentration or current density.
3. **Complete and instantaneous reactions:** The electrochemical reactions (H_2 oxidation and O_2 reduction) are assumed to occur instantaneously to the extent dictated by Faraday's Law for the specified current. Kinetic limitations are captured solely within the activation overpotential term.
4. **Constant electrochemical parameters:** The semi-empirical coefficients from the Corrêa et al. [12] model ($\xi_1, \xi_3, \xi_4, B, J_{\max}, R_c$) are treated as constant values for the given stack design. (Note: ξ_2 is calculated dynamically based on local conditions, which is a refinement).

These assumptions are standard for developing a system-level, steady-state PEMFC model for process simulation and are critical for defining the scope and limitations of the subsequent analysis.

5.2 Membrane reactor design assumptions (Conf. A)

System-level operational framework

These assumptions define the overall state and boundaries of the membrane reformer.

1. **Steady-state operation:** The model calculates the performance of the membrane reactor at a single, constant operating point. It determines the final outlet conditions and internal profiles for a given set of feed conditions and design parameters. Transient effects such as start-up, shut-down, or dynamic load changes on the reformer itself are not considered in this steady-state model.
2. **Coaxial tube geometry:** The reactor is modelled as a shell-and-tube unit containing multiple identical coaxial membrane tubes operating in parallel. Each coaxial tube consists of an outer structural tube, an inner membrane tube, and a catalyst bed packed in the annulus between them. See subsection 6.2 for a deeper analysis.
3. **Co-current flow:** The process fluid (retentate) and the heating utility fluid are assumed to flow in the same direction (co-currently) from the inlet ($Z = 0$) to the outlet ($Z = L$) of the reactor tubes.

Fluid and Transport Properties

These assumptions govern the behaviour of gases and the transport phenomena within the reactor model.

1. **Ideal gas behaviour:** The retentate, permeate, and utility gas mixtures are assumed to behave as ideal gases. This is a valid assumption for the high temperatures and moderate pressures (e.g., up to 20 bar) typical for methanol steam reforming, where intermolecular forces are negligible. Partial pressures are determined using the ideal gas law ($P_i = Y_i \cdot P_{\text{total}}$).
2. **Plug flow reactor (PFR) assumption:** The model assumes ideal plug flow within the annular catalyst bed. This implies no radial gradients in concentration, temperature, or velocity, and no axial dispersion or back-mixing. All fluid elements are assumed to have the same residence time.
3. **Simplified fluid properties:** To maintain computational tractability within the custom Fortran model:

- **Temperature-dependent heat capacity:** Mixture heat capacities ($c_{p,\text{mix}}$) are calculated dynamically at each point along the reactor length. This is done by using a mole-fraction weighted average of the pure component heat capacities, which are themselves calculated as a function of temperature using the Shomate equation with hardcoded NIST parameters.
- **Constant viscosity:** The viscosity of the gas mixture is calculated using a mole-fraction weighted average of constant, pure-component viscosity values. These constants represent average values over the expected operating temperature range.
- **Ideal gas density:** The density of the gas mixture is calculated at each point using the ideal gas law and the dynamically calculated average molecular weight of the local mixture.

Reaction and permeation assumptions

These assumptions concern the core chemical and physical processes occurring within the reactor tubes.

1. **Peppley kinetics:** The rates of the three primary reactions (Methanol Steam Reforming, Methanol Decomposition, and Water-Gas Shift) are calculated using the comprehensive Langmuir-Hinshelwood kinetic model developed by Peppley et al. (1999) for $Cu/ZnO/Al_2O_3$ catalysts.
2. **Sivert's law for permeation:** Hydrogen permeation through the membrane is modelled using Sieverts' Law, where the flux is proportional to the difference in the square root of the hydrogen partial pressures across the membrane.
   - **Perfect H_2 selectivity:** The membrane is assumed to be perfectly selective to hydrogen. Only H_2 is allowed to permeate; all other components are fully retained in the process stream.
   - **Isothermal permeation:** The permeating hydrogen is assumed to exit the retentate phase and enter the permeate phase at the same temperature as the local retentate stream. Heat transfer through the membrane is considered negligible compared to other heat effects.
3. **Explicit energy balance:** The model solves a differential energy balance along the reactor length that explicitly accounts for:
   (a) The heat consumed/generated by the three chemical reactions (using specified heats of reaction).
   (b) The sensible heat removed from the retentate stream by the permeated hydrogen.
   (c) The heat transferred from the co-currently flowing utility fluid.
4. **Ergun equation for pressure drop:** The pressure drop through the annular packed catalyst bed is calculated at each integration step using the Ergun equation:

$$-\frac{dP}{dZ} = \frac{150\mu(1-\varepsilon)^2}{d_p^2\varepsilon^3}v_s + \frac{1.75\rho(1-\varepsilon)}{d_p\varepsilon^3}v_s^2 \tag{3.12}$$

   where ε is the bed voidage, d_p is the catalyst particle diameter, μ is the fluid viscosity, ρ is the fluid density, and v_s is the superficial fluid velocity.

5.3 Packed-bed reactor + separate membrane design assumptions (Conf. B)

Conventional packed-bed reactor (PBR) assumptions

These assumptions define the reformer, which is modelled as a non-isothermal, non-isobaric packed-bed reactor using the Aspen Plus R-plug block.

1. **Steady-state operation:** The reactor is modelled at a steady operating point, determining the final outlet conditions and internal profiles for a given set of feed conditions and design parameters.
2. **Plug flow reactor (PFR) Model:** The Aspen Plus R-plug model is used, which assumes ideal plug flow. This implies no radial gradients in concentration, temperature, or velocity, and no axial dispersion.
3. **Peppley kinetics:** The rates of the three primary reactions (Methanol Steam Reforming, Methanol Decomposition, and Water-Gas Shift) are calculated within a custom Fortran User kinetics subroutine based on the Langmuir-Hinshelwood model by Peppley et al. [54].
4. **Aspen-calculated energy balance:** The R-plug block solves the differential energy balance along the reactor length, accounting for the heat consumed/generated by the reactions and heat transfer with the specified utility.

5. **Aspen-calculated pressure drop:** The pressure drop through the packed catalyst bed is calculated by the R-plug block's built-in Ergun equation functionality, based on user-specified bed voidage and particle diameter.

Separate membrane unit assumptions

The hydrogen purification stage is modelled as a 0-D (lumped) separator using a custom User2 Fortran subroutine, which calculates the split between the permeate and retentate streams.

1. **Isothermal operation:** The separation process is assumed to be isothermal. The calculated permeate and retentate outlet streams are set to the same temperature as the reformate feed stream entering the unit.
2. **Isobaric retentate:** The pressure drop on the retentate (feed) side of the membrane module is assumed to be negligible; the retentate outlet pressure is set equal to the feed inlet pressure. The permeate outlet pressure is a specified input parameter.
3. **Sieverts' law with log-mean pressure difference:** Hydrogen permeation is modelled using Sieverts' Law. To accurately account for the changing H_2 partial pressure on the retentate side from inlet to outlet, an iterative log-mean pressure difference is calculated within the subroutine to determine the total H_2 flux for the given membrane area.
4. **Perfect H_2 selectivity:** The membrane is assumed to be perfectly selective to hydrogen. Only H_2 is allowed to permeate; all other components (CH_3OH, H_2O, CO_2, CO, etc.) are fully retained and exit in the retentate stream.

6 Components sizing and design constraints

This section aims to define the hardware of the process: the size of the components. The basis of the design of the process has been defined in section 2, as a result the power demand to be satisfied is 325 kW. In both configurations A and B the PEMFC system is modelled the same way. In fact, the comparison of the configurations is related to the reactor + separation unit. Therefore the fuel cell will be sized once for both configurations.

6.1 PEMFC sizing strategy

The sizing of the PEMFC stack was based on a set of performance targets derived from the application's power demand and typical benchmarks for efficient and durable marine fuel cell systems. The primary design targets were:

- **Net electrical power output:** $P_{\text{stack}} \geq 325$ kW
- **High hydrogen utilization:** $\mu_f \geq 95\%$
- **High electrical efficiency:** $\eta_{\text{HHV}} \geq 50\%$

The sizing process was performed iteratively to find a combination of operating current density (J), active area per cell (A_{MEA}), and number of cells (N_{cells}) that could meet the power target while maximizing the cell voltage (V_{cell}) and, consequently, the overall efficiency. The governing equations for power, current, efficiency and fuel consumption are:

$$P_{\text{stack}} = N_{\text{cells}} \cdot V_{\text{cell}} \cdot (J \cdot A_{\text{MEA}}) \tag{3.13}$$

$$\dot{n}_{\text{H}_2,\text{cons}} = \frac{I_{\text{stack}}}{2F} = \frac{N_{\text{cells}} \cdot J \cdot A_{\text{MEA}}}{2F} \tag{3.14}$$

$$\eta_{\text{HHV}} = \frac{V_{\text{cell}}}{HHV_{\text{volt}}} = \frac{V_{\text{cell}}}{1.48} \tag{3.15}$$

$$\mu_f = \frac{\dot{n}_{\text{H}_2,\text{cons}}}{\dot{n}_{\text{H}_2,\text{fed}}} \tag{3.16}$$

where I_{stack} is the total stack current (A), F is Faraday's constant 96485 C/mol, $\dot{n}_{\text{H}_2,\text{cons}}$ is the molar consumption rate of hydrogen (mol/s), η_{HHV} is the electrical efficiency and $\dot{n}_{\text{H}_2,\text{fed}}$ is the molar feed rate of hydrogen (mol/s).

The iterative design process revealed that operating at a low current density significantly increases V_{cell} and η_{HHV} but requires a larger total active area to achieve the target power. A final operating point of $J = 0.3 A/cm^2$ was selected as a favourable compromise. To meet the 325 kW power demand at the high cell voltage predicted by the model at this current density, a stack composed of 1200 cells, each with a large active area of 1200 cm^2, was determined to be necessary. This configuration is representative of modern stacks designed for high-power, high-efficiency applications.

6.2 Configuration A: membrane reactor sizing

Configuration A corresponds to the membrane reactor, in which the reaction and H_2 separation occur simultaneously. A detailed overview of the reactor geometry is presented below, followed by the sizing strategy for this equipment.

Membrane reactor geometry and design parameters

The reactor consists of a shell that encloses a bundle of identical coaxial membrane tubes operating in parallel. This arrangement, shown schematically in Figure 3.6a and in Figure 3.6b, enables three functions to occur simultaneously: methanol steam reforming in the catalyst bed, selective hydrogen separation through the membrane, and heat supply from an external utility stream. Each tube is composed of an outer structural wall, a catalyst bed in the annular gap, and an inner palladium-based membrane with a central channel (lumen) that collects the permeated hydrogen. The outer tube is in direct contact with the hot flue gas circulating in the shell, which delivers the energy required for the endothermic reforming reaction. Inside the annulus, the $Cu/ZnO/Al_2O_3$ catalyst promotes the conversion of the methanol/steam feed. The hydrogen formed in this region diffuses across the dense Pd layer of the inner tube and enters the lumen, where it is withdrawn as purified product. In the lumen a sweep gas is typically used to extract the H_2. The function of this gas is to force the flow of H_2 towards the exit of the pipes, thus not relying on natural convection for the flow circulation inside the pipes. This model does not take the sweep gas into account in the calculations, however it is important to be aware that in real life application it will most likely be present.

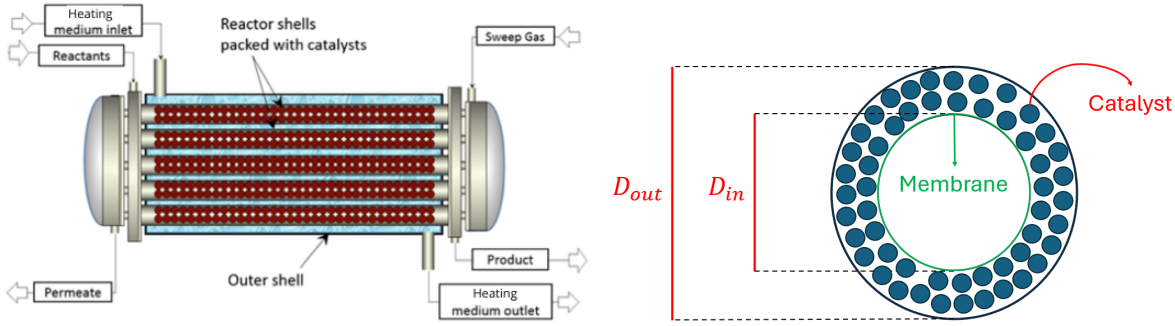

(a) Membrane reactor scheme [58]. Reprinted with permission.

(b) Tube cross-section.

Figure 3.6: Membrane reactor geometry.

To capture the essential physics, the model defines two key diameters: the inner membrane diameter (D_{in}), which determines the available surface area for hydrogen permeation, and the outer tube diameter (D_{out}), which governs the heat transfer area on the shell side.

Table 3.5 provides the list of fixed design parameters of the reactor. This group of parameters are taken from literature.

Membrane reactor sizing strategy

The design and operating parameters of the User2 membrane reactor model were iteratively adjusted to meet a set of stringent performance targets, ensuring the unit not only operates efficiently but also satisfies the downstream requirements of the PEM fuel cell. The primary design objectives for the membrane reformer are defined as follows:

Table 3.5: Fixed design parameters used in the membrane reactor model.

Parameter	Value
Catalyst bulk density (ρ_{cat})	1300 kg/m^3 [18]
Membrane permeance (p_{memb})	0.0005 mol/(s $\cdot$ m^2 $\cdot$ Pa$^{0.5}$) [59]
Surface area of fresh catalyst (S_A)	15,000 m^2/kg [54]
Shell/tubes heat transfer coeff. (U)	50 W/(m^2 $\cdot$ K) [60]
Steam to carbon ratio (S/C)	1.5 [18]
Permeate pressure (P_{perm})	10^5 Pa [59]
Void fraction (Φ)	0.37 [18]
Inlet process stream temperature (T_{in})	280°C [6]
Inlet utility stream temperature ($T_{util,in}$)	400°C [18]

1. **High methanol conversion:** The conversion of methanol in the retentate stream must exceed 95% to ensure efficient fuel utilization and minimize the amount of unreacted methanol sent to the downstream burner.
2. **High hydrogen recovery:** The hydrogen recovery, defined as the ratio of H_2 molar flow in the permeate stream to the total H_2 produced by the reactions, must be greater than 95%. This target ensures effective separation and maximizes the delivery of purified hydrogen to the fuel cell.
3. **Sufficient hydrogen production:** The molar flow rate of hydrogen in the final permeate outlet stream must be greater than or equal to 8.0593 kmol/h. This value is the calculated minimum hydrogen feed rate required by the sized PEMFC stack to achieve its target power output while maintaining a fuel utilization of 95%.
4. **Temperature constraint:** To ensure the stability of the Cu/ZnO/Al_2O_3 catalyst and prevent thermal degradation or undesirable side reactions, the process temperature of the retentate stream ($T_{\text{retentate}}$) must remain below 300°C at all points along the entire reactor length.
5. **Catalyst volume constraint:** A critical physical constraint is that the geometric volume of the annular catalyst bed within the reactor tubes must be sufficient to contain the specified mass of catalyst. This is expressed as:
$$V_{\text{annulus}} \geq V_{\text{catalyst}} \tag{3.17}$$
where V_{annulus} is the geometric volume calculated from the tube diameters and length, and V_{catalyst} is the volume occupied by the catalyst, calculated from the specified catalyst mass (m_{cat}) and its bulk density (ρ_{cat}). This ensures the reactor design is physically feasible.
6. **Bed dimension constraint:** To ensure the validity of the packed-bed assumption and minimize wall effects that can lead to flow maldistribution (channelling), a constraint is imposed on the characteristic width of the annular catalyst bed relative to the catalyst particle diameter. The ratio of the annular gap width (l_a) to the particle diameter (D_p) must be sufficiently large. A common heuristic requires this ratio to be at least 10 [61]. This ensures that the flow characteristics within the annulus can be reasonably approximated by a packed bed model rather than being dominated by wall interactions. The constraint is expressed as:
$$l_a = \frac{D_{out} - D_{in}}{2} \tag{3.18}$$
$$\frac{l_a}{D_p} \geq 10 \tag{3.19}$$
where D_{out} and D_{in} are the outer and inner diameters of the catalyst annulus, respectively.

These targets create a constrained optimization problem, where parameters such as reactor dimensions, catalyst loading, membrane area, and operating conditions (feed flow rate, utility temperature, and pressure) are manipulated to find a feasible and high-performance design point.

Achieving the performance targets outlined in the previous section requires a careful selection of the reactor's geometric and operational parameters. A manual iterative procedure was employed within the Aspen Plus simulation environment to determine a feasible design point. The key manipulated variables in this sizing process were the reactor tube length (l_{tubes}), the number of tubes (n_{tubes}), the particle diameter

(D_p), the total catalyst mass (m_{cat}), the inlet feed molar flow rate ($\dot{n}_{in}$), the retentate process stream pressure ($P_{retenate}$) and the inner and outer tube diameters (D_{in}, D_{out}).

The procedure involved adjusting these variables and running the User2 model to observe the impact on the key performance indicators until all six design targets were simultaneously met. The following governing equations were central to this iterative sizing and physical validation process:

$$A_{memb} = \pi D_{in} l_{tubes} n_{tubes} \tag{3.20}$$

$$V_{annulus} = (\frac{\pi D_{out}^2}{4} - \frac{\pi D_{in}^2}{4}) l_{tubes} n_{tubes} \tag{3.21}$$

$$V_{cat} = \frac{m_{cat}}{\rho_{cat}} \tag{3.22}$$

For context within a complete shell-and-tube assembly, the overall shell diameter was estimated to provide a preliminary assessment of the reactor's footprint. Assuming a standard triangular tube pitch (P_t) of 1.25 times the outer tube diameter, the shell diameter (D_{shell}) can be estimated using the following correlations:

$$P_t = 1.25 D_{out} \tag{3.23}$$

$$D_{shell} = D_{out} (\frac{n_{tubes}}{k_1})^{\frac{1}{n_1}} \tag{3.24}$$

where k_1 and n_1 are constants dependent on the tube layout and number of passes. For the purpose of this process it is assumed that the pipes make one single pass in the shell. Therefore according to Sinnott and Towler [60] at Table 12.4: $k_1 = 0.391$ and $n_1 = 2.141$.

Finally Table 3.6 shows the results of the sizing iterative process. With these settings the reactor meets all the six constraints previously stated.

Table 3.6: Configuration A sizing results.

Parameter	**Value**	**Parameter**	**Value**
n_{tubes}	212	m_{cat}	390 kg
l_{tubes}	1.5 m	D_{p}	1 mm
A_{memb}	20 m^2	$V_{\text{cat}} = V_{\text{annulus}}$	0.3 m^3
D_{in}	2 cm	$\dot{n}_{\text{in}}$	7.14295 kmol/h
D_{out}	4 cm	$P_{\text{retentate}}$	20 bar
D_{shell}	75.7 cm	P_t	5 cm

6.3 Configuration B: packed bed reactor + separate membrane sizing

Geometry and design parameters

The conventional packed-bed reactor (PBR) in Configuration B is modelled as a standard multi-tubular shell-and-tube heat exchanger. The methanol and steam feed mixture flows through a bundle of parallel tubes that are packed with the $Cu/ZnO/Al_2O_3$ catalyst. Heat required for the endothermic reforming reactions is supplied by a hot utility fluid circulating on the shell side. This configuration is representative of common industrial reformers and its fundamental design principles were outlined in the preceding literature review (section 4 of Chapter 2).

Following the reactor, the hydrogen purification is performed in a separate membrane unit, also conceptualized as a shell-and-tube module. The hot, hydrogen-rich reformate gas from the packed-bed reactor outlet is directed into the tube side of this separator. Hydrogen selectively permeates through the walls of these membrane tubes into the shell side, from which it is collected as the purified product stream. The remaining un-permeated gas, or retentate, exits from the tube outlets. A deeper review is visible in section 4. The key fixed design parameters and operating conditions used as a baseline for the Configuration B simulation are summarized in Table 3.7.

Table 3.7: Fixed design parameters used in the Configuration B model.

Parameter	Value
Shell/Tubes heat transfer coeff. (U)	50 W/(m^{2}K) [60]
Steam to carbon ratio (S/C)	1.5 [18]
Membrane permeance (p_{memb})	0.0005 mol/(s $\cdot$ m^2 $\cdot$ Pa$^{0.5}$) [59]
Void fraction (ϕ)	0.37 [18]
Permeate pressure (P_{perm})	10^5 Pa [59]
Inlet process stream temperature (T_{in})	280 °C [6]
Inlet utility stream temperature ($T_{\text{util,in}}$)	400 °C [18]

Configuration B sizing strategy

The sizing of the conventional packed-bed reactor and the separate membrane unit in Configuration B was performed through a manual iterative procedure within the Aspen Plus environment. The goal was to find a feasible design point that satisfies the same primary performance targets defined for Configuration A (see subsection 6.2), namely: High Methanol Conversion (>95%), High Hydrogen Recovery (>95%), Sufficient Hydrogen Production (>8.0593 kmol/h), and a catalyst bed Temperature Constraint (<300°C).

Unlike the integrated User2 model for Configuration A where the reactor equations were solved explicitly in Fortran, the conventional reactor in this configuration is modelled using the built-in Aspen Plus R-plug block. This block internally solves the differential mass and energy balance equations using the reaction rates provided by the custom kinetics subroutine. Consequently, the sizing process involved manipulating the design parameters on the Aspen Plus forms and re-running the simulation to observe the impact on the performance targets, as direct control over the integration loop and internal profiles was handled by the simulator itself.

The key manipulated variables in this sizing process were the reactor tube length (l_{tubes}), the number of tubes (n_{tubes}), the total catalyst mass (m_{cat}), the inlet feed molar flow rate ($\dot{n}_{\text{in}}$), the inner tube diameter (D_{in}), the retentate process stream pressure ($P_{\text{retentate}}$) and the membrane area (A_{memb}). The following governing equations and constraints were central to this iterative sizing and physical validation process.

For the conventional packed-bed reactor, two key physical constraints were considered to ensure the model's validity. First, the total geometric volume of the reactor tubes must be sufficient to contain the specified mass of catalyst. This is expressed as:

$$V_{\text{tubes}} = \frac{\pi D_{in}^2}{4} \cdot l_{\text{tubes}} \cdot n_{\text{tubes}} \geq V_{\text{catalyst}} \tag{3.25}$$

where V_{catalyst} is the volume occupied by the catalyst, calculated from its mass (m_{cat}) and bulk density (ρ_{cat}).

Second, to ensure the validity of the plug-flow assumption and minimize non-ideal wall effects, a constraint was imposed on the ratio of the tube inner diameter (D_{in}) to the catalyst particle diameter (D_p). A common heuristic requires this ratio to be at least 10 [61].

$$\frac{D_{in}}{D_p} \geq 10 \tag{3.26}$$

The separate membrane unit was sized to achieve the target hydrogen recovery. The required membrane area was determined based on the hydrogen flow in the reformate stream and the permeation characteristics defined by Sieverts' Law. The total area is a function of the number of membrane tubes, their length, and their diameter:

$$A_{\text{memb}} = \pi \cdot n_{\text{tubes,memb}} \cdot l_{\text{tubes,memb}} \cdot D_{\text{memb}} \tag{3.27}$$

The sizing procedure involved adjusting these geometric parameters in the User2 model until the hydrogen recovery target was met for the given reformate feed from the reactor.

After numerous simulation runs, a converged design point that successfully met all performance targets was established. The key sizing parameters for this final design of the packed-bed reactor and separate membrane unit are presented in Table 3.8.

Table 3.8: Configuration B sizing results.

Parameter	Value	Parameter	Value
n_{tubes}	156	m_{cat}	380.2 kg
l_{tubes}	1.5 m	$P_{\text{retentate}}$	10 bar
D_{in}	4 cm	A_{memb}	10.5 m^2
D_{shell}	72.1 cm	D_{memb}	3 cm
P_t	5 cm	$l_{\text{tubes,memb}}$	1 m
D_p	4 mm	$n_{\text{tubes,memb}}$	112
V_{tubes}	0.294 m^3	$\dot{n}_{\text{in}}$	7.427 kmol/h

7 Heat integration strategy

A key objective of this thesis is to evaluate the overall system efficiency, which is heavily influenced by the effectiveness of thermal management. Onboard a ship, minimizing waste heat and reducing the reliance on external utilities for heating and cooling is paramount for achieving a compact, efficient, and cost-effective power system. Therefore, a comprehensive heat integration strategy was developed and modelled for both Configuration A (membrane reactor) and Configuration B (conventional packed-bed reactor + separator). This section outlines the principles and implementation of this strategy.

The approach is based on identifying the primary heat sources and sinks within the process and utilizing a network of heat exchangers to recover high-temperature waste heat to satisfy the system's heating demands.

7.1 Identification of heat sources and sinks

The main thermal streams available for integration were identified as follows:

1. Primary heat sources:
    - The hot flue gas stream exiting the burner, which combusts the unreacted retentate fuel. This is the highest quality heat source, with temperatures potentially exceeding 1200°C.
    - The exothermic PEM fuel cell stack, which generates a significant amount of low-grade waste heat (at 80°C), captured by the coolant loop.
    - Hot process streams that require cooling, such as the compressed hydrogen exiting the separation unit.
2. Primary heat sinks:
    - The highly endothermic methanol steam reforming reaction, requiring a constant high-temperature heat supply (modelled with a utility fluid loop).
    - The vaporization and preheating of the liquid methanol/water feed from ambient temperature to the reformer inlet temperature. This represents the largest single heating duty.
    - The preheating of the PEMFC air feed to the stack operating temperature (80°C).

7.2 Design of the heat exchanger network

Based on the identified sources and sinks, a heat exchanger network was designed and implemented in Aspen Plus. The strategy prioritizes using the highest temperature waste heat for the highest temperature duties, following thermodynamic principles.

Reactant preheating and vaporization

The largest single heating demand in the process is the vaporization of the liquid methanol-water mixture and its subsequent superheating to the required reformer inlet temperature. The highest quality heat source available for this duty is the hot flue gas produced by the combustion of the unreacted retentate fuel and extra methanol. A central heat exchanger is therefore modelled to transfer heat from the hot burner exhaust to the cold liquid reformer feed. The outlet temperature of this preheated feed stream is specified as a design target (280°C) to ensure proper conditions for the reforming reaction.

Reformer heating and retentate loop

The endothermic duty of the methanol steam reforming reaction requires a continuous, high-temperature heat supply. Since the hot thermal utility fluid leaving the evaporator of the feed has still some qualitative heat to provide, the same stream is sent directly as thermal fluid in the reformer itself.

The retentate stream leaving the reactor + separation unit contains mainly unseparated H_2, unreacted CH_3OH, CO and CO_2. Therefore this stream contains species that could be burned to provide extra heat. Consequentially, this stream is sent back to the burner where it is mixed with some extra methanol and air to provide the heat for the thermal utility stream used both in the evaporator and reformer. To clearly visualise the heat management see Figure 3.7 for Configuration A and Figure 3.8 for Configuration B.

PEMFC air feed preheating

The hot H_2 permeated stream coming from the reactor + separation unit must be cooled down to 80°C to meet the PEMFC temperature requirements. The air fed to the cathode of the PEM fuel cell is the ideal candidate to absorb this heat. In fact pre-heating the air going into the fuel cell increases the thermal efficiency of the electrochemical equipment. A dedicated heat exchanger is therefore modelled to transfer heat between this two streams.

PEMFC thermal management and waste heat recovery

The PEM Fuel Cell is modelled as an isothermal unit operating at a constant temperature. The significant waste heat generated by the stack's electrochemical inefficiencies must be continuously removed. This is modelled using a closed-loop liquid coolant system. A cold water stream enters the PEMFC User2 block, where it absorbs the heat produced by the component. The resulting coolant outlet temperature is calculated based on the coolant's flow rate and heat capacity, following the principle of $Q = \dot{m}C_p\Delta T$.

A final cooler is then used to reject any remaining excess heat to the environment, cooling the coolant back to its initial inlet temperature before it is pumped and recycled.

7.3 Burner design

As mentioned in the theoretical background and the identification of the heat exchanger network, a burner is used to provide the hot thermal fluid required for both the reformer and the feed evaporator. The feed to this burner consists of a slipstream of fresh methanol, compressed air, and the recycled retentate stream from the separation unit, which contains unreacted fuel species such as CH_3OH, H_2, and CO.

The operational strategy for the burner, as implemented in the model, is to use a highly lean fuel-air mixture. This involves supplying a large excess of air, which results in two key outcomes: (1) it produces the large mass flow rate of hot gas required to meet the significant heat duties of the evaporator and reformer, and (2) it yields moderate flue gas temperatures, calculated to be between 550°C and 900°C across the various operating points. The specific settings for the excess air and the resulting temperature profiles for each configuration will be presented and analysed in detail in the Results section.

It is crucial to contextualize these operating conditions within the principles of practical combustion. The burner is an auxiliary component in this study, and as such, a simplified thermodynamic model based on an energy balance was employed. While this model accurately calculates the resulting temperature from the energy release, it does not account for the chemical kinetics that govern flame stability. In a conventional flame burner, combustion is sustained by a high-temperature, self-propagating gas-phase reaction. This process has a well-established kinetic stability limit, typically around 900-1200°C, below which the chemical reactions become too slow to generate heat faster than it is dissipated, causing the flame to become unstable and extinguish (quench) [62]. Therefore, the lower end of the calculated temperature range in this study would be physically unachievable in a standard burner design.

To provide a physically sound basis for these model parameters, it is specified that the burner for this system is a catalytic burner. Unlike a conventional burner, a catalytic unit employs a solid catalyst (typically a noble metal on a ceramic monolith) to facilitate a flameless surface reaction. This technology fundamentally changes the combustion mechanism, enabling complete and stable oxidation of ultra-lean fuel mixtures at much lower temperatures, typically within the 500-1000°C range [63]. This operational window aligns perfectly with the calculated results of this study, validating the chosen process conditions for process heating applications [64]. Furthermore, the presence of hydrogen (H_2) in the recycled retentate stream, known for its high reactivity and wide flammability limits, acts as a combustion promoter that would further enhance the stability and efficiency of the catalytic process. This low-temperature, flameless

approach also carries significant practical advantages, including the near-complete elimination of thermal NOx formation and the ability to use conventional steel alloys for construction, aligning with the overall goal of an efficient and cost-effective system.

8 ASPEN Plus block flow diagrams

The first outputs of the models are the process flow diagrams. Figure 3.7 and Figure 3.8 present the complete ASPEN Plus models for Configuration A and Configuration B, respectively. These figures highlight the different approaches used for H_2 purification in each configuration. They also include the full heat integration network, as described in section 7.

Each stream in the diagrams is annotated with its temperature (°C), pressure (bar), molar flow rate (kmol/h), and mass flow rate (kg/h). Similarly, each process block indicates either the power (W) required/produced or the heat duty (W) supplied/removed.

It is noticeable that in both ASPEN Plus block flow diagrams several heaters that have not been discussed in section 7 are present. More specifically block `B1`, `B2` and `B3` for Configuration A and block `H-RETE` and `H-H2FEED` for Configuration B. These blocks are a workaround for a problem encountered in the output streams of a User2 block. In short the output streams of a User2 block are missing the thermodynamic property, they only contain temperature, pressure, and the flow rate of each component. Therefore, the added heaters simply perform a flash calculation without altering any property of the stream. This allows to obtain the thermodynamic property missing. These streams are then complete and can be used for all the calculations necessary.

9 Model control strategy

This section aims to bridge the methodology chapter with the results and discussion chapter. In fact, to understand deeply the results and the analysis it is compulsory to know how the results have been extracted. Therefore this section will highlight how the entire model is controlled in order to obtain high quality consistent results.

Five main controllers are used as knob in both configurations. First, as explained in the section of heat integration, the PEMFC need to dissipate the heat that the electrochemical reaction creates. The PEMFC it is designed to be operating constantly and evenly at 80°C. To achieve this state the first controller iterates over the molar flow rate of the water cooling loop in order to remove all the heat produced. Therefore the coolant fluid is designed to leave the fuel cell at around 78°C.

Second, to ensure that the PEMFC receives enough H_2 from the permeated stream to meet the power demand, a controller iterates over the molar flow rate of the reformer feed. In this way it is granted that the reactor produces enough moles of H_2 to meet the PEMFC requirements. As a result, this controller indirectly keeps the PEMFC fuel utilization constant to a desired value, in our case it was set to be 97%.

The third controller is again applied to the PEMFC component. As explained in the literature review chapter the PEMFC typically works with an O_2 excess of 100%. This means that the amount of O_2 that needs to be supplied to the fuel cell is double the amount of the stoichiometric requirement. To ensure that this constraint is met the third controller iterates over the molar flow rate of the air fed to the fuel cell until the correct amount of O_2 is supplied.

The fourth controller is in charge of iterating the molar flow rate of the air fed to the burner. In fact, the system performances are strongly influenced by the O_2 excess quantity that is fed to the burner. In fact, similarly to the PEMFC, also the burner typically works with some O_2 excess to respect to the stoichiometry ratio. This controller it is not set to a singular value of O_2 excess but each configuration at each different operating condition will have its own design point. This will be further explained in the results and discussion chapter.

Lastly, to assure that the reactor process stream operates within the correct range of temperatures, the inlet thermal fluid temperature of the reformer is controlled. In fact, as shown in Figure 2.10 the process stream is expected to work in its optimum range within 220°C and 300°C when the steam to carbon ratio is 1.5. To achieve this constraint the controlled thermal fluid temperature it is set to be constantly at 400°C. The fifth controller iterates over the mass flow rate of the extra methanol fed to the burner until it matches the desired temperature setting.

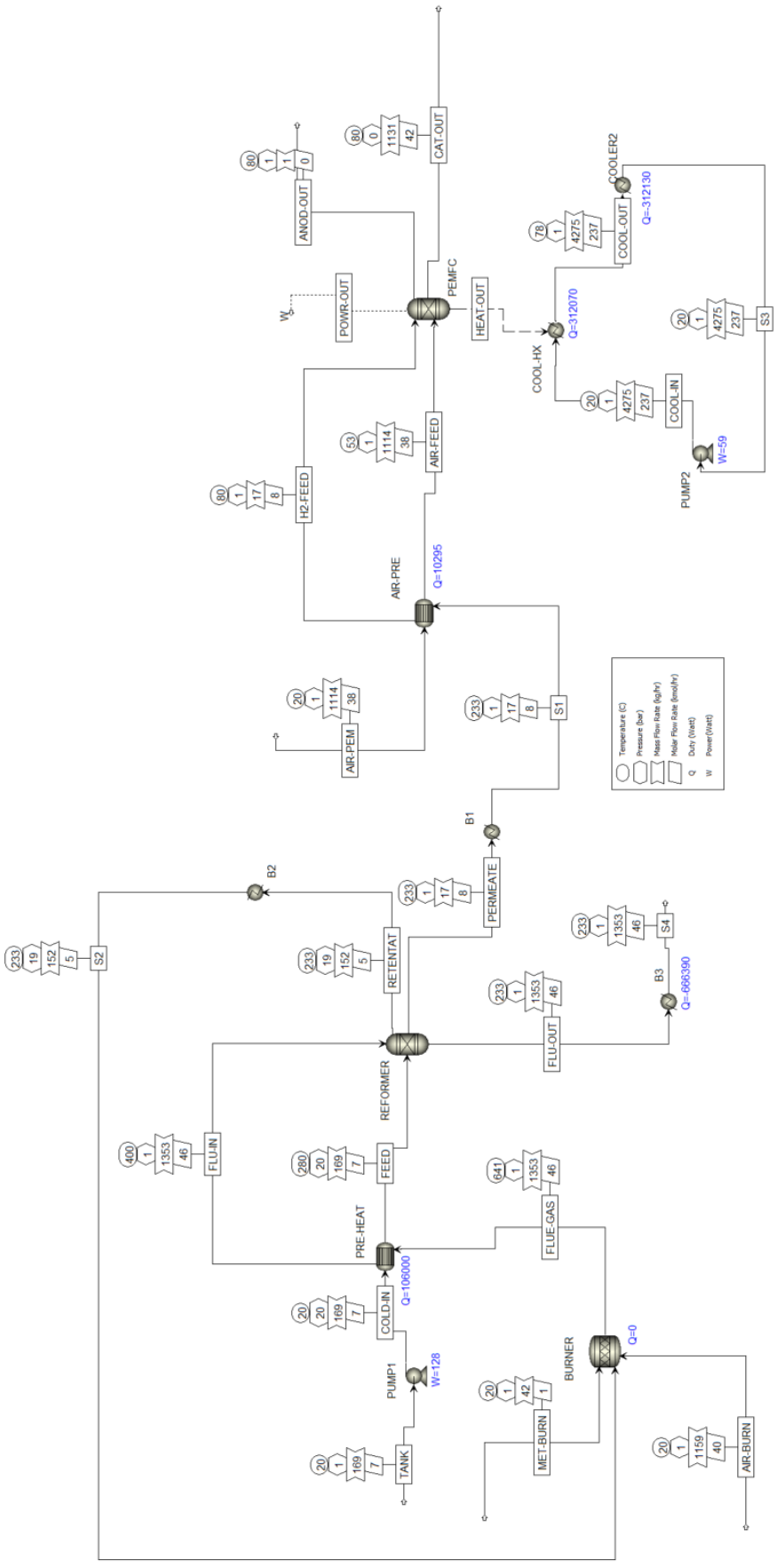

Figure 3.7: ASPEN Plus block flow diagram Configuration A.

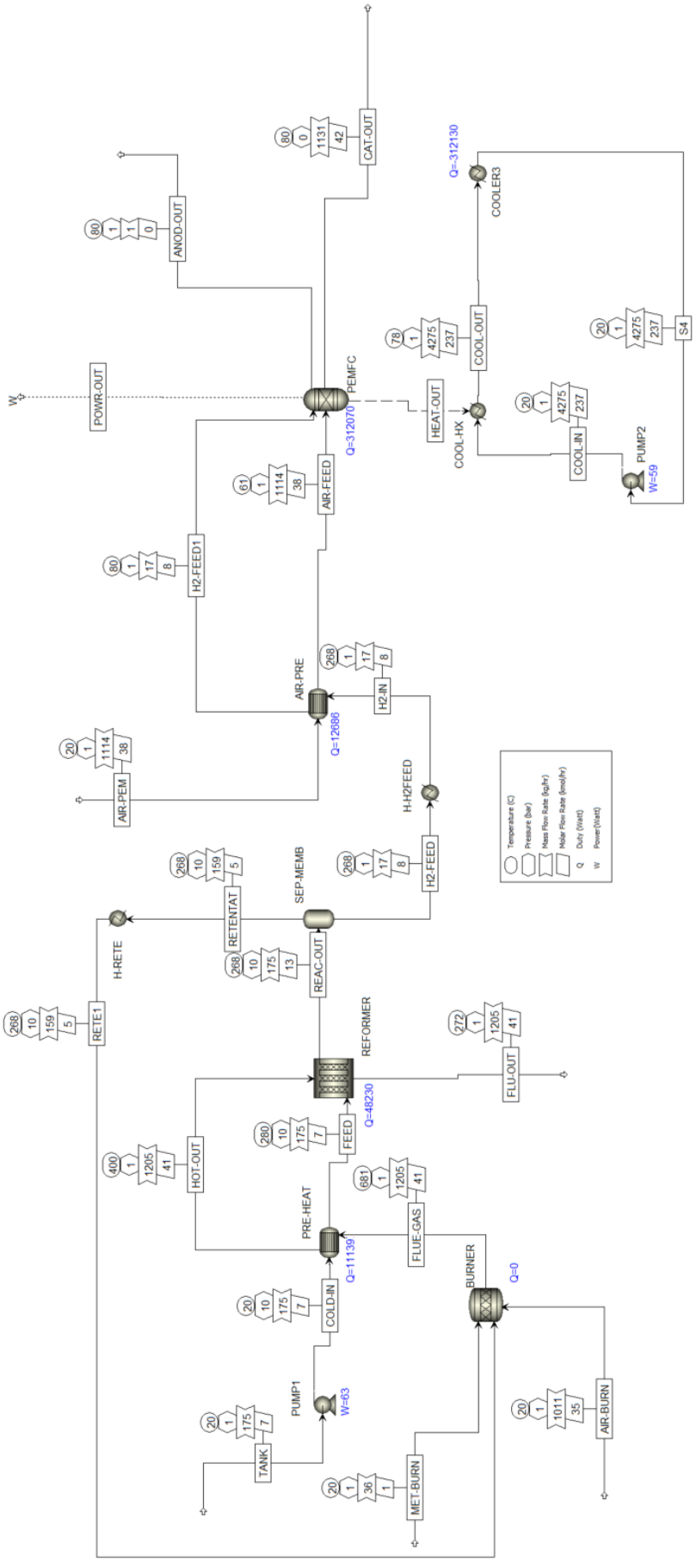

Figure 3.8: ASPEN Plus block flow diagram Configuration B.

The combination of these five controllers restricts the freedom of the models. This allows the process to work always within the correct boundaries.

Similarly to the sizing, to achieve consistent results the simulations need to satisfy performance constraints. The following list forms the basis for the simulations results. It is important to keep in mind that these constraints are met for both configurations only at the design operating condition. This means that the sensitivity analysis, where power load demand is varied, will show how the system reacts under off-design operating conditions.

- **Net electrical power output:** $P_{\text{net}} \geq 325$ kW which means $J = 0.3A/cm^2$
- **High PEMFC hydrogen utilization:** $\mu_f \geq 95\%$
- **High PEMFC electrical efficiency:** $\eta_{\text{HHV}} \geq 50\%$
- **Constant O_2 excess in the PEMFC:** $O_{2,excess,PEMFC} = 100\%$
- **High methanol conversion:** $X_{\text{CH}_3\text{OH}} \geq 95\%$
- **High H_2 recovery:** $\text{Rec}_{\text{H}_2} \geq 95\%$
- **Fixed & constant T utility in the reformer:** $T_{utility,in} = 400°\text{C}$

10 Key Performance Indicators (KPIs)

To quantify and compare the performance of the two systems, a set of Key Performance Indicators (KPIs) was defined. These metrics evaluate the efficiency of the overall system, the performance of the core reforming and separation subsystems, and the environmental impact.

Overall system performance

1. **Overall system efficiency (η_{sys}):** This is the primary metric for overall performance, defined as the net electrical power output divided by the total chemical energy input from the consumed methanol fuel, based on its Lower Heating Value (LHV).

$$\eta_{\text{sys}} = \frac{P_{\text{PEMFC,gross}} - P_{\text{parasitic}}}{(\dot{n}_{\text{CH}_3\text{OH, feed}} + \dot{n}_{\text{CH}_3\text{OH, burner}}) \cdot \text{LHV}_{\text{CH}_3\text{OH}}} \tag{3.28}$$

2. **Specific methanol consumption (SMC):** This KPI directly relates to the fuel operating cost and is defined as the total mass of methanol consumed per unit of net electrical energy produced.

$$\text{SMC}\left[\frac{\text{kg}}{\text{kWh}}\right] = \frac{\dot{m}_{\text{CH}_3\text{OH, feed}} + \dot{m}_{\text{CH}_3\text{OH, burner}}}{P_{\text{net,electric}}} \tag{3.29}$$

Reformer and separation performance

3. **Methanol conversion ($X_{\text{CH}_3\text{OH}}$):** This measures the effectiveness of the reforming stage by quantifying the fraction of methanol fed to the reformer that is converted.

$$X_{\text{CH}_3\text{OH}} = \frac{\dot{n}_{\text{CH}_3\text{OH, in}} - \dot{n}_{\text{CH}_3\text{OH, retentate}}}{\dot{n}_{\text{CH}_3\text{OH, in}}} \tag{3.30}$$

4. **Hydrogen recovery (Rec_{H_2}):** This measures the efficiency of the separation stage, defined as the fraction of hydrogen produced in the reformer that is recovered in the purified product stream.

$$\text{Rec}_{\text{H}_2} = \frac{\dot{n}_{\text{H}_2,\text{permeate}}}{\dot{n}_{\text{H}_2,\text{permeate}} + \dot{n}_{\text{H}_2,\text{retentate}}} \tag{3.31}$$

5. **Hydrogen yield (Y_{H_2}):** This combined metric evaluates the overall effectiveness of hydrogen production per unit of methanol fed to the reformer.

$$Y_{\text{H}_2}\left[\frac{\text{kmol H}_2}{\text{kmol CH}_3\text{OH}}\right] = \frac{\dot{n}_{\text{H}_2,\text{permeate}}}{\dot{n}_{\text{CH}_3\text{OH, in}}} \tag{3.32}$$

Environmental performance

6. **Specific CO_2 emissions:** This KPI quantifies the carbon footprint of the system, defined as the mass of carbon dioxide emitted from the burner flue gas per unit of net electrical energy produced.

$$\text{Specific } CO_2 \left[\frac{\text{kg } CO_2}{\text{kWh}}\right] = \frac{\dot{m}_{CO_2,\text{flue gas}}}{P_{\text{net,electric}}} \tag{3.33}$$

Chapter 4

Model validation

The objective of this chapter is to verify the accuracy and reliability of the models developed for the main process units. The validation covers the kinetic model of the packed-bed reactor, the electrochemical model of the PEM fuel cell and the kinetic model of the membrane reactor.

1 PEMFC model validation

To validate the custom User2 PEM fuel cell model, its steady-state performance was simulated and compared with the experimental data of a Ballard Mark V fuel cell stack reported by Corrêa et al. [12]. The simulation setup was configured to replicate precisely the experimental conditions and stack parameters described in the reference study. The key parameters, directly taken from Table I of Corrêa et al. [12], are summarized in Table 4.1.

Table 4.1: PEMFC parameters for model validation, adapted from Table I of Corrêa et al. [12].

Parameter	**Value**	**Parameter**	**Value**
n_{cells}	1	ξ_1	-0.948
T_{op}	343 K	ξ_2	$0.00286 + 0.0002 \ln A + (4.3 \cdot 10^{-5}) \ln c_{H_2}$
A	50.6 cm^2	ξ_3	$7.6 \cdot 10^{-5}$
t_{memb}	178 μm	ξ_4	$-1.93 \cdot 10^{-4}$
B	0.016 V	λ	23
R_C	0.0003 Ω	$J_{\max}$	1.5 A/cm^2

Figure 4.1 presents the polarization, power density, and voltage efficiency curves obtained from the Aspen Plus User2 model developed in this work, compared with the experimental data of Corrêa et al. [12]. Simulations were performed at different operating pressures for both H_2 and O_2 (1 atm, 3 atm, and 5 atm). Although Corrêa et al. [12] report an operating pressure of 1 atm, they also reference the study by Mann et al. [65], which uses 3 atm and 5 atm. A closer inspection of Figure 4.1 shows that the higher the operating pressure the closer are the results compared to the model of Corrêa et al. [12]. This suggests that the actual operating pressure in their experiments may have been 3 atm or higher, consistent with Mann et al. [65].

Overall, the simulated polarization curve (Figure 4.1a) shows excellent agreement with the reference data across the entire operating range. The model correctly captures the initial steep voltage drop from activation losses due to reaction kinetics, the subsequent quasi-linear decrease from ohmic resistances, and the final sharp drop-off at high currents from concentration losses due to mass transport limitations. This confirms that the model accurately implements the fundamental electrochemical relations governing the Nernst potential and the three main overpotential contributions.

Furthermore, as expected, the model correctly reproduces the performance enhancement observed at higher operating pressures (3 atm and 5 atm) due to increased reactant partial pressures, which elevate the Nernst potential and mitigate activation losses. The close correspondence between simulated and experimental curves provides strong evidence for the physical consistency and predictive accuracy of the custom PEMFC User2 model developed in this study.

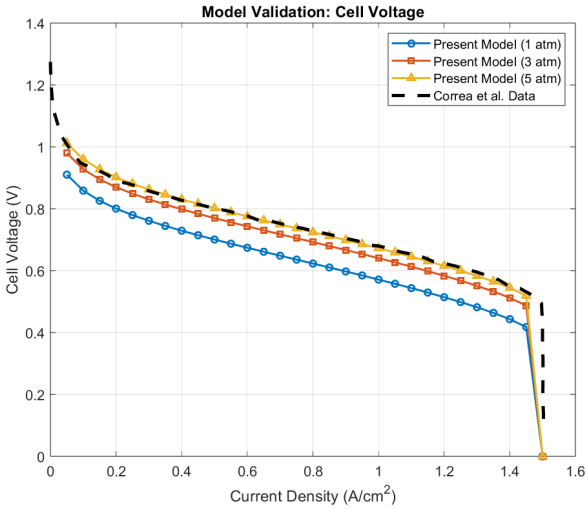

(a) Cell voltage.

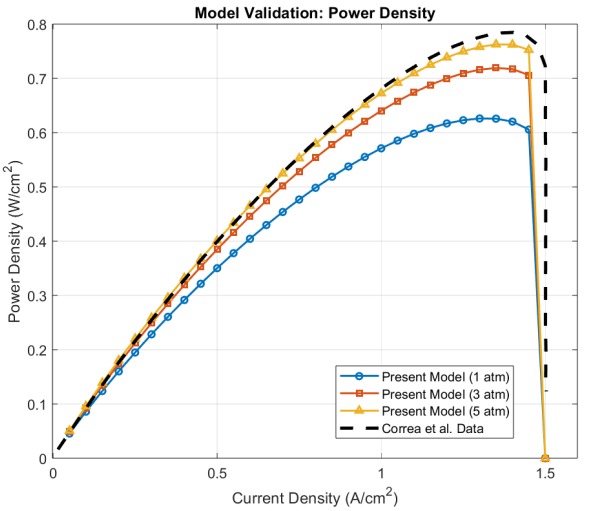

(b) Power density.

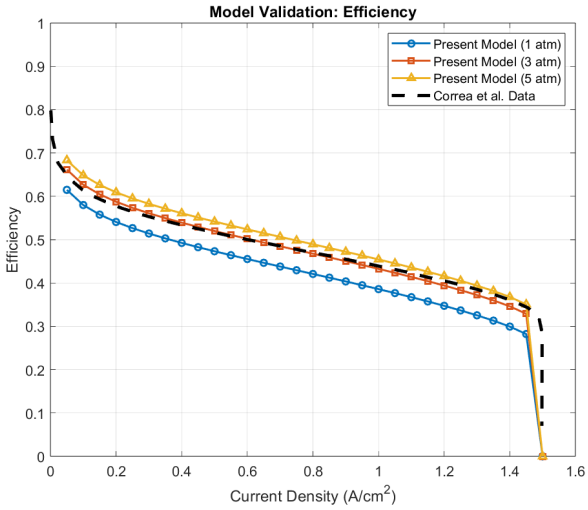

(c) Efficiency.

Figure 4.1: Comparison of PEMFC performance curves versus Corrêa et al. [12] for model validation: (a) Cell voltage, (b) Power density and (c) Efficiency.

2 Packed-bed reactor model validation (Configuration B)

The performance of the packed-bed reformer model was validated against the detailed modelling study of Zhu et al. [18], which employed the same kinetic model as Peppley et al. [54] in a comparable multi-tubular packed-bed configuration.

The simulation setup was designed to replicate precisely the operating conditions and parameters reported in the reference study. The corresponding model settings taken from Table 4 in the Zhu et al. [18] paper, are summarized in Table 4.2. The results of this validation are presented in Figure 4.2, where the calculated mole fraction profiles of the key species along the reactor length obtained from the present model (Figure 4.2a) are compared directly with those from Zhu et al. [18] (Figure 4.2b).

Table 4.2: Operating parameters for packed-bed reactor model validation, adopted from Table 4 of Zhu et al. [18].

Parameter	Value	Parameter	Value
D_{p}	1.5 mm	n_{tubes}	36
ρ_{cat}	1300 kg/m^3	D_{shell}	0.24 m
S_{A}	1.02×10^5 m^2/kg	l_{tubes}	0.48 m
ϕ	0.38	$P_{\mathrm{retentate}}$	1 bar
S/C	1.5	T_{in}	160 °C
D_{in}	0.016 m	$T_{\mathrm{util,in}}$	400 °C
$\dot{V}_{\mathrm{in}}$	4.5 L/h	$\dot{m}_{\mathrm{util,in}}$	6 g/s

The consumption of reactants (CH_3OH and H_2O) and the formation of products (H_2, CO_2, and CO) exhibit the expected trends, with reaction rates decreasing as the system approaches chemical equilibrium toward the reactor outlet. This behaviour aligns closely with the composition profiles reported by Zhu et al. [18] (Figure 4.2b). The strong qualitative and quantitative agreement between the present simulation and the reference data confirms the correct implementation and physical fidelity of the packed-bed reactor model.

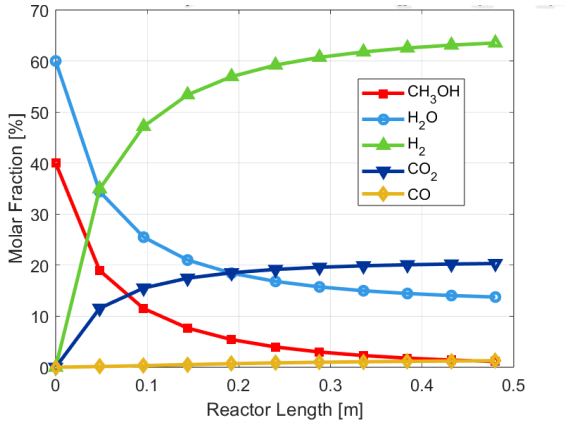

(a) Simulated mole fraction profiles for the packed-bed reactor under the reference conditions of Zhu et al. [18].

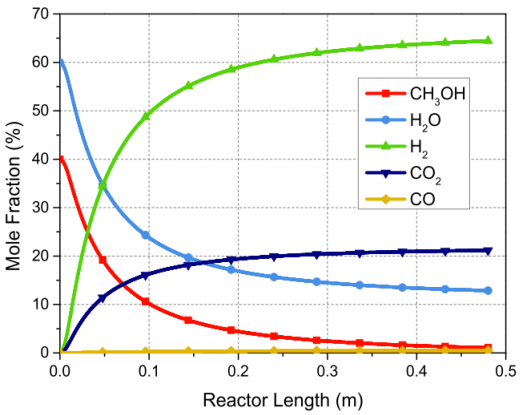

(b) Reference mole fraction profiles for the methanol steam reformer. Reprinted with permission from Zhu et al. [18].

Figure 4.2: Comparison of mole fraction profiles for packed-bed reactor model validation: (a) simulation results and (b) reference profiles from literature.

3 Membrane reactor model validation (Configuration A)

While the Zhu et al. [18] study provides validation for the base kinetics, it does not include a membrane. In literature it was not possible to find a membrane methanol steam reformer modelled using the Peppley et al. [54] kinetic model and the Sievert's law for the H_2 permeation. The validation of the custom User2 model for the membrane reactor is therefore based on its adherence to the expected physical phenomena characteristic of such systems.

Figure 4.3 shows the molar fraction profiles within the membrane reactor at the design operating point of this process. The profiles demonstrate the key feature of an integrated membrane reactor: the continuous in-situ removal of hydrogen. The concentration of H_2 in the retentate (green line) rises to a peak early in the reactor and is then actively suppressed as it permeates through the membrane. This suppression of the hydrogen product directly shifts the reaction equilibrium forward increasing the methanol conversion. The cumulative amount of permeated hydrogen (purple line) increases steadily along the reactor, representing the successful recovery of the purified product. This behaviour, particularly the suppression of the retentate H_2 concentration, is the hallmark of a functioning membrane reactor and qualitatively validates the coupled reaction-separation model.

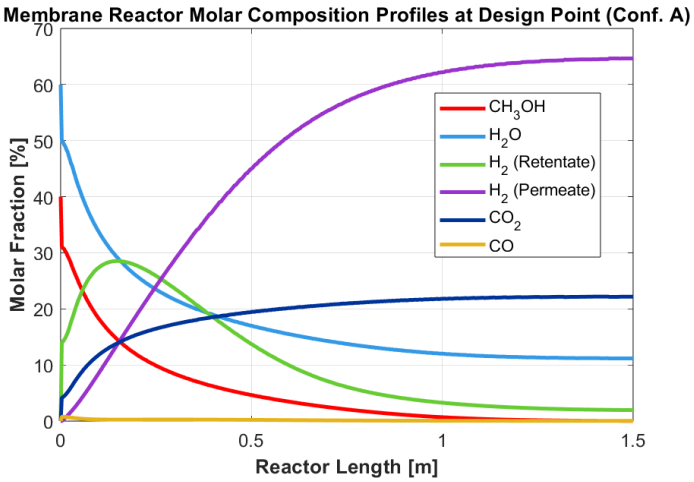

Figure 4.3: Calculated molar fraction profiles for key species in the Membrane Reactor (Configuration A) at the design point.

Chapter 5

Results and discussion

This chapter compares the two system configurations that were modelled, focusing on their performance and reliability. In addition, a sensitivity analysis is carried out for both configurations to validate the results under varying operating conditions.

1 Design point selection and burner performance

A critical aspect of both system configurations is the performance of the burner and its role within the heat integration network. The burner is responsible for generating the high-temperature flue gas required to preheat the reformer feed and supply the endothermic duty of the reforming reaction. To ensure complete combustion of the fuel the burner must be operated with excess air. However, the amount of excess oxygen is a sensitive parameter that directly impacts the overall system's thermal efficiency. To identify an optimal operating point for this subsystem, a sensitivity analysis was performed for both configurations at a constant design PEMFC load (J = 0.3 A/cm^2), varying the excess O_2 supplied to the burner.

The results of this analysis for Configuration A and B are presented in Figure 5.1 and Figure 5.2, respectively. It should be noted that in these dual-axis plots, the left (blue) and right (red) y-axes have independent scales. The intersection point of the two curves is therefore arbitrary and does not represent the chosen design point; rather, the optimal point is determined by analysing the trends of each curve against the common x-axis of O_2 excess.

For both configurations, it is observed that the methanol conversion within the reformer reaches after a certain level of O_2 excess it reaches a plateau. However, the overall system efficiency exhibits a distinct optimum. While initially increasing with O_2 excess (due to improved combustion), the efficiency begins to decline at higher excess levels.

This efficiency penalty is directly explained by the relationship between excess air, the resulting adiabatic flame temperature, and the supplementary fuel required to meet the system's heat demands. As shown in Figure 5.3 and Figure 5.4, increasing the excess air introduces a larger molar flow of inert nitrogen that must be heated to the flue gas temperature. This additional thermal mass causes the burner outlet temperature to decrease significantly. To compensate for this lower-temperature heat source and still meet the fixed heat integration targets (specifically, maintaining the reformer's utility fluid inlet at 400°C), the flow rate of supplementary methanol to the burner must be increased. This is clearly illustrated by the rising red curves in both figures. This additional fuel consumption represents a direct energy penalty and is the primary cause for the decline in overall system efficiency at high O_2 excess levels. Moreover, the bigger mass flow rate of the flue gas leaving the burner becomes a bigger reservoir of heat for the reformer, therefore keeping the reaction temperature higher and thus improving the conversion of methanol.

Based on this analysis, an optimal design point for the burner's air supply was chosen for each configuration. The goal was to select the lowest possible excess O_2 that still guaranteed maximum methanol conversion, thereby maximizing thermal efficiency by minimizing supplementary fuel consumption.

For Configuration A, as seen in Figure 5.1, methanol conversion reaches 99% at approximately 140% excess O_2 and the overall efficiency value it is slightly lower than its peak. This value was therefore selected as the chosen design point for all subsequent analyses of the membrane reactor system.

For Configuration B, the trade-off is slightly different. As shown in Figure 5.2, methanol conversion is only around 81% at the design point of configuration A (140% of O_2 excess). This setting does not meet the

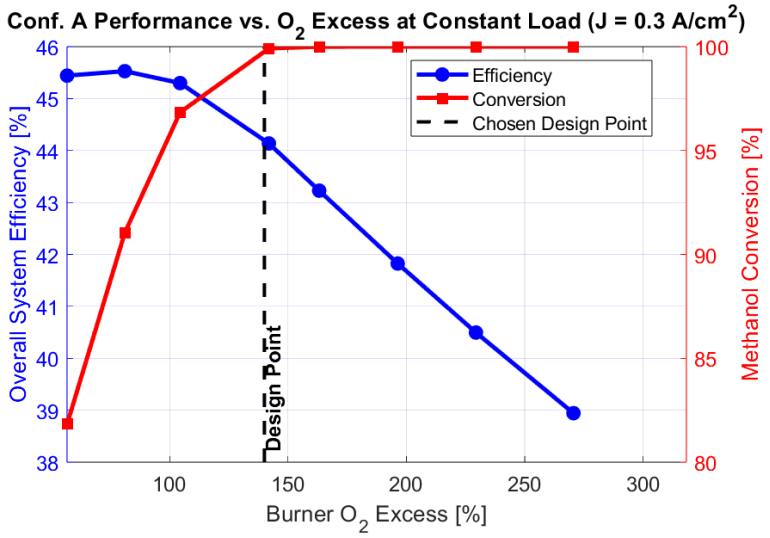

Figure 5.1: Configuration A performance vs burner O_2 excess at design load (J = 0.3 A/cm^2).

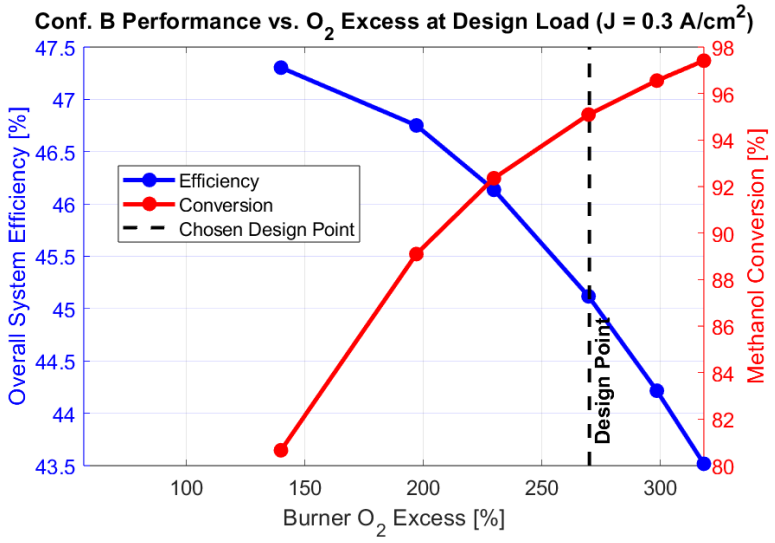

Figure 5.2: Configuration B performance vs burner O_2 excess at design load (J = 0.3 A/cm^2).

simulation constraint stated in Section 9 of the Chapter 3 therefore we are forced to increase the burner's O_2 excess until we meet 95% of methanol conversion regardless of the overall efficiency of the system. This constraint is satisfied at 270% of O_2 excess. Therefore, this setting is selected as design point for Configuration B.

This different design points in the two configurations is a direct reflection of the fundamental differences in the operational robustness and requirements of the two technologies. Furthermore, these respective design points are used for the performance comparisons across the full range of power loads presented in the following sections.

2 Comparative performance analysis across operating loads

Following the selection of the optimal burner operating points for each configuration, a comprehensive performance comparison was conducted across a range of net electrical power outputs, from lower loads (around 70 kW meaning J=0.05 A/cm^2) to the design operating condition (around 325 kW J=0.3 A/cm^2) and even to higher loads (around 380 kW meaning J=0.4 A/cm^2). This analysis evaluates the systems based on the key performance indicators defined in section 10 of the methodology, providing a clear comparison of the integrated Membrane Reactor (Configuration A) and the packed-bed reactor with separate separation (Configuration B).

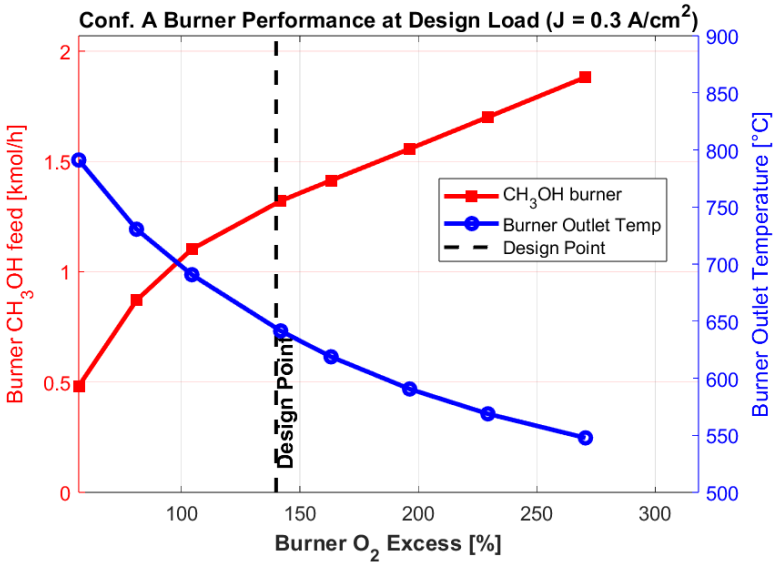

Figure 5.3: Burner performance of Configuration A vs O_2 excess at design load (J = 0.3 A/cm^2).

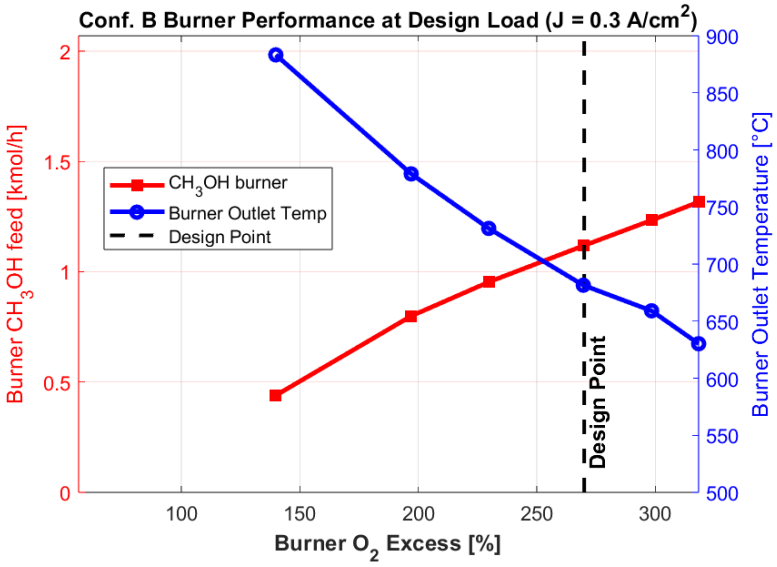

Figure 5.4: Burner performance of Configuration B vs O_2 excess at design load (J = 0.3 A/cm^2).

Overall efficiency, fuel consumption and emissions

The primary metrics for evaluating the two systems are the overall electrical efficiency, the specific methanol consumption, and the resulting environmental impact. Figure 5.5 presents the overall system efficiency for both configurations as a function of the net electrical power output. Counter-intuitively, the results indicate that Configuration B is more efficient than Configuration A across the entire operational range. The efficiency gap widens at higher power loads, where Configuration B achieves a peak efficiency of approximately 60%, while Configuration A peaks at 58% before declining more steeply. Both systems exhibit a decrease in efficiency at the highest power demands, which is attributable to the lower cell voltage of the PEMFC at high current densities, as established in the model validation (section 1).

To understand this unexpected result, it is essential to analyse the underlying reformer performance and the impact of the heat integration strategy. The superior efficiency of Configuration B is directly linked to its lower total fuel consumption. This is further detailed in Figure 5.6, which breaks down the Specific Methanol Consumption (SMC) into contributions from the reformer feed and the supplementary burner fuel.

The breakdown of SMC reveals a critical system-level trade-off. The dark-coloured bars, representing the methanol fed directly to the reformer, show that Configuration A (red bars) is slightly more fuel-efficient at the reactor level, requiring less methanol to produce the necessary hydrogen. This is a direct consequence

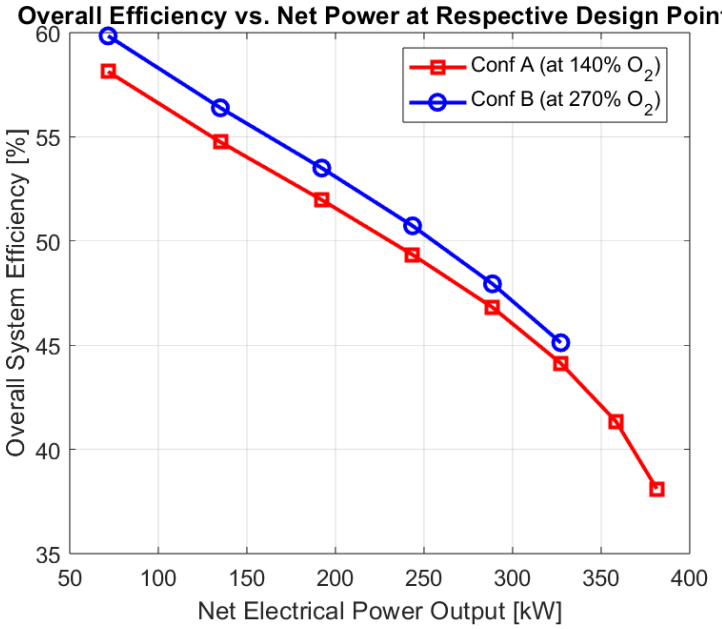

Figure 5.5: Overall system efficiency vs net power output for Configuration A and Configuration B.

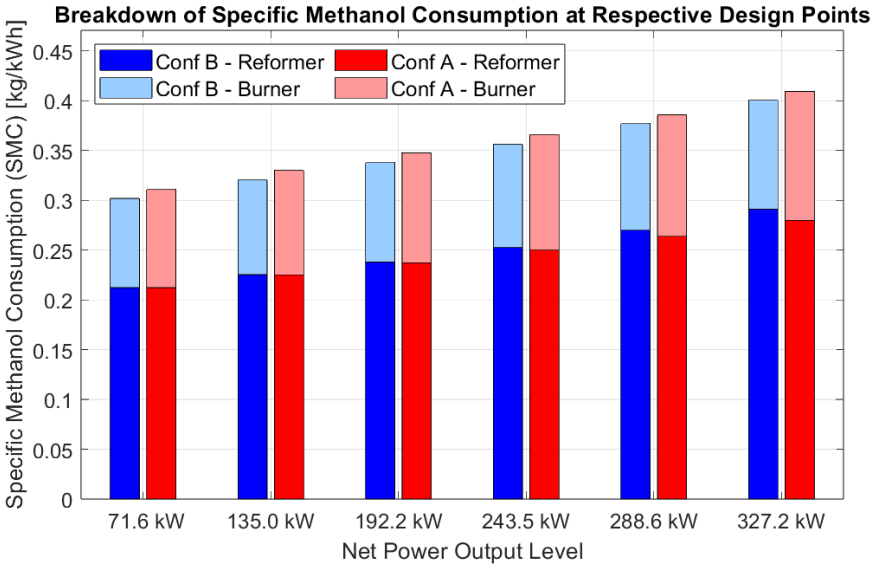

Figure 5.6: Breakdown of Specific Methanol Consumption (SMC) for the reformer feed and the supplementary burner fuel at various power levels.

of its superior methanol conversion. However, this advantage is completely negated by the demand for supplementary fuel in the burner, represented by the light-coloured bars. The retentate stream from the highly efficient membrane reactor is so depleted of combustible fuel (mainly unreacted CH_3OH) that it cannot provide sufficient heat for the endothermic reformer and feed preheating duties. Consequently, a large amount of fresh supplementary methanol must be burned, drastically increasing the total fuel consumption and lowering the overall system efficiency of Configuration A. In contrast, the less efficient conventional reactor in Configuration B produces a fuel-rich retentate (more unreacted CH_3OH), which allows its heat integration loop to be more efficient, requiring less supplementary fuel.

It can be argued that at the design point of 325 kW Configuration A was set to have 99% methanol conversion and Configuration B only 95% (see Figure 5.1 and Figure 5.2). This could lead Configuration A to a more depleted retentate stream by design conditions. However, the analysis is extended also to off design conditions where the design point doesn't directly influence the results. As shown in Figure 5.5 and Figure 5.6 the trend of Configuration B consuming less methanol still appears, leading to the same conclusions.

On the other hand, to fully interpret these results, it is important to note that the model does not account for the air blowers used in both the burner and the fuel cell. While the fuel cell performance is comparable for both configurations, the burner performance plays a crucial role in this analysis. As discussed in section 1, Configuration A operates with 140% excess O_2, whereas Configuration B operates with 270%. Consequently, Configuration B requires more blower power to handle the increased airflow. However, this additional auxiliary power, estimated between 200 W and 400 W, is negligible compared to the system's design power of 325 kW and therefore does not significantly affect the results.

Moving forward, the environmental impact follows the same trend as the fuel consumption. Figure 5.7 shows the specific CO_2 emissions for both systems. As emissions are directly proportional to the total amount of methanol combusted, Configuration B consistently demonstrates a lower carbon footprint per unit of energy produced, reinforcing the conclusion that its superior heat integration outweighs the lower conversion efficiency of its reformer from a system-level perspective.

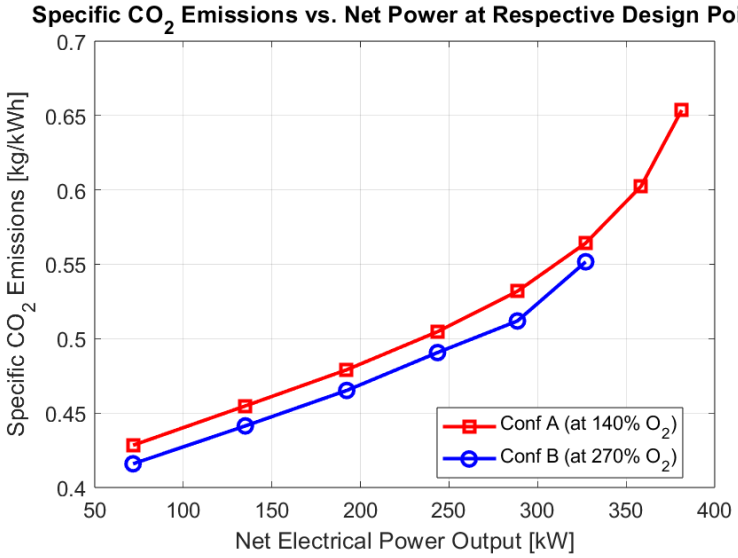

Figure 5.7: Specific CO_2 emissions vs net power output for both configurations.

Reformer conversion, H_2 yield and H_2 recovery

The performance of the reforming and separation subsystems explains the differences in reformer fuel consumption and overall system behaviour. Figure 5.8 directly compares the methanol conversion achieved in the reformers of both systems as a function of power load.

This result perfectly illustrates the fundamental advantage of the membrane reactor. Configuration A maintains a near-complete methanol conversion of almost 100% across a wide range of power outputs, only beginning to decline slightly above 350 kW. This is due to the continuous in-situ removal of hydrogen, which shifts the reaction equilibrium towards the products. In contrast, Configuration B shows a significant drop in conversion as the power load increases, falling from over 99.5% at low loads to approximately 95% at high loads due to equilibrium limitations at higher feed throughputs.

Figure 5.9 details the hydrogen recovery, which is the fraction of H_2 produced that is successfully separated. This parameter is specific for the H_2 separation and shows how the two different configuration behave based on how they are structurally modelled. Configuration A has the membrane separator directly implemented in the reactor. This means that while the reaction takes place and H_2 is produced it is also immediately separated from the reactant. This pushes the reaction forward as we have seen in the methanol conversion graph but this also translates into the impossibility of reaching 100% separation. In fact, at the end of the reactor even if the reaction rate is quite low the reaction is still happening. On the other hand, Configuration B has the membrane separator external to the reformer. This means that we can fully separate the H_2 from the process stream. Moreover, it is important to note that hydrogen recovery is a direct function of the membrane's design and operating conditions, primarily its surface area and the partial pressure difference across it. The results shown from the plot are therefore highly influenced by the membrane sizing. For instance, choosing an undersized membrane for Configuration B could have shown a H_2 recovery lower than 100%. In the same way over-sizing the membrane area of Configuration A could have led to a higher H_2 recovery. In conclusion, even if the two configurations are very different regarding the separation of H_2 both systems meet the separation requirements set in Section 9 of Chapter 3.

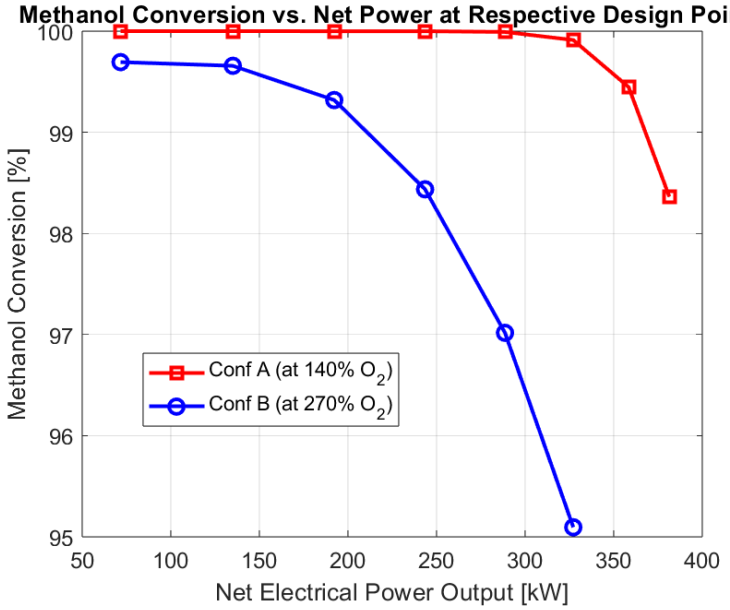

Figure 5.8: Methanol conversion in the reformer vs net power output for both configurations.

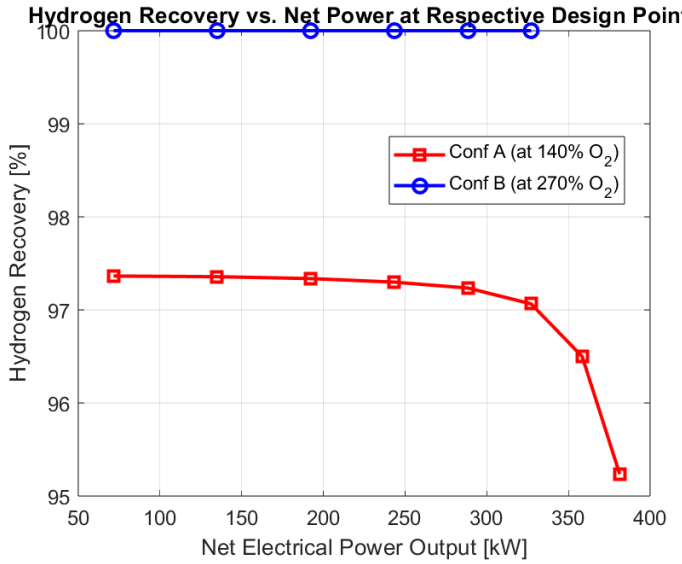

Figure 5.9: Hydrogen recovery of the separation stage vs net power output for both configurations.

Ultimately, the combination of conversion and recovery is captured by the hydrogen yield, presented in Figure 5.10. The hydrogen yield of Configuration A remains high across the load range, whereas the yield of Configuration B decreases in line with its falling methanol conversion. This analysis highlights the central conflict of the integrated membrane reactor design: while it is exceptionally effective at the unit-operation level for converting methanol and yielding a high amount of purified hydrogen, its very effectiveness creates a challenge for thermal self-sufficiency at the system level.

As shown in Figure 5.5, Figure 5.7, Figure 5.8, Figure 5.9, and Figure 5.10, the data points for Configuration B end at a lower power load than those for Configuration A. This occurs because the membrane in the separator unit acts as a bottleneck in the system.

As explained in the methodology, membrane permeation is proportional to both the membrane area and the pressure difference across the membrane. Although the sizing conditions selected for Configuration B enable the system to reach the target power of 325 kW, there is insufficient capacity to operate at higher power levels. At that point, the membrane becomes saturated, and the pressure difference is no longer sufficient to drive further H_2 permeation. Consequently, even if the reactor produces additional H_2, it remains in the process stream and exits in the retentate, rather than being separated. As a result, the PEMFC receives less fuel and cannot meet a higher power demand.

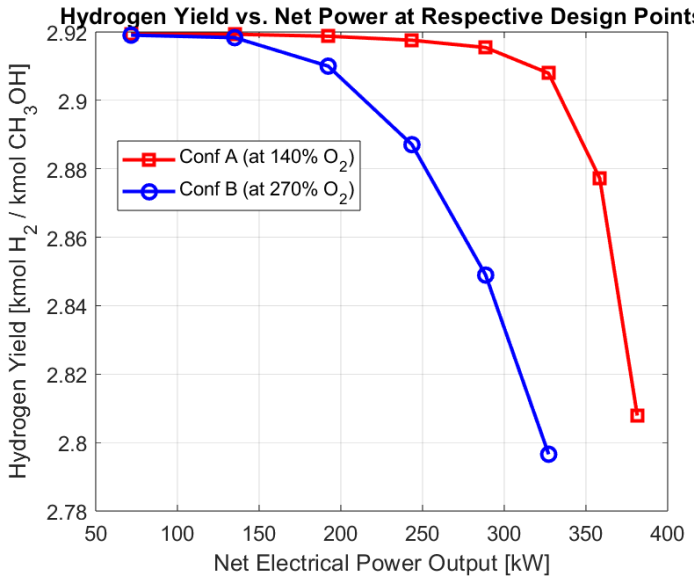

Figure 5.10: Overall hydrogen yield (kmol of purified H_2 per kmol of CH_3OH feed) vs net power output for both configurations.

This limitation arises from an overly tight sizing of the membrane separator unit. Increasing either the membrane area or the process stream pressure would enhance H_2 separation, but at the expense of higher pumping power or increased membrane cost. Conversely, the membrane in Configuration A appears to be oversized, allowing operation at higher power loads but also resulting in greater pumping power requirements and higher membrane costs.

3 Internal reactor profiles results and comparisons

To gain a deeper understanding of the phenomena driving the performance differences between the two configurations, the internal reactor profiles were analysed and compared at design point.

3.1 Composition profiles comparison

Figure 5.11 presents a comparative analysis of the molar composition profiles along the reactor length for the integrated membrane reactor (Configuration A) and the conventional packed-bed reactor (Configuration B). Both configurations exhibit the expected consumption of reactants (CH_3OH and H_2O) and formation of products (H_2, CO_2, and CO). However, the profiles reveal fundamental differences in reactor performance driven by the in-situ removal of hydrogen in Configuration A.

In the conventional packed-bed reactor (Figure 5.11b), the molar fraction of H_2 steadily increases along the reactor length, reaching its maximum value at the outlet as it approaches chemical equilibrium. Correspondingly, the conversion of methanol (red line) is significant initially but decelerates in the latter half of the reactor as the increasing H_2 partial pressure inhibits the forward rates of the reforming and water-gas shift reactions.

In contrast, the membrane reactor (Figure 5.11a) demonstrates the key advantage of Le Châtelier's principle. The H_2 molar fraction in the retentate (green line) rises to a peak early in the reactor (approximately Z=0.2 m) and is then actively suppressed as it permeates through the membrane. This continuous removal of a product dramatically shifts the reaction equilibrium forward. As a result, the methanol conversion is significantly enhanced, approaching near-complete conversion well before the reactor outlet. Furthermore, the cumulative molar fraction of permeated H_2 (purple line) steadily increases, representing the successful recovery of the purified product.

3.2 Temperature profiles comparison

The temperature profiles shown in Figure 5.12 provide critical insight into the thermal behaviour and energy balance of the two reactor configurations. Both profiles exhibit the characteristic "cold spot" near

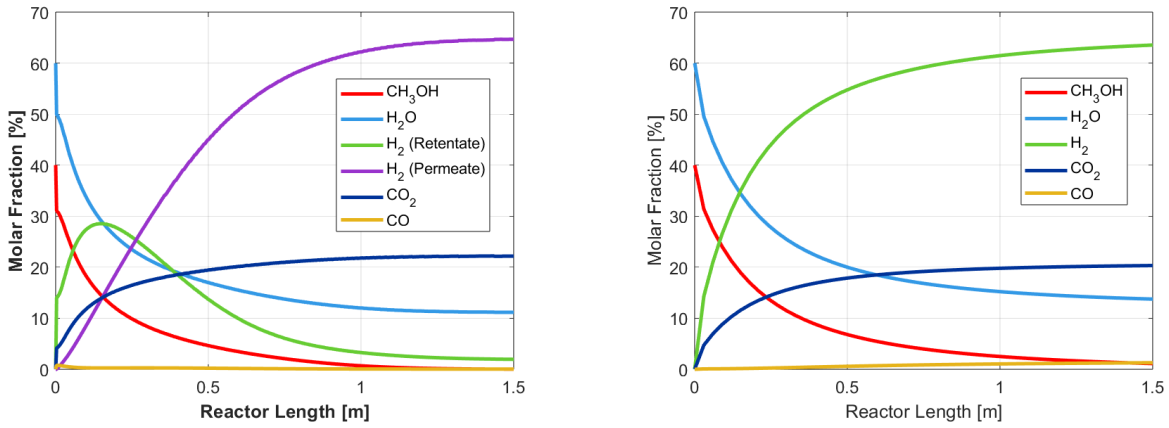

(a) Molar composition profiles at design point in the membrane reactor (Configuration A).

(b) Molar composition profiles at design point in the packed-bed reactor (Configuration B).

Figure 5.11: Comparison of molar composition profiles for (a) Configuration A and (b) Configuration B.

the reactor inlet (Z ≈ 0.15 m), where the temperature of the process stream drops sharply due to the highly endothermic nature of the methanol steam reforming reactions.

For the conventional packed-bed reactor (Figure 5.12b), after the initial drop to approximately 250 °C, the process temperature gradually recovers as heat transfer from the hotter utility fluid (red line) becomes dominant over the slowing reaction rate. The temperature difference between the process and thermal fluid diminishes along the reactor length, consistent with a standard co-current heat exchange configuration.

The membrane reactor (Figure 5.12a) displays a more pronounced and distinct thermal profile. The initial endothermic drop is more severe, with the process temperature falling to approximately 230 °C. This is attributable to a higher initial reaction rate, which is sustained by the continuous removal of hydrogen. However, following this minimum, the process stream temperature exhibits a significant recovery, rising to a peak of approximately 260 °C. This reheating is driven by two coupled effects: the continuous heat transfer from the external thermal fluid, and the decrease in the retentate thermal mass as hydrogen is selectively removed through the membrane. As the mass flow rate of the retentate decreases along the reactor, a given amount of heat input from the utility fluid results in a greater temperature rise.

It is important to note that the coaxial tube geometry was modelled with the assumption that permeation is isothermal, meaning the hydrogen leaves the retentate and enters the permeate phase at the same local temperature. Consequently, the model does not account for heat transfer through the inner membrane tube wall. This simplification effectively treats the membrane as an adiabatic boundary, or an insulator, between the reacting annular space and the permeate collection channel (see Figure 3.6b in the methodology chapter).

The ability of the User2 model to capture this thermodynamically consistent profile, where the process temperature correctly responds to the interplay of endothermic reaction, heat transfer, and mass removal without non-physical crossovers, serves as a crucial validation of the explicit energy balance implemented in the custom subroutine.

3.3 Pressure profiles comparison

The pressure drop across the packed catalyst bed is a critical operational parameter, influencing reactor mechanical design, and reaction kinetics through its effect on partial pressures. A significant difference in both the magnitude and the shape of the pressure profiles was observed between the two reactor configurations, as shown in Figure 5.13a and Figure 5.13b.

Three key distinctions are evident from the profiles. First, the absolute operating pressure is substantially different: Configuration A operates with an inlet pressure of 20 bar, while Configuration B operates at 10 bar. This higher pressure in the membrane reactor is a deliberate design choice to provide a large driving force for hydrogen permeation across the membrane, which requires a significant partial pressure difference.

Second, the magnitude of the pressure drop varies dramatically. Configuration A exhibits a significant pressure drop of approximately 1.3 bar over the 1.5 m reactor length. In contrast, Configuration B shows a negligible pressure drop of less than 0.005 bar. This pronounced difference is attributable to two primary

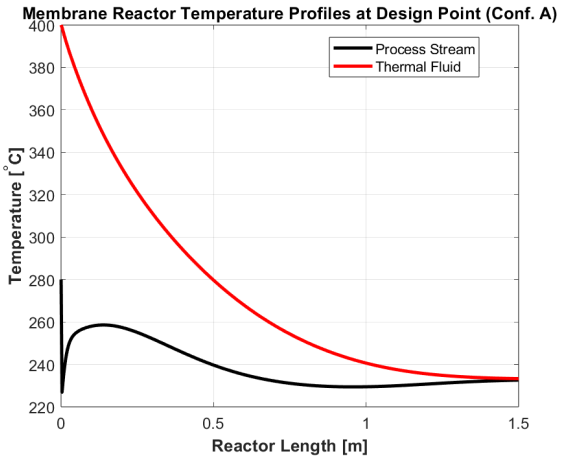

(a) Temperature profile at design point in the membrane reactor (Configuration A).

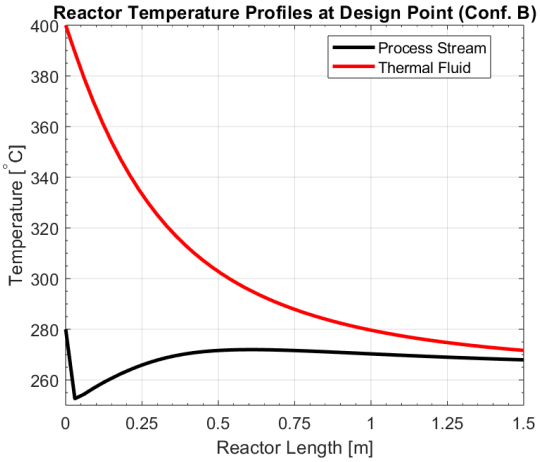

(b) Temperature profile at design point in the packed-bed reactor (Configuration B).

Figure 5.12: Comparison of temperature profiles for (a) Configuration A and (b) Configuration B.

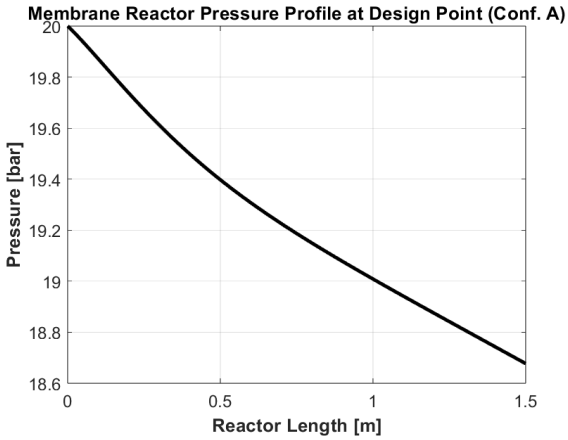

(a) Pressure profile in the membrane reactor.

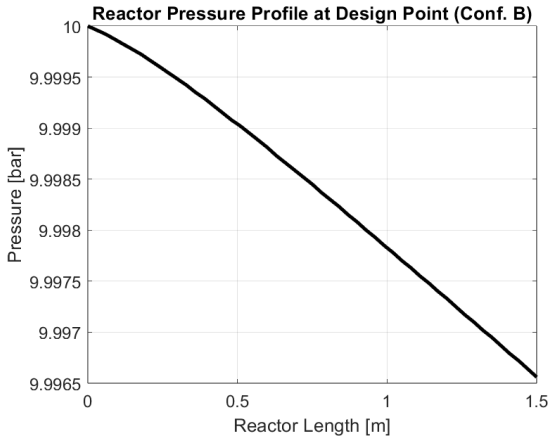

(b) Pressure profile in the packed-bed reactor.

Figure 5.13: Comparison of pressure profiles in the reformers: (a) Configuration A and (b) Configuration B.

factors. The most significant is the difference in the catalyst particle size specified for each model; a smaller particle diameter of 1 mm was used for Configuration A, whereas a larger 4 mm particle was used for Configuration B. According to the Ergun equation (see Equation 3.12 in the methodology), pressure drop is inversely proportional to the particle diameter ($\Delta P \propto 1/D_p$) and its square ($\Delta P \propto 1/D_p^2$) in the laminar and turbulent flow regimes, respectively, thus smaller particles inherently lead to a much higher pressure drop. Additionally, while both models are based on the Ergun equation, the explicit implementation within the custom User2 subroutine for Configuration A provides a more rigorous calculation compared to the simplified built-in function of the standard `R-Plug` block used for Configuration B.

Finally, the shape, or concavity, of the pressure profiles is different. The pressure profile for Configuration B is nearly linear, showing a slight downward concavity (i.e., the rate of pressure drop, $|dP/dz|$, increases slightly along the length). This is typical for a conventional packed-bed reactor where the gas density and viscosity change moderately with temperature and composition. On the other hand, the profile for Configuration A exhibits a distinct upward concavity, meaning the pressure gradient is steepest near the reactor inlet. This is a direct consequence of the mass removal through the membrane. According to the Ergun equation, pressure drop is strongly dependent on the superficial fluid velocity ($\Delta P \propto v_s$ and $\propto v_s^2$). In a conventional packed-bed reactor, the total mass flow is constant. In the membrane reactor, as hydrogen permeates out, the total molar and mass flow rate of the retentate stream decreases along the reactor length. To maintain the same flow of the remaining components through a smaller flow area, or simply due to the change in mass flux, the superficial velocity term in the Ergun equation is affected. The continuous removal of mass would typically decrease the pressure drop gradient along the length.

As expected, the observed upward concavity (steeper drop at the beginning) therefore aligns with the theory enhancing the validation of the Configuration A model. The temperature drop and recovery also play a significant role, as gas density (ρ) increases dramatically in the cold spot, which increases the pressure drop in that region according to the inertial term of the Ergun equation ($\Delta P \propto \rho v_s^2$). The complex shape is a testament to the strong coupling between reaction, permeation, heat transfer, and momentum transfer captured by the User2 model.

4 PEMFC results

Figure 5.14 shows the performance results of the PEMFC designed for this process. Overall the trends of the polarization curve, power density curve and efficiency curve aligns with the trend shown in Figure 4.1 in the model validation chapter. The simulated polarization curve correctly exhibits the characteristic regions of voltage loss: a quasi-linear region where ohmic losses are dominant, and a sharp voltage drop at high current densities (J > 0.6 A/cm²) due to concentration overpotential. Similarly, the power density curve demonstrates the expected parabolic behaviour, rising to a peak of approximately 0.28 W/cm² at an optimal current density of around 0.45 A/cm² before declining due to overpowering voltage losses. Finally, the efficiency curve correctly shows the inverse relationship between current density and thermodynamic efficiency, decreasing from over 60% at low loads to under 20% at high loads. Moreover, the curves drop to zero around J=0.7 A/cm^2 as expected since $J_{\max} = 0.672$ A/cm^2 as stated in the methodology in Table 3.4.

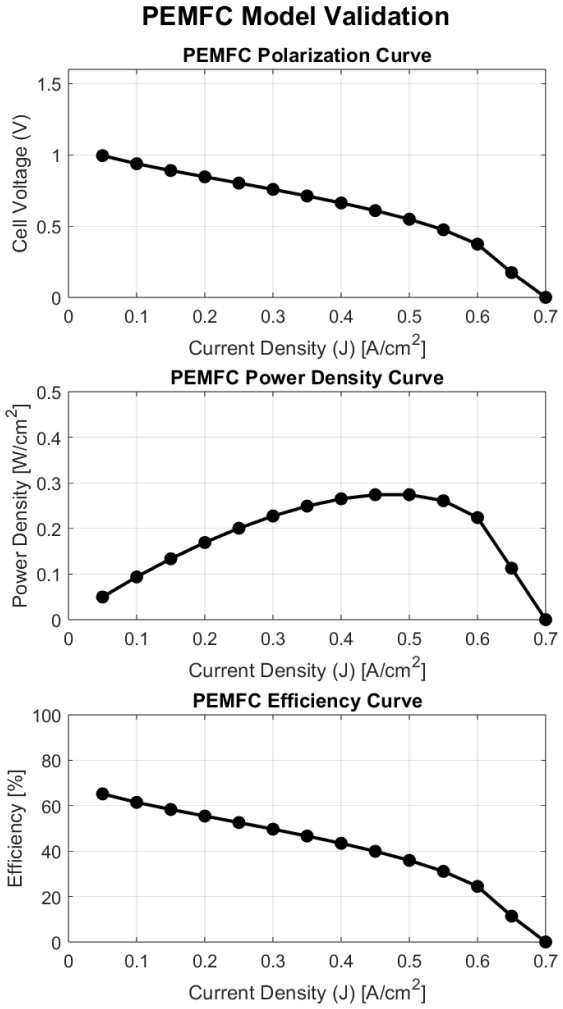

Figure 5.14: PEMFC performance results.

Chapter 6

Operating cost analysis

1 Introduction

Following the comprehensive technical evaluation of the integrated membrane reactor (Configuration A) and the conventional packed-bed reactor with a separate membrane unit (Configuration B), this chapter presents a comparative techno-economic analysis. The primary objective is to translate the observed performance differences such as fuel consumption, component sizing, and operational efficiency—into tangible economic metrics. This analysis is crucial for answering the core research question regarding the techno-economic trade-offs of the two system architectures for on-board ship applications.

A complete techno-economic assessment typically involves evaluating both Capital Expenditure (CAPEX) and Operational Expenditure (OPEX). However, a deliberate and strategic decision has been made in this study to focus exclusively on a detailed OPEX analysis. This approach is necessitated by the highly customized and novel nature of the core components modelled in this thesis.

The primary components, particularly the integrated membrane reactor in Configuration A and the separate high-flux membrane unit in Configuration B, are not standard, off-the-shelf items. Their manufacturing costs are subject to significant variability depending on fabrication techniques, economies of scale, and the specific manufacturer, factors that are beyond the scope of this process-modelling-focused research. A CAPEX estimation would therefore rely on a cascade of high-uncertainty assumptions, potentially obscuring the true economic drivers of the systems.

In contrast, the OPEX is directly and robustly quantifiable from the high-fidelity simulation results already generated. Key operational cost drivers such as: fuel consumption, components longevity and maintenance needs.

To ground the analysis in a realistic operational scenario, the economic calculations are based on an annual operational time-frame of 6100 hours. This value is derived directly from the power load data provided by Feadship for the design vessel (see Figure A.1 and Figure A.2). This specific usage profile is critical for accurately calculating the total annual fuel consumption and for determining the true calendar lifetime of components whose degradation is dependent on operating hours, such as the PEMFC stack and the reforming catalyst.

To ensure a fair and consistent economic comparison, it was necessary to adjust all capital-related cost data sourced from literature to a common basis, which for this project is the reference year 2025. This normalization was performed using the Chemical Engineering Plant Cost Index (CEPCI) [19], a widely recognized industry standard that tracks the changing costs of process equipment, materials, and labour over time. The adjustment is made using the following formula:

$$Cost_{new} = Cost_{old} \times \frac{CEPCI_{new}}{CEPCI_{old}} \tag{6.1}$$

The values of the CEPCI index for the years of reference of the data used in this analysis are summarized in Table 6.1.

Table 6.1: CEPCI index values from 2021 to June 2025 [19].

Year	CEPCI
2021	708.8
2022	795.5
2023	810.1
2024	838.5
June 2025	850.2

2 Operating costs breakdown

To understand the economic drivers behind each configuration, the Total Annual Operating Cost (OPEX) was broken down into its four primary contributors: fuel cost, catalyst replacement, membrane replacement, and PEMFC stack replacement. The individual annual cost for each of these components is illustrated in Figure 6.1, while Figure 6.2 provides a stacked comparison of the total annual OPEX. Each component's cost is analysed in the following subsections.

2.1 Annual fuel cost

The cost of bio-methanol is the dominant factor in the annual OPEX for both systems. This cost was calculated from the detailed, load-dependent fuel consumption rates determined in the Aspen Plus simulations, summed over the vessel's 6100 operational hours per year. To establish a realistic fuel price, a comprehensive literature review was conducted. Based on the IRENA Innovation Outlook report [66] and a recent study by Tariq et al. [67], a representative production cost of \$600/tonne (510 €/tonne) in 2022 was selected as a baseline. To account for significant inflation in energy and logistics between 2022 and the project year of 2025, a conservative 15% inflation factor was applied, resulting in a final fuel price of approximately 587 €/tonne.

The top-left subplot of Figure 6.1 illustrates the resulting annual fuel costs. Configuration A incurs a fuel cost of 408,955 €, while Configuration B demonstrates a clear advantage with a lower cost of 398,924 €. This annual saving for Configuration B is a direct consequence of its superior thermal integration, which reduces the need for supplementary methanol in the burner compared to the fuel-depleted retentate stream from the highly efficient membrane reactor in Configuration A.

2.2 Annual catalyst replacement cost

The recurring cost of replacing the reforming catalyst was calculated using the annualized replacement cost method. A specific cost of 25 €/kg was assumed for a commercial $Cu/ZnO/Al_2O_3$ catalyst [68]. This total replacement cost was annualized over a standard operational lifetime of 17,520 hours, which corresponds to a calendar lifetime of approximately 2.87 years given the vessel's 6100 annual operating hours.

The top-right subplot of Figure 6.1 presents these costs. The annual catalyst replacement cost for Configuration A (390 kg catalyst mass) is 3,395 €, and for Configuration B (380.2 kg catalyst mass) it is 3,309 €. As these values are very similar and represent a negligible fraction of the total OPEX (as shown in Figure 6.2), catalyst replacement is not a significant economic differentiator between the two designs.

2.3 Annual Pd membrane replacement cost

The replacement of the palladium membrane is a major operational expense and a key differentiator between the two configurations. The calculation was based on data from Sweeney et al. [69], assuming a specific cost of \$10,000/m^2 (in 2022 dollars) and a calendar lifetime of 3 years. This cost was adjusted to a 2025 value using the CEPCI inflation factor and currency conversion. This calendar-based lifetime was chosen as it appropriately reflects degradation from thermal cycling stress, a primary failure mode for metallic membranes.

The economic penalty of the integrated design is starkly illustrated in the bottom-left subplot of Figure 6.1. Configuration A, with its large 20 m^2 membrane, incurs a substantial annual cost of 60,563 €. In contrast, Configuration B, requiring a smaller 10.5 m^2 membrane, has an annual cost of only 31,796 €. This significant difference is a major disadvantage for the integrated reactor design.

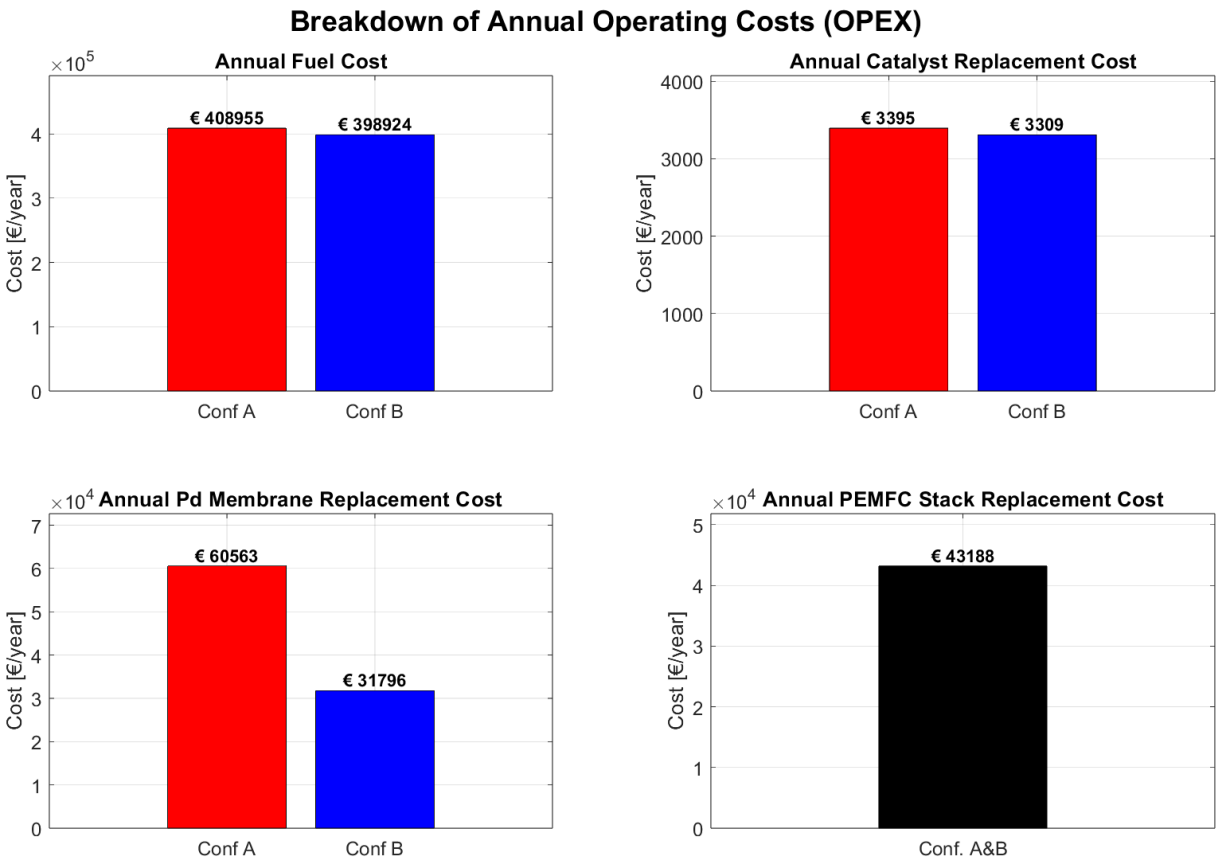

Figure 6.1: Breakdown of annual operating costs.

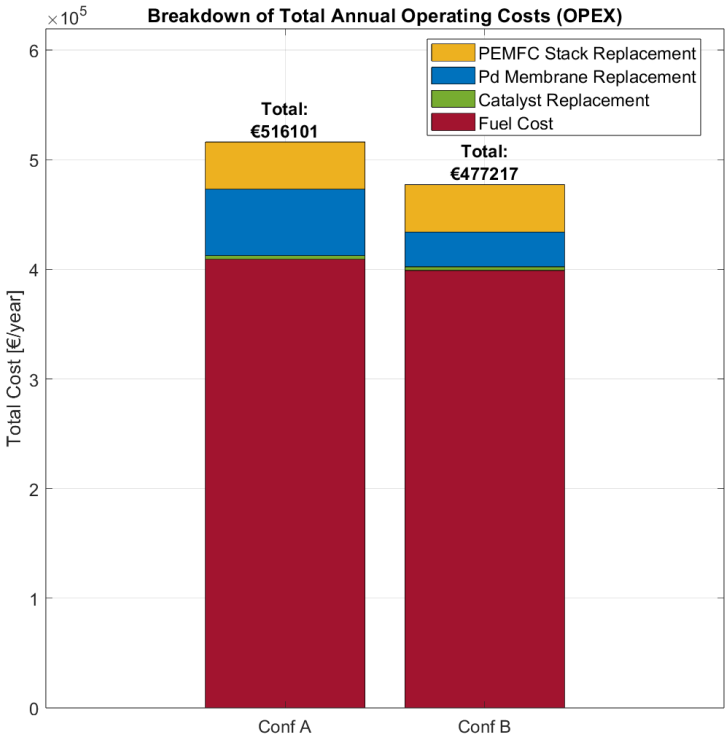

Figure 6.2: Total annual operating costs comparison.

2.4 Annual PEMFC stack replacement cost

The periodic replacement of the PEMFC stack is a significant OPEX component, identical for both systems as they utilize the same 325 kW power unit. The cost was derived from data in Fontalvo et al. [70], which

reports a specific replacement cost of $400/kW (in 2021 dollars). This value was adjusted for inflation to the project year 2025 using the CEPCI. To accurately reflect the wear and tear associated with variable-load operation, the total annual replacement cost was calculated by summing the costs incurred at each power level within the yacht's operational profile, rather than assuming constant operation at the rated 325 kW. This load-dependent cost was then annualized over the stack's total operational lifetime of 15,000 hours, which equates to a calendar lifetime of 2.46 years based on the vessel's specific annual usage of 6100 hours.

The bottom-right subplot of Figure 6.1 shows the resulting annual replacement cost of 43,188 €. As seen in Figure 6.2, this is the second-largest cost driver after fuel for Configuration B, highlighting the critical role of stack durability in the economic viability of maritime fuel cell applications.

Chapter 7

Conclusions

This thesis successfully developed and compared two distinct process configurations for onboard power generation via methanol steam reforming: an integrated membrane reactor system (Configuration A) and a conventional packed-bed Reactor with a separate purification unit system (Configuration B). The primary objective was to evaluate the techno-economic trade-offs for a Feadship super-yacht application. Through detailed, custom-developed models in Aspen Plus, supported by Fortran subroutines for core unit operations, the following conclusions were drawn in response to the research questions:

RQ 1: What are the techno-economic trade-offs of implementing a membrane reactor versus a conventional packed-bed reactor with a separation unit for shipboard LT-PEMFC applications?

A fundamental trade-off between unit-level reaction efficiency, system-level thermal efficiency, and operational cost was identified.

The membrane reactor (Configuration A) demonstrated superior methanol conversion efficiency (across the whole power range analysed) due to the in-situ removal of hydrogen, which shifts the reaction equilibrium. However, this high conversion resulted in a fuel-depleted retentate stream, necessitating a significant flow of supplementary methanol to the burner for heat integration.

The packed-bed reactor (Configuration B), while achieving slightly lower methanol conversion, produced a fuel-rich retentate that significantly reduced the need for supplementary fuel. This superior thermal integration led to a higher overall system efficiency for Configuration B (≈45%) compared to Configuration A (≈43%) at the design point.

From an operational cost (OPEX) perspective, this efficiency advantage directly translated to lower annual fuel costs, which represent the largest single operating expense. Furthermore, the integrated design of Configuration A required a larger total membrane area (20 m^2) compared to the separate purification unit in Configuration B (10.5 m^2). This resulted in a significantly higher estimated annual membrane replacement cost for Configuration A, making Configuration B the more favourable option from both a thermal efficiency and operational expenditure standpoint for this application.

RQ 2: What are the optimal operating conditions and sizes for the methanol steam reformer, the separation unit and the PEMFC for the power demand use cases of the Feadship superyacht?

The optimal operating conditions represent a complex trade-off between maximizing hydrogen yield, ensuring catalyst stability, and maintaining overall system efficiency. The sizes of each component, determined through an iterative design process detailed in the methodology, are summarized below for each configuration.

For the membrane reactor (Configuration A), an aggressive operating pressure of 20 bar was selected to maximize the partial pressure driving force for hydrogen permeation. To achieve the target hydrogen production, the reactor was sized to contain 212 coaxial tubes of 1.5 m length, incorporating a total membrane area of 20 m^2 and a catalyst mass of 390 kg. A catalyst bed temperature was maintained below 300 °C, achieved with a utility fluid inlet temperature of 400 °C. The optimal burner O_2 excess was found to be 140%, balancing complete combustion with thermal losses from the fuel-depleted retentate.

For the packed-bed reactor (Configuration B), a lower operating pressure of 10 bar was sufficient as reaction and separation are decoupled. The reformer was designed with 156 tubes of 1.5 m length, containing a comparable catalyst mass of 380.2 kg. Similar temperature constraints were applied. The hydrogen purification stage was modelled as a separate membrane unit requiring a significantly smaller area of 10.5 m^2 due to the higher hydrogen partial pressure of the feed. Due to the fuel-rich retentate from the less efficient reforming stage, a much higher O_2 excess of 270% was required in the burner to achieve complete combustion and meet heat integration targets.

The PEMFC in both configurations was sized to meet the 325 kW design point. This required a stack composed of 1200 individual cells, each with an active area of 1200 cm^2. The fuel cell was operated under consistent conditions of 80 °C (353 K) and inlet O_2 and H_2 partial pressures of 0.2095 atm and 1.47628 atm respectively, with a current density of 0.3 A/cm^2. This highlights the necessity of conditioning the product streams from both reformer types to meet these consistent downstream requirements. A comprehensive list of the final design parameters for both configurations is detailed in Table 3.6 and Table 3.8.

RQ 3: What are the key challenges and opportunities in integrating heat recovery strategies into the system?

Heat integration was identified as the most critical factor determining the overall efficiency and viability of both systems.

The primary opportunity lies in utilizing the high-temperature waste heat from the burner. This high-quality heat source was successfully implemented to vaporize and preheat the liquid methanol-water feed, satisfying the largest heat sink in the process. A second significant opportunity is the recovery of low-grade waste heat from the PEMFC coolant loop. This hot water stream represents a valuable low-temperature heat source that could be used for other onboard duties, such as providing domestic hot water for the vessel.

The key challenge is the trade-off between reformer conversion and the fuel value of the retentate, which has a strong, direct influence on the burner and its air feed requirements. A highly efficient reformer (Configuration A) produces a fuel-depleted retentate, forcing a high reliance on supplementary fuel. In contrast, a less efficient reformer (Configuration B) produces a fuel-rich retentate, requiring less supplementary fuel but a much higher flow of combustion air (higher O_2 excess) to control the flame temperature and ensure complete combustion. This study concludes that for a tightly integrated system where the retentate is a primary fuel source, the superior thermal self-sufficiency of Configuration B system proved more advantageous.

The heat integration strategy was found to be the primary driver of CO_2 output. Configuration B's lower reliance on supplementary fuel resulted in lower total fuel consumption and correspondingly lower specific CO_2 emissions. A significant future opportunity exists in managing these emissions. The burner flue gas represents a relatively concentrated CO_2 stream suitable for onboard carbon capture. This captured CO_2 could be stored and sold onshore or, more ambitiously, used in a closed-loop fuel cycle. By integrating a water electrolyser, the resulting green hydrogen could be combined with the captured CO_2 to synthesize renewable e-methanol directly on the vessel, representing a complete circular carbon economy and a pathway to near-zero net emissions.

Overall system viability and comparison to marine technology

In conclusion, this research shows that the conventional packed-bed reactor with a separate membrane (Configuration B) is the superior architecture for this specific application, offering a better balance of high conversion, excellent thermal integration, and lower operational costs.

Furthermore, when compared to the marine diesel engine technology, both modelled MSR-PEMFC systems present compelling advantages. With peak electrical efficiencies approaching 60%, they significantly outperform typical marine diesels in this power class, which have peak efficiencies of 42-48% and suffer from considerable efficiency losses at part-load. This is a critical advantage for the variable load profiles of a super-yacht. From an environmental perspective, the benefits are even more pronounced. The use of sulphur-free methanol eliminates SOx emissions entirely, while the low-temperature electrochemical process of the PEMFC produces zero NOx and particulate matter (PM), which are major pollutants from diesel combustion subject to strict maritime regulations. While the system does produce CO_2, the potential to use green methanol offers a clear pathway to a carbon-neutral power solution. Combined with the qualitative benefits of silent, vibration-free operation ideal for luxury marine applications, this study demonstrates that the methanol reformer-PEMFC architecture presents a technologically superior and viable alternative to conventional diesel engines.

Chapter 8

Model limitations

While the custom models developed in this study provide a robust basis for system comparison, it is important to acknowledge their inherent limitations, which define the scope of the conclusions and provide avenues for future refinement.

A significant factor influencing the comparative results was the selection of the design point for each configuration, particularly the burner's excess O_2 level. Configuration A was optimized for a high methanol conversion of >99%, while Configuration B was optimized to meet a minimum conversion target of 95% while maximizing its thermal integration potential. This asymmetric design basis, while meeting all performance constraints, inherently favours Configuration B in terms of overall system efficiency due to the higher fuel value of its retentate. This highlights that the conclusions are strongly tied to the specific design targets chosen. However, this influences only the design point and not all the other power set points investigated, which have provided consistent results.

Furthermore, the performance of each system is highly sensitive to the sizing of its core components. The results presented are based on a specific set of design parameters for membrane area, catalyst mass, and base operating conditions such as the reformer's temperature and pressure. It is conceivable that a different set of sizing parameters, for instance a significantly larger membrane area in Configuration A or a different catalyst loading in Configuration B could alter the balance between reaction efficiency and heat integration, potentially leading to a different optimal configuration. The conclusions drawn are therefore representative of the specific designs evaluated and not necessarily a universal statement for all possible sizes of these systems.

The simulations were also conducted under steady-state conditions for various discrete power loads. This approach does not capture the transient behaviour of the system, such as start-up dynamics or the response to rapid load changes characteristic of a super-yacht.

The modelling of auxiliary components was also simplified. Parasitic energy loads for air blowers were not included, meaning the reported net power output and system efficiencies are optimistic. Moreover, the difference in the airflow blowers of the two configurations was not included leaning in favour of configuration B which uses more mass without drawbacks of power. Similarly, the burner was modelled as an ideal reactor with complete combustion, which does not account for real-world limitations like flame stability.

Finally, the models assumed perfect hydrogen selectivity for the membranes and did not account for the long-term degradation of the catalyst, membrane, or PEMFC stack. These factors, along with the simplified fluid property calculations within the custom models, represent key areas for future, more detailed investigation.

Chapter 9

Recommendations for future work

The findings and limitations of this study provide a strong foundation for further research into methanol-reforming PEMFC systems for maritime applications.

The most critical next step is to extend the developed steady-state models into the Aspen Plus Dynamics environment. The real-world load profile of a super-yacht is highly transient, and a steady-state analysis cannot capture the system's response to these changes. A dynamic simulation would be essential to investigate key performance aspects such as reformer start-up time, catalyst bed thermal inertia, and the system's ability to follow rapid changes in power demand. This would also facilitate the design and testing of a comprehensive control strategy for managing the reformer temperature, supplementary burner fuel, and reactant flow rates to ensure stable and efficient operation across the entire load profile.

While this study focused on operational performance and key OPEX drivers, a full Capital Expenditure (CAPEX) analysis is necessary for a complete techno-economic assessment. The integrated membrane reactor (Configuration A), despite showing lower thermal efficiency in this study, may offer a smaller physical footprint and lower component count (e.g., fewer heat exchangers, no separate large purification unit). In a space- and weight-constrained maritime application, these factors could translate to significant CAPEX advantages. A detailed CAPEX estimation, considering equipment sizing, materials, and fabrication complexity, would provide a more holistic comparison and could potentially alter the final conclusion on the most favourable system architecture.

To obtain a more accurate measure of the true net system efficiency, the model should be expanded to include detailed models for key Balance-of-Plant components. This includes explicitly modelling the parasitic energy loads of air blowers. The power consumption of these auxiliaries, especially the air blower for the burner in Configuration B at high excess O_2, is likely to be a significant factor and would reduce the net electrical efficiency of both systems.

Furthermore, the assumption of perfect hydrogen selectivity should be relaxed. Future models could include the permeation of other species (CO, CO_2) based on literature selectivity data to assess the impact on PEMFC performance and determine the need for anode gas purging, leading to a more realistic representation of the integrated system.

Bibliography

[1] Nasa Global Climate Change. Global Surface Temperature | NASA Global Climate Change, January 2025. URL https://climate.nasa.gov/vital-signs/global-temperature/?intent=121.

[2] European Union. Regulation - 2023/1805 - EN - EUR-Lex, February 2025. URL https://www.cfp.energy/en/insights/decarbonising-shipping.

[3] Jon Anders. Comparison of alternative marine fuels sealtd. 2019. ISSN 2019-0567. URL https://sea-lng.org/wp-content/uploads/2020/04/Alternative-Marine-Fuels-Study_final_report_25.09.19.pdf.

[4] Gabriel Garcia, Emmanuel Arriola, Wei Hsin Chen, and Mark Daniel De Luna. A comprehensive review of hydrogen production from methanol thermochemical conversion for sustainability, 2 2021. ISSN 03605442. URL https://doi.org/10.1016/j.energy.2020.119384.

[5] J.M. Andújar and F. Segura. Fuel cells: History and updating. a walk along two centuries. *Renewable and Sustainable Energy Reviews*, 13(9):2309–2322, 2009. ISSN 1364-0321. doi: https://doi.org/10.1016/j.rser.2009.03.015. URL https://www.sciencedirect.com/science/article/pii/S1364032109001336.

[6] Kajornsak Faungnawakij, Ryuji Kikuchi, and Koichi Eguchi. Thermodynamic evaluation of methanol steam reforming for hydrogen production. *Journal of Power Sources*, 161:87–94, 10 2006. ISSN 03787753. doi: 10.1016/j.jpowsour.2006.04.091.

[7] Jimin Zhu, Samuel Simon Araya, Xiaoti Cui, and Søren Knudsen Kær. The role of effectiveness factor on the modeling of methanol steam reforming over cuo/zno/al2o3 catalyst in a multi-tubular reactor. *International Journal of Hydrogen Energy*, 47(14):8700–8715, 2022. ISSN 0360-3199. doi: https://doi.org/10.1016/j.ijhydene.2021.12.223. URL https://www.sciencedirect.com/science/article/pii/S0360319921050254.

[8] A. Iulianelli, P. Ribeirinha, A. Mendes, and A. Basile. Methanol steam reforming for hydrogen generation via conventional and membrane reactors: A review, 2014. ISSN 13640321.

[9] Zhemin Du, Congmin Liu, Junxiang Zhai, Xiuying Guo, Yalin Xiong, Wei Su, and Guangli He. A review of hydrogen purification technologies for fuel cell vehicles, 3 2021. ISSN 20734344.

[10] Vincenzo Palma, Daniela Barba, Eugenio Meloni, Concetta Ruocco, and Marco Martino. Chapter 2 - membrane reactors for h2 and energy production. In Angelo Basile and Têko W. Napporn, editors, *Current Trends and Future Developments on (Bio-) Membranes*, pages 33–56. Elsevier, 2020. ISBN 978-0-12-817110-3. doi: https://doi.org/10.1016/B978-0-12-817110-3.00002-3. URL https://www.sciencedirect.com/science/article/pii/B9780128171103000023.

[11] Feadship / de Voogt Naval Architects. Memens f4 mbse pilot reduced use case. Internal document, Feadship / de Voogt Naval Architects, dec 2024. Design Ship Primary Power System.

[12] Jeferson M. Corrêa, Felix A. Farret, Luciane N. Canha, and Marcelo G. Simoes. An electrochemical-based fuel-cell model suitable for electrical engineering automation approach. *IEEE Transactions on Industrial Electronics*, 51:1103–1112, 10 2004. ISSN 02780046. doi: 10.1109/TIE.2004.834972.

[13] Selma Brynolf, Maria Grahn, Julia Hansson, Andrei David Korberg, and Elin Malmgren. *Sustainable fuels for shipping*, pages 403–428. Elsevier, 1 2022. ISBN 9780128244715. doi: 10.1016/B978-0-12-824471-5.00017-7. URL https://linkinghub.elsevier.com/retrieve/pii/B9780128244715000177.

[14] S. Mekhilef, R. Saidur, and A. Safari. Comparative study of different fuel cell technologies, 2012. ISSN 13640321.

[15] Lindert van Biert and Klaas Visser. *Fuel cells systems for sustainable ships*, pages 81–121. Elsevier, 1 2022. doi: 10.1016/B978-0-12-824471-5.00010-4. URL https://linkinghub.elsevier.com/retrieve/pii/B9780128244715000104.

[16] ISO 14687:2019, March 2025. URL https://www.iso.org/standard/69539.html. [Online; accessed 7. Mar. 2025].

[17] Arunabha Kundu, Yong Gun Shul, and Dong Hyun Kim. Methanol Reforming Processes. In *Advances in Fuel Cells*, volume 1, pages 419–472. Elsevier Science, Walthm, MA, USA, January 2007. doi: 10.1016/S1752-301X(07)80012-3.

[18] Jimin Zhu, Samuel Simon Araya, Xiaoti Cui, Simon Lennart Sahlin, and Søren Knudsen Kær. Modeling and design of a multi-tubular packed-bed reactor for methanol steam reforming over a cu/zno/al2o3 catalyst. *Energies*, 13, 2020. ISSN 19961073. doi: 10.3390/en13030610.

[19] The Chemical Engineering Plant Cost Index. URL https://www.chemengonline.com/pci-home.

[20] Juhi Yadav, Avinash Kumar, and Rahul Mohan. Dramatic decline of Arctic sea ice linked to global warming. *Nat. Hazards*, 103(2):2617–2621, September 2020. ISSN 1573-0840. doi: 10.1007/s11069-020-04064-y.

[21] Nasa Global Climate Change. Carbon Dioxide Concentration | NASA Global Climate Change, January 2025. URL https://climate.nasa.gov/vital-signs/carbon-dioxide/?intent=121. [Online; accessed 31. Jan. 2025].

[22] WFJ Evans, Trent University, E Puckrin, and D Canada-Valcartier. Measurements of the radiative surface forcing of climate. URL https://ams.confex.com/ams/pdfpapers/100737.pdf.

[23] Lonnie G. Thompson. Climate change: The evidence and our options. *BEHAV ANALYST*, 33(2):153–170, October 2010. ISSN 2196-8918. doi: 10.1007/BF03392211.

[24] REN21 Renewables Global Status Report, November 2024. URL https://www.ren21.net/wp-content/uploads/2019/05/GSR2025_Factsheet_Demand_Transport.pdf.

[25] Richa Sharma, Amit Kumar, and Rajesh K. Upadhyay. Performance comparison of methanol steam reforming integrated to pd-ag membrane: Membrane reformer vs. membrane separator. *Separation and Purification Technology*, 183:194–203, 2017. ISSN 18733794. doi: 10.1016/j.seppur.2017.04.006.

[26] P. Ribeirinha, M. Abdollahzadeh, M. Boaventura, and A. Mendes. H2production with low carbon content via msr in packed bed membrane reactors for high-temperature polymeric electrolyte membrane fuel cell. *Applied Energy*, 188:409–419, 2017. ISSN 03062619. doi: 10.1016/j.apenergy.2016.12.015.

[27] P. Ribeirinha, M. Abdollahzadeh, A. Pereira, F. Relvas, M. Boaventura, and A. Mendes. High temperature pem fuel cell integrated with a cellular membrane methanol steam reformer: Experimental and modelling. *Applied Energy*, 215:659–669, 4 2018. ISSN 03062619. doi: 10.1016/j.apenergy.2018.02.029.

[28] A. Graeeli, M. Rahimi-Esbo, V. Kord Firouzjaee, M. Sedighi, and M. Rezaee Firouzjaee. Steam reforming of methanol and reactor optimization for additional hydrogen production: Process simulation. *Iranica Journal of Energy and Environment*, 15:142–150, 2024. ISSN 20792115. doi: 10.5829/ijee.2024.15.02.03.

[29] Julia Hansson, Selma Brynolf, Erik Fridell, and Mariliis Lehtveer. The potential role of ammonia as marine fuel-based on energy systems modeling and multi-criteria decision analysis. *Sustainability (Switzerland)*, 12, 4 2020. ISSN 20711050. doi: 10.3390/SU12083265.

[30] Selma. Brynolf. *Environmental assessment of present and future marine fuels*. Chalmers University of Technology, 2014. ISBN 9789175970066. URL https://research.chalmers.se/publication/196899/file/196899_Fulltext.pdf.

[31] Maria Grahn, Elin Malmgren, Andrei D. Korberg, Maria Taljegard, James E. Anderson, Selma Brynolf, Julia Hansson, Iva Ridjan Skov, and Timothy J. Wallington. Review of electrofuel feasibility - cost and environmental impact. *Progress in Energy*, 4, 7 2022. ISSN 25161083. doi: 10.1088/2516-1083/ac7937.

[32] Sustainability whitepaper: Hydrogen as marine fuel. Technical report, 2021.

[33] A. D. Korberg, S. Brynolf, M. Grahn, and I. R. Skov. Techno-economic assessment of advanced fuels and propulsion systems in future fossil-free ships. *Renewable and Sustainable Energy Reviews*, 142, 5 2021. ISSN 18790690. doi: 10.1016/j.rser.2021.110861.

[34] Patrycja Makos, Edyta Słupek, Joanna Sobczak, Dawid Zabrocki, Jan Hupka, and Andrzej Rogala. Dimethyl ether (dme) as potential environmental friendly fuel. In *E3S Web of Conferences*, volume 116. EDP Sciences, 9 2019. doi: 10.1051/e3sconf/201911600048.

[35] Sebastian Verhelst, James WG Turner, Louis Sileghem, and Jeroen Vancoillie. Methanol as a fuel for internal combustion engines. *Progress in Energy and Combustion Science*, 70:43–88, 1 2019. ISSN 03601285. doi: 10.1016/j.pecs.2018.10.001. URL https://linkinghub.elsevier.com/retrieve/pii/S036012851830042X.

[36] John J. Clary. *The Toxicology of Methanol*. Wiley, Hoboken, NJ, USA, January 2013. ISBN 978-0-470-31759-4. URL https://www.wiley.com/en-au/The+Toxicology+of+Methanol-p-9780470317594.

[37] Methanol Institute. Methanol safe handling manual. Technical report, Methanol Institute, 2017. URL https://www.methanol.org/wp-content/uploads/2017/03/Safe-Handling-Manual.pdf.

[38] Mohammed Alhassan and Mohammed Umar Garba. Design of an alkaline fuel cell leonardo electronic journal of practices and technologies design of an alkaline fuel cell. *Leonardo Electronic Journal of Practices and Technologies*, 2006. ISSN 1583-1078. URL http://lejpt.academicdirect.org.

[39] R. J. Unger, S. Kenner, M. J. Binder, and F. H. Holcomb. Phosphoric acid fuel cells. Technical report, US Army Corps of Engineers, 2004.

[40] R. J. Remick, D. Wheeler, and P. Singh. Mcfc and pafc rd workshop summary report. Technical report, U.S. Department of Energy, 2010.

[41] R. Mark Ormerod. Solid oxide fuel cells, 2003. ISSN 03060012.

[42] S C Singhal. Advances in solid oxide fuel cell technology. Technical report, Science and Technology Center Siemens Westinghouse Power Corporatio, 2000. URL www.elsevier.com/locate/ssi.

[43] Contributors to Wikimedia projects. Molten carbonate fuel cell - Wikipedia, February 2025. URL https://en.wikipedia.org/w/index.php?title=Molten_carbonate_fuel_cell&oldid=1274382256. [Online; accessed 4. Mar. 2025].

[44] T. Tronstad, H. H. Astrand, G. P. Haugom, and L. Langfeldt. Study on the use of fuel cells in shipping. Technical report, EMSA European Maritime Safety Agency, 2017. URL https://www.emsa.europa.eu/publications/reports/download/4545/2921/23.html.

[45] Kamaruzzaman Sopian and Wan Ramli Wan Daud. Challenges and future developments in proton exchange membrane fuel cells. *Renewable Energy*, 31:719–727, 2006. ISSN 09601481. doi: 10.1016/j.renene.2005.09.003.

[46] Feg Wen Chang, L. Selva Roselin, and Ti Cheng Ou. Hydrogen production by partial oxidation of methanol over bimetallic au-ru/fe2o3 catalysts. *Applied Catalysis A: General*, 334:147–155, 1 2008. ISSN 0926860X. doi: 10.1016/j.apcata.2007.10.003.

[47] Daniel G. Araiza, Antonio Gómez-Cortés, and Gabriela Díaz. Partial oxidation of methanol over copper supported on nanoshaped ceria for hydrogen production. *Catalysis Today*, 282:185–194, 3 2017. ISSN 09205861. doi: 10.1016/j.cattod.2016.06.055.

[48] Konstantinos Kappis, Joan Papavasiliou, and George Avgouropoulos. Methanol reforming processes for fuel cell applications, 12 2021. ISSN 19961073.

[49] J. Christopher Brown and Erdogan Gulari. Hydrogen production from methanol decomposition over pt/al 2o3 and ceria promoted pt/al2o3 catalysts. *Catalysis Communications*, 5:431–436, 8 2004. ISSN 15667367. doi: 10.1016/j.catcom.2004.05.008.

[50] Yanyong Liu, Takashi Hayakawa, Tomoko Ishii, Mikio Kumagai, Hiroyuki Yasuda, Kunio Suzuki, Satoshi Hamakawa, and Kazuhisa Murata. Methanol decomposition to synthesis gas at low temperature over palladium supported on ceria–zirconia solid solutions. *Applied Catalysis A: General*, 210(1):301–314, 2001. ISSN 0926-860X. doi: https://doi.org/10.1016/S0926-860X(00)00817-6. URL https://www.sciencedirect.com/science/article/pii/S0926860X00008176.

[51] Wu-Hsun Cheng. Reaction and xrd studies on cu based methanol decomposition catalysts: Role of constituents and development of high-activity multicomponent catalysts. *Applied Catalysis A: General*, 130(1):13–30, 1995. ISSN 0926-860X. doi: https://doi.org/10.1016/0926-860X(95)00102-6. URL https://www.sciencedirect.com/science/article/pii/0926860X95001026.

[52] A. A. Lytkina, N. V. Orekhova, and A. B. Yaroslavtsev. Methanol steam reforming in membrane reactors. *Petroleum Chemistry*, 58:911–922, 12 2018. ISSN 0965-5441. doi: 10.1134/S096554411811004X. URL http://link.springer.com/10.1134/S096554411811004X.

[53] Aspen Technology, Inc. *Aspen Plus User Models Reference Manual, Version 12.1*. Aspen Technology, Inc., Cambridge, MA, USA, version 12.1 edition, June 2003. URL https://esupport.aspentech.com/S_Article?id=000062943. Part of the Aspen Plus Reference Manuals series.

[54] B. Peppley, J. Amphlett, L. Kearns, and R. Mann. Methnol-steak reforming on cu/zn/al2o3 catalyst. part 2. a comprehnive kinetic model. *Applied Catalyst*, pages 31–49, 1999. URL https://www.sciencedirect.com/science/article/pii/S0926860X98002993?casa_token=nHqfvmQVCBMAAAAA:QFcYMUkk-xvRjbRRXL4KoqJMvwY_gWOuskBVepPCVDAhWPXRMciUH3JIERS78LO-xpP1Yb0fvQ.

[55] F. K. Sinurat, T. B. Sitorus, Taufik Bin Nur, and H. Susilo. *Simulation Analysis of Polymer Electrolyte Membrane Fuel Cell Using Aspen Plus*, volume 1566. Institute of Physics Publishing, 7 2020. doi: 10.1088/1742-6596/1566/1/012024.

[56] Lamei Xu and Jinsheng Xiao. Modeling and simulation of pem fuel cells based on electrochemical model. *IEEE*, 2011.

[57] Keoagile Mogorosi, M. Tunde Oladiran, and Edward Rakgati. Mathematical modelling and experimental investigation of a low temperature proton exchange membrane fuel cell. *Energy and Power Engineering*, 12:653–670, 2020. ISSN 1949-243X. doi: 10.4236/epe.2020.1211039.

[58] Homa Hamedi and Torsten Brinkmann. Rigorous and customizable 1d simulation framework for membrane reactors to, in principle, enhance synthetic methanol production. *ACS Sustainable Chemistry and Engineering*, 9:7620–7629, 6 2021. ISSN 21680485. doi: 10.1021/acssuschemeng.1c01677.

[59] B.H Howard, R.P Killmeyer, K.S Rothenberger, A.V Cugini, B.D Morreale, R.M Enick, and F Bustamante. Hydrogen permeance of palladium–copper alloy membranes over a wide range of temperatures and pressures. *Journal of Membrane Science*, 241(2):207–218, 2004. ISSN 0376-7388. doi: https://doi.org/10.1016/j.memsci.2004.04.031. URL https://www.sciencedirect.com/science/article/pii/S0376738804003606.

[60] Ray Sinnott and Gavin Towler. *Chemical Engineering Design*. Elsevier, 1 2019. ISBN 9780081025994. doi: 10.1016/B978-0-08-102599-4.09980-X.

[61] H. Scott Fogler. *Elements of Chemical Reaction Engineering*. Prentice Hall, Boston, 5th edition, 2016. ISBN 978-0-13-388751-8.

[62] Stephen R. Turns. *An Introduction to Combustion: Concepts and Applications*. McGraw-Hill, Boston, 3rd edition, 2011. ISBN 978-0073380193.

[63] L. D. Pfefferle and W. C. Pfefferle. Catalytically stabilized thermal combustion. *Catalysis Reviews*, 29(2-3):219–267, 1987. doi: 10.1080/01614948708078071.

[64] P. Forzatti and G. Groppi. Catalytic combustion for the production of energy. *Catalysis Today*, 54 (1):165–183, 1999. doi: 10.1016/S0920-5861(99)00186-5.

[65] Ronald F. Mann, John C. Amphlett, Michael A.I. Hooper, Heidi M. Jensen, Brant A. Peppley, and Pierre R. Roberge. Development and application of a generalised steady-state electrochemical model for a pem fuel cell. *Journal of Power Sources*, 86(1):173–180, 2000. ISSN 0378-7753. doi: https://doi.org/10.1016/S0378-7753(99)00484-X. URL https://www.sciencedirect.com/science/article/pii/S037877539900484X.

[66] Seungwoo. Kang. *Innovation outlook : renewable methanol*. International Renewable Energy Agency, 2021. ISBN 9789292603205. URL https://www.irena.org/-/media/Files/IRENA/Agency/Publication/2021/Jan/IRENA_Innovation_Renewable_Methanol_2021.pdf.

[67] Ghulam Tariq, Zhiwen Chen, and Ming Zhao. Techno-economic and life cycle assessment of integrated bio- and e-methanol production from biomass with carbon capture and utilization. *Chemical Engineering Journal*, 515, 7 2025. ISSN 13858947. doi: 10.1016/j.cej.2025.163850.

[68] Electro Power Cell Energy Technology (Shanghai) Co., Ltd. URL https://www.alibaba.com/product-detail/Copper-Zinc-Aluminum-Methanol-Reforming-Catalyst_1601244666112.html. Copper Zinc Aluminum Methanol Re forming Catalyst Efficient Hydrogen Generator for Green Energy Production. 2025.

[69] Dean M. Sweeney, Victor Alves, Savannah Sakhai, San Dinh, and Fernando V. Lima. Techno-economic analysis and optimization of intensified, large-scale hydrogen production with membrane reactors. *Industrial and Engineering Chemistry Research*, 62:19740–19751, 11 2023. ISSN 15205045. doi: 10.1021/acs.iecr.3c02045.

[70] Victor M. Fontalvo, George J. Nelson, Oscar Pupo-Roncallo, Marco E. Sanjuan, and Humberto A. Gómez. A techno-economic assessment for fuel cells hybrid systems in stationary applications. *International Journal of Sustainable Energy*, 42:889–912, 2023. ISSN 1478646X. doi: 10.1080/14786451.2023.2244605.

Appendix A

Feadship power load profiles

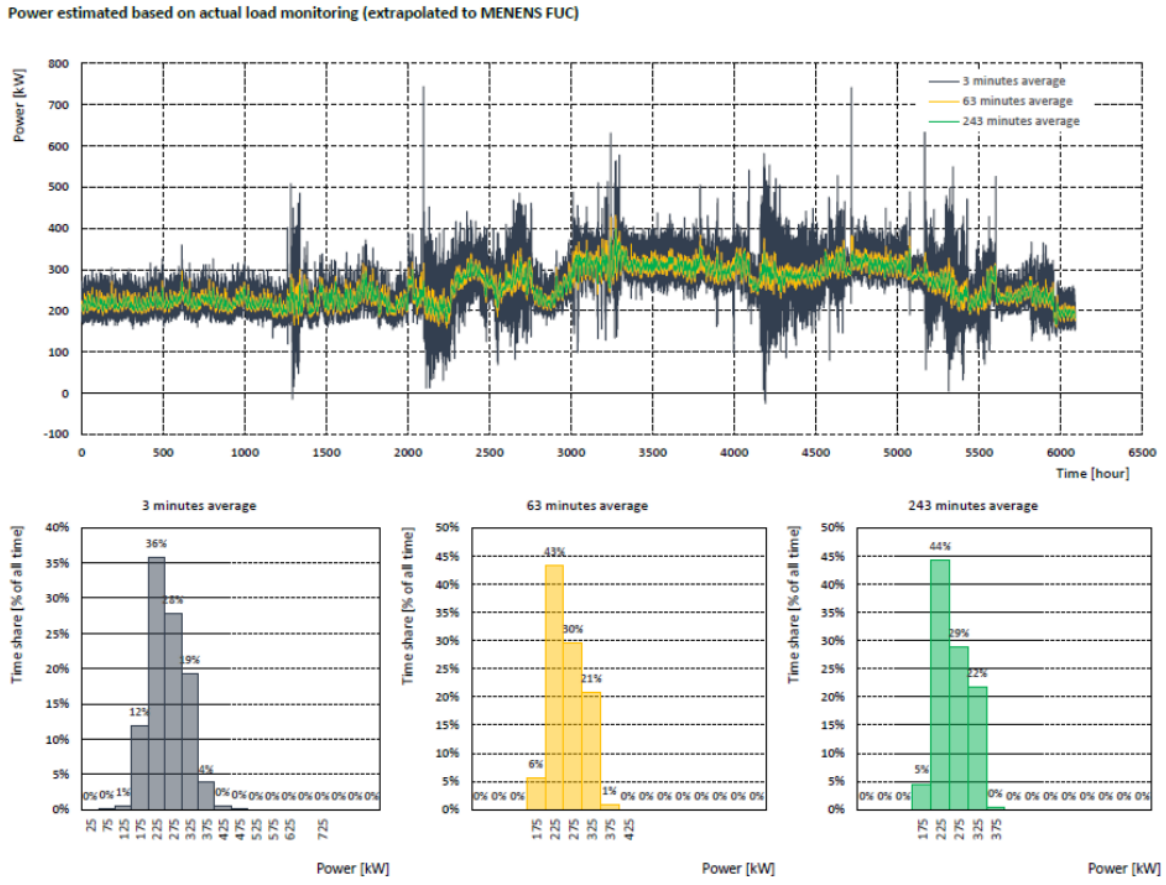

Figure A.1: Design ship's auxiliary power load profile [11].

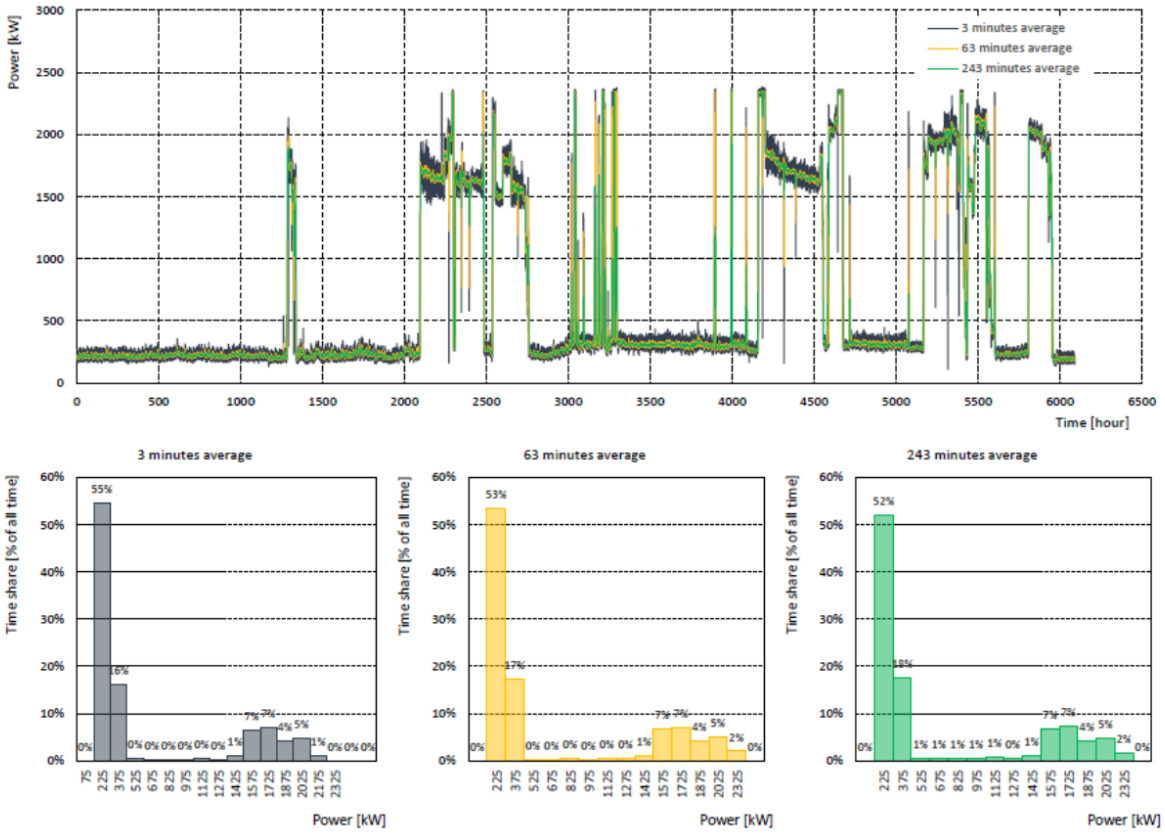

Figure A.2: Design ship's total power load profile [11].

Appendix B

Langmuir-Hinshelwood kinetic model

$$
\begin{aligned}
k_R &= k_R^{\infty} \exp\left(-\frac{E_R}{RT}\right), \\
k_D &= k_D^{\infty} \exp\left(-\frac{E_D}{RT}\right), \\
k_W^* &= k_W^{\infty *} \exp\left(-\frac{E_W^*}{RT}\right), \\
K^*_{CH_3O(1)} &= \exp\left(\frac{\Delta S^*_{CH_3O(1)}}{R} - \frac{\Delta H^*_{CH_3O(1)}}{RT}\right), \\
K^*_{HCOO(1)} &= \exp\left(\frac{\Delta S^*_{HCOO(1)}}{R} - \frac{\Delta H^*_{HCOO(1)}}{RT}\right), \\
K^*_{OH(1)} &= \exp\left(\frac{\Delta S^*_{OH(1)}}{R} - \frac{\Delta H^*_{OH(1)}}{RT}\right), \\
K^*_{CO_2(1)} &= \exp\left(\frac{\Delta S^*_{CO_2(1)}}{R} - \frac{\Delta H^*_{CO_2(1)}}{RT}\right), \\
K_{H(1a)} &= \exp\left(\frac{\Delta S_{H(1a)}}{R} - \frac{\Delta H_{H(1a)}}{RT}\right),
\end{aligned}
$$

$$
\begin{aligned}
K^*_{CH_3O(2)} &= \exp\left(\frac{\Delta S^*_{CH_3O(2)}}{R} - \frac{\Delta H^*_{CH_3O(2)}}{RT}\right), \\
K^*_{HCOO(2)} &= \exp\left(\frac{\Delta S^*_{HCOO(2)}}{R} - \frac{\Delta H^*_{HCOO(2)}}{RT}\right), \\
K^*_{OH(2)} &= \exp\left(\frac{\Delta S^*_{OH(2)}}{R} - \frac{\Delta H^*_{OH(2)}}{RT}\right), \\
K^*_{CO_2(2)} &= \exp\left(\frac{\Delta S^*_{CO_2(2)}}{R} - \frac{\Delta H^*_{CO_2(2)}}{RT}\right), \\
K_{H(2a)} &= \exp\left(\frac{\Delta S_{H(2a)}}{R} - \frac{\Delta H_{H(2a)}}{RT}\right).
\end{aligned}
$$

Methanol-steam reaction:

$$
r_R = \frac{k_R K^*_{CH_3O(1)} \left(p_{CH_3OH}/p_{H_2}^{1/2}\right) \left(1 - p_{H_2}^3 p_{CO_2}/k_R p_{CH_3OH} p_{H_2O}\right) C_{S_1}^T C_{S_{1a}}^T}{\left(1 + K^*_{CH_3O(1)} \left(p_{CH_3OH}/p_{H_2}^{1/2}\right) + K^*_{HCOO(1)} p_{CO_2} p_{H_2}^{1/2} + K^*_{OH(1)} \left(p_{H_2O}/p_{H_2}^{1/2}\right)\right) \left(1 + K_{H(1a)} p_{H_2}^{1/2}\right)}.
$$

Water-gas shift reaction:

$$r_W = \frac{k_W^* K_{OH(1)}^* \left(p_{CO} p_{H_2O} / p_{H_2}^{1/2}\right) \left(1 - p_{H_2} p_{CO_2} / k_W p_{CO} p_{H_2O}\right) C_{S_1}^{T2}}{\left(1 + K_{CH_3O(1)}^* \left(p_{CH_3OH} / p_{H_2}^{1/2}\right) + K_{HCOO(1)}^* p_{CO_2} p_{H_2}^{1/2} + K_{OH(1)}^* \left(p_{H_2O} / p_{H_2}^{1/2}\right)\right)^2}.$$

Decomposition reaction:

$$r_D = \frac{k_D K_{CH_3O(2)}^* \left(p_{CH_3OH} / p_{H_2}^{1/2}\right) \left(1 - p_{H_2}^2 p_{CO} / k_D p_{CH_3OH}\right) C_{S_2}^T C_{S_{2a}}^T}{\left(1 + K_{CH_3O(2)}^* \left(p_{CH_3OH} / p_{H_2}^{1/2}\right) + K_{OH(2)}^* \left(p_{H_2O} / p_{H_2}^{1/2}\right)\right) \left(1 + K_{H(2a)} p_{H_2}^{1/2}\right)}.$$

Table B.1: Parameters for rate constants in the comprehensive kinetic model.

Rate constants	**Kinetic parameters**	
	k^∞ ($\mathrm{m^2 s^{-1} mol^{-1}}$)	E (kJ $\mathrm{mol^{-1}}$)
k_R ($\mathrm{m^2 s^{-1} mol^{-1}}$)	7.4×10^{14}	102.8
k_D ($\mathrm{m^2 s^{-1} mol^{-1}}$)	3.8×10^{20}	170.0
k_W^* ($\mathrm{m^2 s^{-1} mol^{-1}}$)	5.9×10^{13}	87.6

Table B.2: Parameters for adsorption coefficients in the comprehensive kinetic model.

Adsorption coefficients	**Kinetic parameters**	
	ΔS^* (J $\mathrm{mol^{-1} K^{-1}}$)	ΔH^* (kJ $\mathrm{mol^{-1}}$)
$K_{CH_3O_{(1)}}^*$ ($\mathrm{bar^{-0.5}}$)	-41.8	-20.0
$K_{OH_{(1)}}^*$ ($\mathrm{bar^{-0.5}}$)	-44.5	-20.0
$K_{H(1a)}$ ($\mathrm{bar^{-0.5}}$)	-100.8	-50.0
$K_{HCOO_{(1)}}^*$ ($\mathrm{bar^{-0.5}}$)	179.2	100.0
$K_{CH_3O_{(2)}}^*$ ($\mathrm{bar^{-0.5}}$)	30.0	-20.0
$K_{OH_{(2)}}^*$ ($\mathrm{bar^{-0.5}}$)	30.0	-20.0
$K_{H(2a)}$ ($\mathrm{bar^{-0.5}}$)	-46.2	-50.0

Appendix C

Configuration A stream results at design point

Table C.1: Configuration A stream results at design point part 1.

Stream	**Units**	**S4**	**TANK**
Phase		Vapor	Liquid
Temperature	°C	233.27	20
Pressure	bar	0.8	1
Molar Vapor Fraction		1	0
Molar Liquid Fraction		0	1
Molar Solid Fraction		0	0
Mole Flows	kmol/hr	46.398	7.143
CH_3OH	kmol/hr	0.00132	2.857
H_2O	kmol/hr	4.331	4.286
H_2	kmol/hr	0.00025	0
CO_2	kmol/hr	4.193	0
CO	kmol/hr	4.29×10^{-6}	0
O_2	kmol/hr	6.269	0
N_2	kmol/hr	31.232	0
Ar	kmol/hr	0.372	0

Table C.2: Configuration A stream results at design point part 2.

Stream	**Units**	**AIR-BURN**	**AIR-FEED**	**AIR-PEM**	**ANOD-OUT**	**CAT-OUT**	**COLD-IN**	**COOL-IN**	**COOL-OUT**	**FEED**
Phase		Vapor Phase	Vapor Phase	Vapor Phase	Vapor Phase	Vapor Phase	Liquid Phase	Liquid Phase	Liquid Phase	Vapor Phase
Temperature	°C	20	53.03	20	79.85	79.85	20.20	20.00	78.00	280
Pressure	bar	1	1	1	1.496	0.212	20	1	0.8	20
Molar Vapor Fraction		1	1	1	1	1	0	0	0	1
Molar Liquid Fraction		0	0	0	0	0	1	1	1	0
Molar Solid Fraction		0	0	0	0	0	0	0	0	0
Mole Flows	kmol/hr	40	38.47	38.47	0.249	42.50	7.143	237.29	237.29	7.143
CH_3OH	kmol/hr	0	0	0	0	0	2.857	0	0	2.857
H_2O	kmol/hr	0	0	0	0	8.059	4.286	237.29	237.29	4.286
H_2	kmol/hr	0	0	0	0.249	0	0	0	0	0
CO_2	kmol/hr	0.016	0.015	0.015	0	0.015	0	0	0	0
CO	kmol/hr	0	0	0	0	0	0	0	0	0
O_2	kmol/hr	8.38	8.059	8.059	0	4.030	0	0	0	0
N_2	kmol/hr	31.232	30.037	30.037	0	30.037	0	0	0	0
Ar	kmol/hr	0.372	0.358	0.358	0	0.358	0	0	0	0

Table C.3: Configuration A stream results at design point part 3.

Stream	**Units**	**FLU-IN**	**FLU-OUT**	**FLUE-GAS**	**H_2-FEED**	**MET-BURN**	**PERMEATE**	**RETENTAT**	**S1**	**S2**	**S3**
Phase		Vapor	Vapor	Vapor	Vapor	Liquid	Solid	Solid	Vapor	Vapor	Liquid
Temperature	°C	399.99	233.27	641.41	80	20	232.57	232.57	232.57	232.57	20
Pressure	bar	1	0.800	1	1	1	0.800	18.677	0.8	18.709	0.6
Molar Vapor Fraction		1	1	1	1	0	0	0	1	1	0
Molar Liquid Fraction		0	0	0	0	1	0	0	0	0	1
Molar Solid Fraction		0	0	0	0	0	1	1	0	0	0
Mole Flows	kmol/hr	46.398	46.398	46.398	8.309	1.321	8.309	4.544	8.309	4.544	237.29
CH_3OH	kmol/hr	0.00132	0.00132	0.00132	0	1.321	0	0.00250	0	0.00250	0
H_2O	kmol/hr	4.331	4.331	4.331	0	0	0	1.435	0	1.435	237.29
H_2	kmol/hr	0.00025	0.00025	0.00025	8.309	0	8.309	0.251	8.309	0.251	0
CO_2	kmol/hr	4.193	4.193	4.193	0	0	0	2.850	0	2.850	0
CO	kmol/hr	4.29×10^{-6}	4.29×10^{-6}	4.29×10^{-6}	0	0	0	0.00429	0	0.00429	0
O_2	kmol/hr	6.269	6.269	6.269	0	0	0	0	0	0	0
N_2	kmol/hr	31.232	31.232	31.232	0	0	0	0	0	0	0
Ar	kmol/hr	0.372	0.372	0.372	0	0	0	0	0	0	0

Appendix D

Configuration B stream results at design point

Table D.1: Configuration B stream results at design point part 3.

Stream	**Units**	**RETENTAT**	**S4**	**TANK**
Phase		Vapor	Liquid	Liquid
Temperature	°C	267.91	20	20
Pressure	bar	9.997	0.6	1
Molar Vapor Fraction		1	0	0
Molar Liquid Fraction		0	1	1
Molar Solid Fraction		0	0	0
Mole Flows	kmol/hr	4.769	237.30	7.428
CH_3OH	kmol/hr	0.146	0	2.971
H_2O	kmol/hr	1.798	237.30	4.457
H_2	kmol/hr	0	0	0
CO_2	kmol/hr	2.658	0	0
CO	kmol/hr	0.167	0	0
O_2	kmol/hr	0	0	0
N_2	kmol/hr	0	0	0
Ar	kmol/hr	0	0	0

Table D.2: Configuration B stream results at design point part 1.

Stream	**Units**	**AIR-BURN**	**AIR-FEED**	**AIR-PEM**	**ANOD-OUT**	**CAT-OUT**	**COLD-IN**	**COOL-IN**	**COOL-OUT**	**FEED**
Phase		Vapor Phase	Vapor Phase	Vapor Phase	Vapor Phase	Vapor Phase	Liquid Phase	Liquid Phase	Liquid Phase	Vapor Phase
Temperature	°C	20	60.70	20	79.85	79.85	20.09	20.00	78.00	280
Pressure	bar	1	1	1	1.496	0.212	10	1	0.8	10
Molar Vapor Fraction		1	1	1	1	1	0	0	0	1
Molar Liquid Fraction		0	0	0	0	0	1	1	1	0
Molar Solid Fraction		0	0	0	0	0	0	0	0	0
Mole Flows	kmol/hr	34.90	38.47	38.47	0.249	42.50	7.428	237.30	237.30	7.428
CH_3OH	kmol/hr	0	0	0	0	0	2.971	0	0	2.971
H_2O	kmol/hr	0	0	0	0	8.059	4.457	237.30	237.30	4.457
H_2	kmol/hr	0	0	0	0.249	0	0	0	0	0
CO_2	kmol/hr	0.01396	0.01539	0.01539	0	0.01539	0	0	0	0
CO	kmol/hr	0	0	0	0	0	0	0	0	0
O_2	kmol/hr	7.312	8.059	8.059	0	4.030	0	0	0	0
N_2	kmol/hr	27.25	30.037	30.037	0	30.037	0	0	0	0
Ar	kmol/hr	0.325	0.358	0.358	0	0.358	0	0	0	0

Table D.3: Configuration B stream results at design point part 2.

Stream	**Units**	**FLU-OUT**	**FLUE-GAS**	**H2-FEED**	**H2-FEED1**	**H2-IN**	**HOT-OUT**	**MET-BURN**	**REAC-OUT**	**RETE1**
Phase		Vapor Phase	Vapor Phase	Vapor Phase	Vapor Phase	Vapor Phase	Vapor Phase	Liquid Phase	Vapor Phase	Vapor Phase
Temperature	°C	271.63	681.47	267.91	80	267.91	399.998	20	267.91	267.91
Pressure	bar	0.8	1	1	1	1	1	1	9.997	10
Molar Vapor Fraction		1	1	1	1	1	1	0	1	1
Molar Liquid Fraction		0	0	0	0	0	0	1	0	0
Molar Solid Fraction		0	0	0	0	0	0	0	0	0
Mole Flows	kmol/hr	41.33	41.33	8.309	8.309	8.309	41.33	1.116	13.08	4.769
CH_3OH	kmol/hr	0.00126	0.00126	0	0	0	0.00126	1.116	0.146	0.146
H_2O	kmol/hr	4.319	4.319	0	0	0	4.319	0	1.798	1.798
H_2	kmol/hr	0	0	8.309	8.309	8.309	0	0	8.309	0
CO_2	kmol/hr	4.099	4.099	0	0	0	4.099	0	2.658	2.658
CO	kmol/hr	0.000167	0.000167	0	0	0	0.000167	0	0.167	0.167
O_2	kmol/hr	5.337	5.337	0	0	0	5.337	0	0	0
N_2	kmol/hr	27.25	27.25	0	0	0	27.25	0	0	0
Ar	kmol/hr	0.325	0.325	0	0	0	0.325	0	0	0